Hydraulic fracturing under waterflooding conditions in unconsolidated sands

Exploring fracture creation capabilities using low viscosity injection fluids

by

T. A. Chorus

to obtain the degree of Master of Science
at the Delft University of Technology,
to be defended publicly on Friday August 31, 2018 at 2:30 PM.

Student number:	4082117	
Project duration:	November 27, 2017 – August 31, 2018	
Thesis committee:	Dr. A. Barnhoorn,	TU Delft, supervisor
	Dr. K. H. A. A. Wolf,	TU Delft, supervisor
	Dr. Ir. K. De Borst,	Shell
	Prof. Dr. P. L. J. Zitha,	TU Delft

TU Delft

Preface

I would like to take this opportunity to thank my supervisors Auke Barnhoorn and Karl-Heinz Wolf, for guiding me the past 9 months. Your endless enthusiasm to help, advice and brainstorm during and after the experiments have made this project feel special and very enjoyable for me. I highly appreciate the time and effort both of you have put in this thesis. Also a thank you to Pacelli Zitha for taking the time to read and assess this work.

From Shell, I would first of all like to thank Karin de Borst. The collaboration together during all stages of this thesis was very pleasant for me. I thank you for listening to and appreciating my input and giving a high level of guidance throughout the entire project. Also from Shell, I would like to thank Frank van der Heyden and Roelien Broos for their direct and indirect input at several stages of this research.

A big thank you goes out to the technical support staff of the Geoscience & Engineering laboratory. Marc Friebel a special thank you to you, working together has been fantastic. You went above and beyond to make this project a success, with countless input on a practical side of view. I have learned a great deal of you and hope we continue to meet even after I graduated. Also a thank you to Jens van den Berg, Karel Heller, Joost van Meel and Ellen Meijvogel - de Koning for your help with the intensifier, sensors and CT scanner. This project could not have been done without you.

Last but not least, a thank you to my parents for their support during all 8 years of my studies. It has been a long journey and I am grateful for your unconditioned encouragement. Even though my extracurricular activities may not always have been in the best interest for you, you supported me regardless, both socially and financially. This is something I will remain grateful for the rest of my life. In addition, a thank you goes out to my girlfriend Emma, to keep me sane throughout the harder phases of this project. Thank you for your support regardless of my mood after a long day of work.

Tijmen Chorus
Delft, August 2018

Abstract

Rapid injectivity decline is frequently observed during injection in unconsolidated sand reservoirs. Field data suggests that hydraulic fracture processes are directly or indirectly related to this injectivity decline. Conventional fracture theories do not apply to unconsolidated sand since this material has little to no cohesion and tensile strength. The main fracture mechanism hypotheses are shear failure of the zone ahead of the fracture tip and fluidization. For both mechanisms, a fluid pressure high enough to initiate and propagate the fracture is required. The fluid pressure is dependent on the injection rate, fluid viscosity and permeability of the formation. Unconsolidated sands have a high permeability, thus under normal waterflood conditions a high injection pressure is not expected. Three main impairment mechanisms leading to the injectivity decline have been identified based on field evidence and previous work:

- Plugging
- Wellbore fill
- Resorting of grains and finer particles

Plugging results from the infiltration of fines originating from the injection fluid, crossflow or drilling mud. The external and/or internal filter cake can locally reduce the permeability of the formation. During surface shut-ins, backflow and/or crossflow can occur leading to the infiltration of solid particles and fluids into the wellbore. This reduces the leak-off area of the well. Lastly, resorting of grains and finer particles can result in a denser packing of the reservoir. The dynamically mixing of particles can lead to lower permeability regions.

Research goal The main goal of this research is to develop a better qualitative and quantitative description of the fracturing process and the impairment mechanisms causing the observed injectivity decline. This thesis comprises of the first phase of this research, focusing on the capabilities of the equipment to create and detect fractures under waterflooding conditions. What makes this research unique is the use of low viscosity fluids, to mimic field conditions. Other work often involves the use of efficient fracturing fluids that have a high viscosity and/or good filter cake building capabilities to minimalize the leak-off. Next to that, injection of fluids is performed live in a CT scanner. This allows the visualization of fractures or low-density regions through density distributions in three dimensions over time.

Equipment Injection takes place in a high-strength aluminium vessel with a sample volume of 3.84 dm^3. See images 2.1 and 2.2 of an overview of the setup and pressure vessel. Axial and radial pressure can be controlled independently up to 20 MPa. A pore fluid system records the outflow mass and provides a fluid pressure on the sample. The sample consists of a very fine, very well sorted sand with a permeability around 5 Darcy. The main injection fluids are water and Fluorinert FC-770. This is a high density, low viscosity fluid that is used to visualize the preferential flow path of the injection fluid in the CT scanner.

Results Fractures have been successfully created using a high viscosity fluid during the first experiment. The goal of that experiment was to test the setup and the equipment. The fractures were created at an injection pressure of 38 MPa and were up to 1 cm long and 2 mm wide. Experiments 2 and 3 were performed in the CT scanner with the use of Fluorinert as the injection fluid. The infiltration zone of this fluid was clearly visible but no fractures were created. Sand infiltration in the injection tube leaded to a number of problems during the experiments. Experiments 4 and 5 added fines to the injection water. Quartz powder was used in experiment 4 and bone meal in experiment 5. The fines leaded to a gradual increase in injection pressure, but did not lead to a higher density in the CT scans. No fractures were observed but low-density regions in front of the perforations were created during both experiments as a result of backflow. Experiment 6 introduced the use of internal pressure sensors in the sample and used a sample created with two sands and Kaolinite, a non-swelling clay. During two high flowrate injection cycles, the clays migrated away from the near wellbore region, leaving behind lower density regions.

Conclusion & future work Creating fractures with low viscosity fluids in a laboratory environment has proven to be difficult. No fractures have been created throughout the low viscosity experiments. Several impairment mechanisms that were identified in the field have also been observed in the experiments. This thesis forms a solid basis for the next research phase to investigate these impairment mechanisms more closely. By lowering the confining stresses, increasing the flow rates and decreasing the sample permeability, there is a good probability that fractures can be created with this equipment in future work.

Contents

List of Tables

List of Figures

1 Introduction

Water injection is a common method in the oil industry to stimulate production from oil-bearing formations. The injected water reduces the reservoir pressure decline as oil is being produced. Next to that, the water displaces the oil from the injection wells towards the production wells, a process called sweeping. The combination of the pressure support and the sweeping increases the recovery factor, meaning less residual oil in the reservoir after its production lifetime. If sweeping efficiency is unsatisfactory, additional measures can be taken such as adding chemicals to the injection stream as part of EOR projects.

1.1. Injectivity decline

Rapid injectivity decline is frequently observed when injecting in unconsolidated sand reservoirs. Injectivity is often quantified with the injectivity index, which in its simplest form is just the ratio of the injection rate to the difference between the injection pressure and the far-field reservoir pressure, see equation 1.1.

$$II = \frac{Q}{P_{bhi} - P_e} \tag{1.1}$$

Where: II = Injectivity index [$m^3/d/bar$]
Q = Injection rate [m^3/d]
P_{bhi} = Bottomhole injection pressure [bar]
P_e = External boundary pressure [bar]

A decrease in injectivity will lead to higher injection pressures which can force injection rates to be decreased. As a consequence water flood progress as well as ongoing EOR projects may be delayed. In some cases, the injectivity decreases to a point that the injection well has to be abandoned. Currently there is no complete explanation available as to what causes this rapid injectivity decline, nor is there a full understanding of the risks involved. Injection pressure and rate field data suggest that hydraulic fracture processes take place during the injectivity decline. Pressure builds up to a critical limit followed by a short pressure decrease and injection rate increase. Such a pressure peak profile is typical for hydraulic fractures being formed. However, conventional hydraulic fracturing theories of competent rock do not apply to unconsolidated sand. These formations have little to no cohesion and thus no significant tensile strength. So other physics and mechanisms take place to initiate the fracture and drive the fracture propagation. Although hydraulic fractures locally enhance the permeability of the formation, it is essential to understand why the formation of these fractures eventually decrease the injectivity of the well in unconsolidated sand reservoirs. By understanding the mechanisms that take place we may have better control over fracture containment and (partially) prevent the injectivity decline.

1.2. Fracture mechanisms

Several studies have been conducted to research the hydraulic fracturing mechanisms of cohesionless materials. Under normal water injection conditions, the injected fluid flows into the formation through its connected pores. The infiltrated formation volume is called the leak-off zone, or simply infiltration zone. For

hydraulic fractures to form in unconsolidated sand, the leak-off of the injection fluid needs to be minimalized so a fluid pressure can build up to initiate the fracture. This is the case when a high flow rate is used, high viscosity fluids are injected and/or the formation has a low permeability. High viscosity fluids are typically not injected in the field. However, reinjecting produced water is a common practice. This produced water often contains solids such as sand particles or other fines originating from the reservoir. It is possible that these solids create an internal and/or external filter cake, which reduces the permeability of the formation. Injection rate is of course a factor that can be directly controlled. Chang [6] suggests that hydraulic fracturing of cohesionless materials has three stages:

1. Cavity expansion, before the pressure peak
2. Fracture front initiation from that cavity, near the pressure peak
3. Propagation of the developed fracture, after the pressure peak

The fracture front initiates from a boundary instability in stage 2, but the exact nature of this instability is unclear.

1.2.1. Shear failure

Shear banding, the process where shearing strain deformes the material and typically forms X-shaped shear bands, has been suggested to be responsible for the instability and trigger the fracture initiation. This theory is backed up by Khodaverdian [10] who also hypothesizes that fracture propagation is primarily a result of shear failure of the zone ahead of the fracture tip. For continuous fracture propagation, the leak-off must remain minimal. This requires a low permeability zone, either in the form of an external or internal filter cake, that stays in front of the fracture tip. To form this filter cake, the area ahead of the fracture tip has to be infiltrated by the injection fluid before the fracture can propagate any further. This is an essential difference to hydraulic fracturing of competent rock, where the injection fluid lags behind the fracture tip.

1.2.2. Fluidzation

Shear failure of the zone ahead of the fracture tip is not the only hypothesis for fracture propagation. Chudnovsky [7] describes fluidization as a mechanism to create fluid localizations around crack-like displacement discontinuities, rather than fractures. Under normal conditions, the unconsolidated sand formation consists of loose unattached grains, which are compressed by confining stresses to create a stable porous medium. Chudnovsky describes that as the fluid pressure exceeds the confining stress acting on a region, the effective stresses in this region become zero. The sand then loses its stability and undergoes rearrangements due to the fluid flow. This rearrangement results in a significant increase in the local permeability and porosity, forming the fluid localizations within the formation. The grains can mobilize in one or mutliple planes, depending on the number of directions that the fluid pressure exceed the confining stresses.

1.3. Impairment mechanisms

Concerning the injectivity decline, three main impairment mechanisms have been identified based on field evidence and previous work:

- Plugging
- Wellbore fill
- Resorting of grains and finer particles

All of these mechanisms may be directly or indirectly enhanced by hydraulic fracturing and are responsible for a decrease in injectivity. Plugging is caused by the creation of external and/or internal filter cake and locally reduces the permeability of the formation. The filter cake reduces the leak-off of the injection fluid, which might be necessary for the fractures to initiate and propagate. Wellbore fill results from surface shut-ins of the injection well and/or when crossflow occurs. The reverse flow brings in loose grains from the formation into the injection well where they accumulate and reduce the leak-off area of the well. The reduction of the leak-off area results in higher local injection velocities and pressures. Lastly, the resorting of grains and finer particles can result in a denser packing of the sand. The dynamically mixing of these particles leads to lower permeability zones that reduce the leak-off.

1.4. Research goals and objectives

The ultimate goal of this research is to develop a better qualitative and quantitative description of the fracturing process and the impairment mechanisms causing the observed injectivity decline. This includes developing a better understanding under which conditions fractures form and what geometry these fractures have. To achieve this a series of injection tests will be done in a pressure vessel that contains a sand sample. The vessel in combination with connected pumps can be used to exert an axial, radial and fluid pressure on the sample. What makes this research unique is the live injection of fluids into the sample in a CT scanner. Fractures typically close completely or partially when no more pressure is being exerted on the sample. Due to this, it is often not possible to get a good view of the formed fractures when the sample is being excavated. Other work often use fluids or gels that solidify after curing [6, 9] or cooling [7] to keep the fracture open while the sample is excavated. The use of a CT scanner prevents the need for these fluids and allows us to visualize fractures or low porosity regions through density distributions in three dimensions over time.

Previous work with great results is done with this equipment by De Pater [5] and Dong [8]. Their studies however focus on efficient fracturing fluids, where efficient in this context means high viscosity and/or good filter cake building capabilities to minimalize the leak-off. This research will focus on field conditions during waterflooding by using low viscosity injection fluids. In essence, this makes successfully fracturing the unconsolidated sand more complicated but does mimic field conditions more closely.

At least two phases will build up this Shell supported research topic at the TU Delft. This thesis comprises of phase 1, where the focus will be on exploring the capabilities of the equipment to create and detect fractures under waterflooding conditions. The main variables in these experiments are the injection system, fluids, flowrates, pressures and sample composition. Next to that, the effect of adding fines to the injection fluid on the permeability and leak-off will be studied. The techniques developed and problems encountered and resolved in this thesis will form a solid basis for the next phases of this research. Phase 2 will focus on studying the injectivity impairment mechanisms.

1.5. Thesis structure

Information about the equipment used together with a detailed description of the testing procedures is given in chapter 2. Any specifications of the pressure vessel, injection system, pumps, CT scanner, etc. can be found there. Adjustments made to the system to accommodate the injection of low viscosity fluids are also mentioned there. Lastly, a description of the sample sand and the injection fluids with additives are given. Chapter 3 describes the processing of the CT images. The types of noise encountered and how to deal with them is discussed. An overview of all the steps involved in visualizing the infiltration region is given and explained. Results of each injection test are given in chapter 4. They are presented here with the help of figures from the data acquisition system and images of the CT scanner. During this chapter the results are also discussed and abnormalities are visualized and explained. The final findings and conclusions will be presented at the end, following with a recommendation for the next phases of this research to finish off. The appendices include a variety of material, such as additional CT images, more detailed research procedures and technical drawings.

2

Research design

2.1. Equipment

The equipment used can be divided into four modules, namely the CT cell, the injection system, the pore fluid system and the data acquisition system. A schematic overview of the setup can be seen in figure 2.1. For complete experiments, the CT cell is placed in a CT scanner to create cross-sectional images of the sample through time.

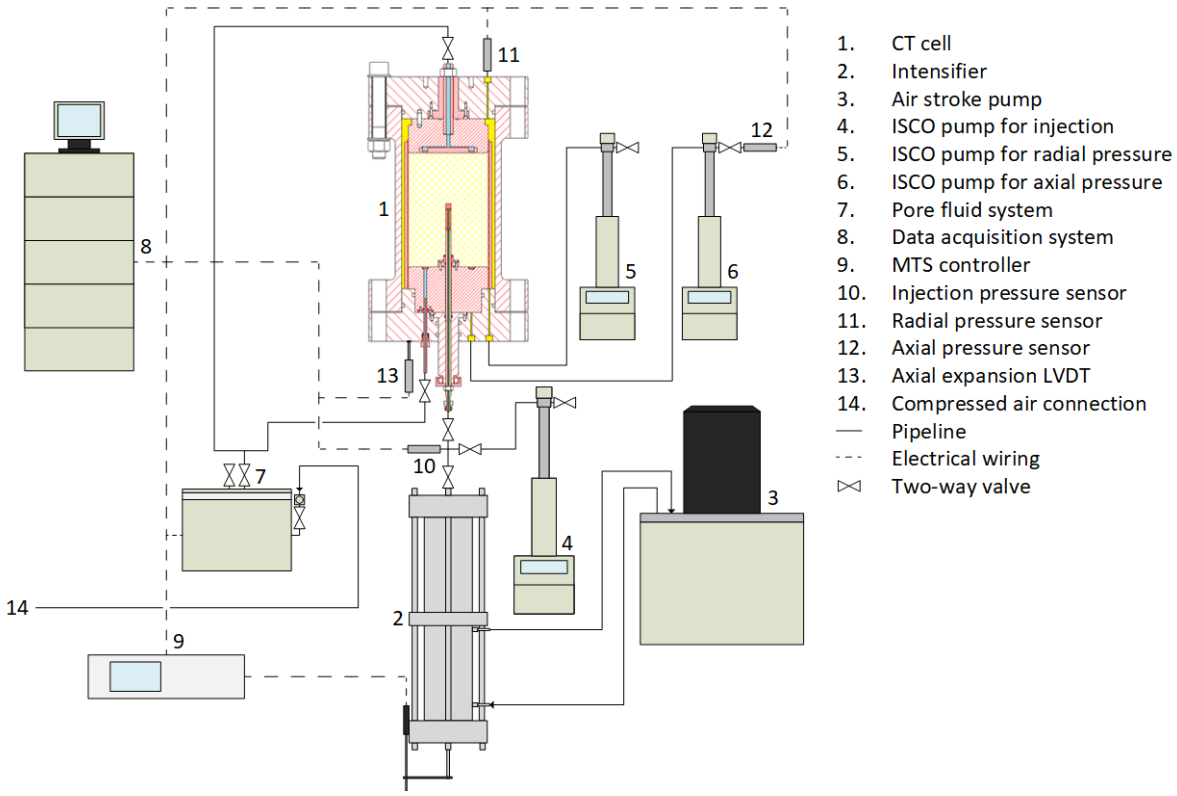

Figure 2.1: Equipment setup

2.1.1. CT cell

The CT cell is a cylindrical pressure vessel with high-strength aluminium walls. The cell is small enough to be placed inside a CT scanner and the aluminium makes it X-ray transparent. It can contain a sample with a diameter of 152 mm and a length of 213 mm. The total sample volume is 3.84 dm^3. Figure 2.2 shows a technical drawing of the CT cell. A radial and axial pressure of up to 20 MPa can be exerted on the sample

using hydraulic oil. The pressures can be controlled independently. Through the centre of the sample, an injection tube runs from one side of the vessel to the middle, which allows fluids to be injected.

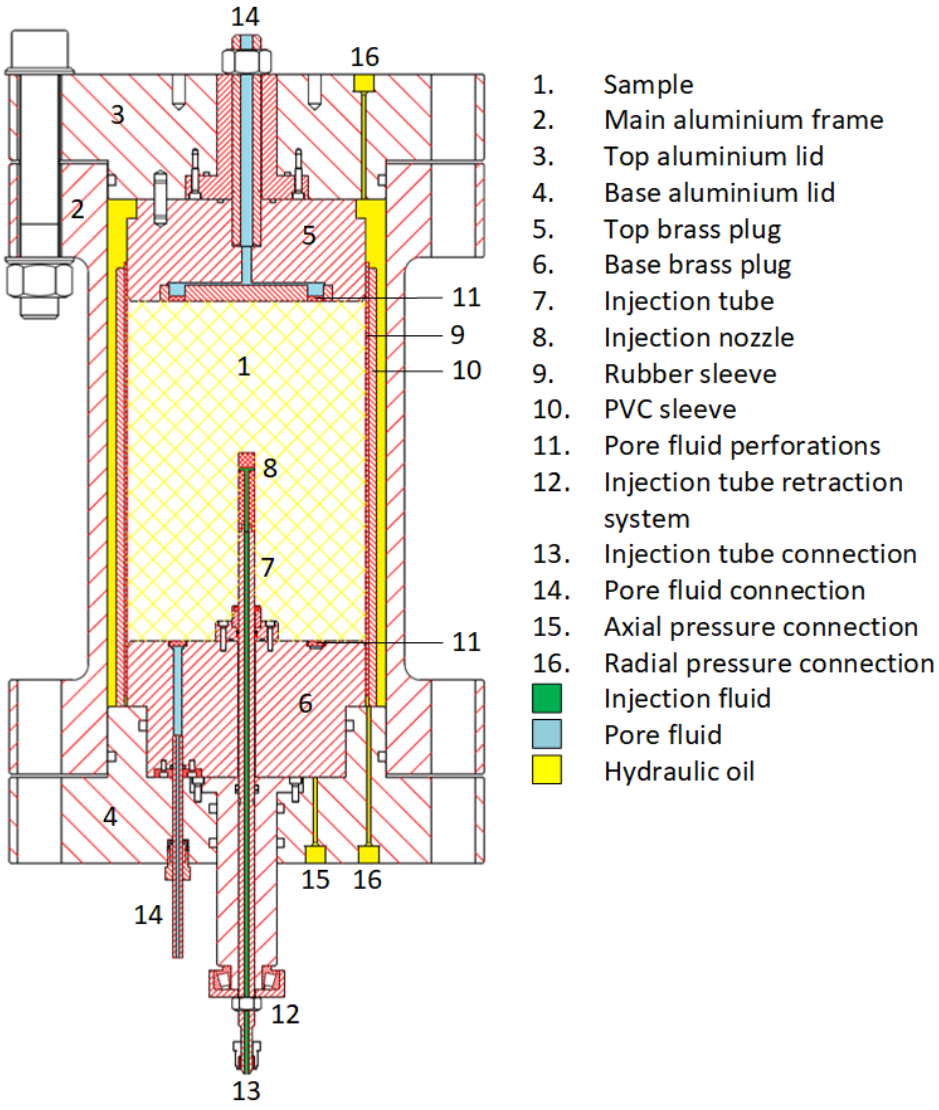

Figure 2.2: Technical drawing CT cell

Sample The sample is hold in place by brass plugs on the axial axis. The base plug exerts axial pressure on the sample using hydraulic oil, while the top plug is static. Both plugs have perforations containing sinter filters through which pore fluid can flow. On the radial axis, the sample is hold in place by a rubber sleeve, which sits inside a separate PVC sleeve. The rubber sleeve separates the sample and its pore fluid from the hydraulic oil used to exert a radial pressure. The PVC sleeve is used to support the sample, mainly during sample preparation. It contains perforations on four sides along its entire length, which allows the hydraulic oil to make contact with the rubber sleeve.

Vessel To seal the vessel, thick aluminium lids are secured on each side with bolts and nuts. Both sides contain connections for the radial hydraulic oil and the pore fluid system. The base side contains the entrance for the injection tube and the connection for the axial hydraulic oil. After sample preparation, the CT cell is turned horizontally and mounted on a frame to hold it in place in the CT scanner. It is attached to the CT scanner medical bed to move it in axial direction through the CT scanner during experiments. This allows for a 3D construction of the sample made from several CT scan images.

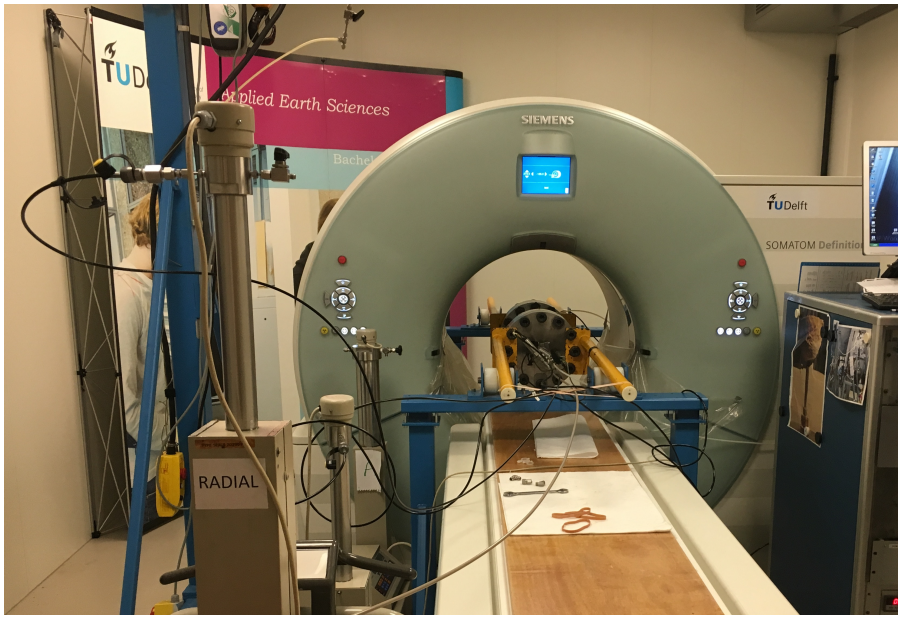

Figure 2.3: CT cell in CT scanner

2.1.2. Injection system

The injection system consists of the injection tube, the injection nozzle, the injection pumps and a series of high-pressure valves and tubing to connect them. The injection tube is made out of stainless steel and has an outer diameter of 10 mm and an inner diameter of 2 mm. The inner diameter is widened to 3 mm for experiment 6. The injection tube runs from outside of the CT cell, through the aluminium lid and brass plug, to the centre of the sample. An injection nozzle can be screwed on top of the injection tube or an open borehole interval can be made.

Open borehole To create an open borehole interval, a cap is placed on top of the injection tube during sample preparation. The cap prevents sand of clogging the injection tube during preparation. After the CT cell is closed, the injection tube is pressurized to the pore fluid pressure and the injection tube can be retracted. The cap comes loose from the injection tube, creating an open borehole interval in between. It is possible to place a butterfly nut on the injection tube, which leaves a groove as the injection tube is retracted that can help control the initial fracture direction. It also creates an instability which helps initiate a fracture. The mechanism to create the open borehole with the butterfly nut can be seen in figure 2.4a. Creating an open borehole is only possible using a high viscosity injection fluid. The high viscosity injection fluid is needed to prevent the open borehole from collapsing while it does not leak off into the sample before injection starts.

Injection nozzle For lower viscosity injection fluids, an injection nozzle should be used. The injection nozzle used in this set of experiments is made out of aluminium, since it creates less noise than steel in the CT images. The nozzle has two perforations perpendicular to each other. The perforations originally had a diameter of 1 mm, but is widened to 1.5 mm and 2.5 mm throughout the experiments. During the experiments, it became clear that the sand clogged up the injection nozzle, which resulted in high-pressure drops in the injection nozzle. An external sand screen was placed in front of the perforations to prevent the inflow of sand particles. A sand screen with a diameter of 180 µm was not sufficient to stop the injection tube from clogging. Switching to a sand screen of 75 µm gave better results. Figure 2.4b shows the aluminium injection nozzle with the external sand screen.

Pumps For high flow rate injection, an air stroke pump in combination with a hydraulic intensifier is used. The air stroke pump pressurizes the intensifier with a closed off hydraulic oil system up to 31 MPa. The intensifier works at a 1:2 ratio, leading to an output of up to 62 MPa. It can inject 600 cm^3 before it needs to be refilled. The injection rate is controlled by a MTS controller, which measures the intensifier's piston position using an LVDT. For injection rates up to 408 cm^3/min, ISCO pumps are used. They are more precise and

(a) Butterfly nut on injection tube

(b) Injection nozzle with external sandscreen

Figure 2.4: Injection nozzles

easier to handle than the intensifier and air stoke pump. Several ISCO pumps are available; the ones used are described in table 2.1. The 500D Syringe Pump is also available in a dual-pump continuous flow setup. This setup lets one pump inject while the other is refilling, allowing greater volumes to be continuously injected if required.

Pump name	Capacity	Max. flow rate	Max. pressure
-	cm^3	cm^3/min	MPa
1000D Syringe Pump	1015	408	13.79
500D Syringe Pump	507	204	25.86
65D Syringe Pump	68	25	139

Table 2.1: Injection pumps specifications

Connections The injection tube and the injection pumps are connected with a series of stainless steel tubes with an outer diameter of 6.35 mm and an inner diameter of 4.57 mm. Since the CT scanner room cannot be entered during scanning due to radiation, pumps and/or their control panel need to be stationed outside of the CT scanner room. The control panel of the intensifier was wired to the control room of the CT scanner. In case an ISCO pump was used for injection, the entire pump was stationed in the control room of the CT scanner. It was connected to the injection system with a PEEK tube of 6 m. These PEEK tubes are flexible and can handle a pressure up to 22.7 MPa. They have an outer diameter of 6.35 mm and an inner diameter of 3 mm. The main valve of the injection system connects the injection tube with the steel tubes leading to the injection pumps. This valve is closed in between injection cycles so no back flow can occur. Valves used operate for pressures up to 41.37 MPa. A pressure sensor positioned in between the injection pump and the main valve measures the fluid pressure in the injection system.

Additives When solid particles are added to the injection fluid, a mixing vessel is added to the injection system. The goal of this mixing vessel is to keep the particles in suspension and prevent them from forming a sediment. The mixing vessel has a volume of 2.22 dm^3 and can be used to inject with a maximum pressure of 15 MPa. The pump injects at the bottom of the mixing vessel while the mixture flows out of the top of the vessel towards the injection tube. Due to the inflow of injection fluid, the concentration of solid particles in the mixture decreases over time. The mixing vessel is stationed on top of a magnetic stirrer, which stirs the magnetic bar at the bottom of the vessel. The use of solid particles also requires a different mechanism to prevent sand inflow from the sample into the injection tube. This is because a sand screen would clog up over time with the solid injection particles. As a solution, a small rubber cylinder was positioned inside

of the injection nozzle, in front of the perforations. This piece of rubber prevents sand from entering the injection tube, mainly during sample preparation. When injection starts, the pressure build up pushes the rubber further up into the injection nozzle, opening up the perforations.

2.1.3. Pore fluid system

The pore fluid can flow in and out of the CT cell through the brass plugs on both sides of the sample. Both plugs have a set of eight perforations with a diameter of 10 mm. Sinter filters prevent any solid particles from entering the pore fluid system. The pore fluid is then directed through the aluminium lid towards the backpressure system. The backpressure system is a pressure vessel with a weighing scale. It is pressurized with compressed air to give a backpressure of 0.2 MPa. The scale measures the weight of pore fluid in the vessel through time. The pore fluid connection at each side of the CT cell is controlled with a valve. One of the brass plugs and its filters can be seen in figure 2.5.

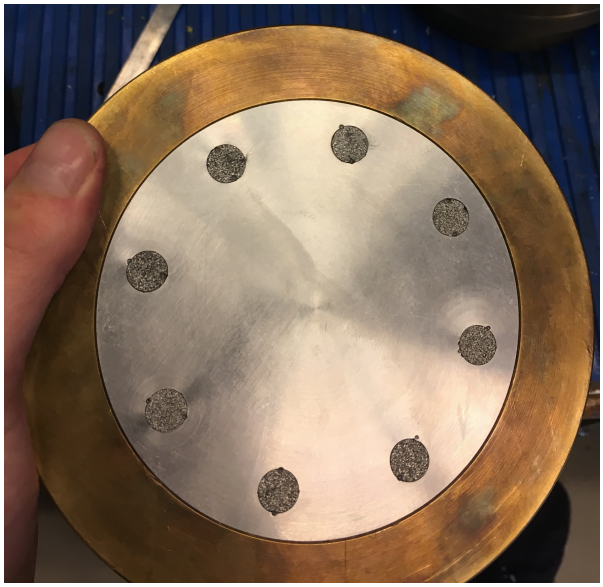

Figure 2.5: Brass plug with sinter filters

2.1.4. Data acquisition system

All pressure sensors and other measurement tools are connected to the data acquisition system. This system reads and stores the data with time intervals of 1 second. There are three pressure sensors present in the setup. One to measure the axial pressure, one for the radial pressure and the last one for the injection pressure. The pressure sensors can operate up to 70 MPa. The weighing scale of the pore fluid system is also connected to the data acquisition system. It operates for masses up to 6200 g. To measure the axial deformation, an LVDT measures the position of the brass plug on the injection tube side of the CT cell. It can measure deformations up to 25.4 mm. In case the intensifier is used, the LVDT used to control the intensifier's piston is also connected to the data acquisition system.

2.1.5. CT scanner

A third generation Siemens Somaton Plus 4 Volume Zoom (dual beam) CT scanner is used to create the internal images of the CT cell and the sample. The CT cell is lifted into the scanner with the use of a crane. Since the medical bed is too fragile to support the weight of the CT cell, a supporting frame is build around the scanner. The CT cell is free to move in and out of the scanner with the help of rollers on the supporting frame. This means the cell is fixed in the radial X and Y direction and moves along its sample length in the Z direction. The cell is connected to the movable medical bed so it can be moved automatically during the CT scans.

Resolution Scans can be made either with or without moving the CT cell. Making a static scan, meaning not moving the CT cell, an interval of 3 cm can be scanned with z-slices of 1.2 mm. When moving the CT

cell, scans are made while the cell moves in the Z direction after which it has to return to its original position. The disadvantage of this method is that moving back to the original position takes time, reducing the time resolution of the scans. The advantage however is that the Z resolution of the scans is doubled to 0.6 mm slices instead of 1.2 mm slices when doing a static scan. The X and Y resolution stays the same at 0.5 mm per pixel width and length. Scanning an interval of 5 cm in the Z direction while moving takes roughly 3.5 seconds after which it returns to its original position in another 3 seconds. This means a scan can be made every 6.5 seconds. The scan interval can be increased but results in longer scan times. When making a static scan, the maximum interval of 3 cm is scanned in approximately 4.5 seconds. Since the scanner can overheat when making too many scans in a short amount of time, the choice was made to use the moving scan method. The scanner can then cool down when returning to its original position, allowing more consecutive scans to be made with double the Z-direction resolution.

2.2. Materials

2.2.1. Sample

The samples are made up of Sibelco GA39 quartz sand, which can be classified as a very fine, very well sorted sand. The physical properties, chemical composition and grain size distribution can be found in tables 2.2, 2.3 and 2.4 respectively. The grain size distribution curve is plotted in figure 2.6. The samples have an initial porosity of 42 to 45%, which is compacted to 41 to 42% using our sample preparation method.

Physical property	Unit	Value
Bulk density	g/cm^3	2.65
Hardness	Mohs	7
pH	-	7
Dry apparent density	g/cm^3	1.5

Table 2.2: Sample sand - Physical properties

Chemical composition	%
SiO_2	99.15
Al_2O_3	0.464
K_2O	0.265
TiO_2	0.069
Fe_2O_3	0.036
CaO	0.011

Table 2.3: Sample sand - Chemical composition

Grain size property	Unit	Sibelco analysis	TU Delft analysis
D90	µm	122	123
D60	µm	112	116
D50	µm	109	113
D10	µm	92	90
Coefficient of uniformity	-	1.2	1.3

Table 2.4: Sample sand - Grain size analysis

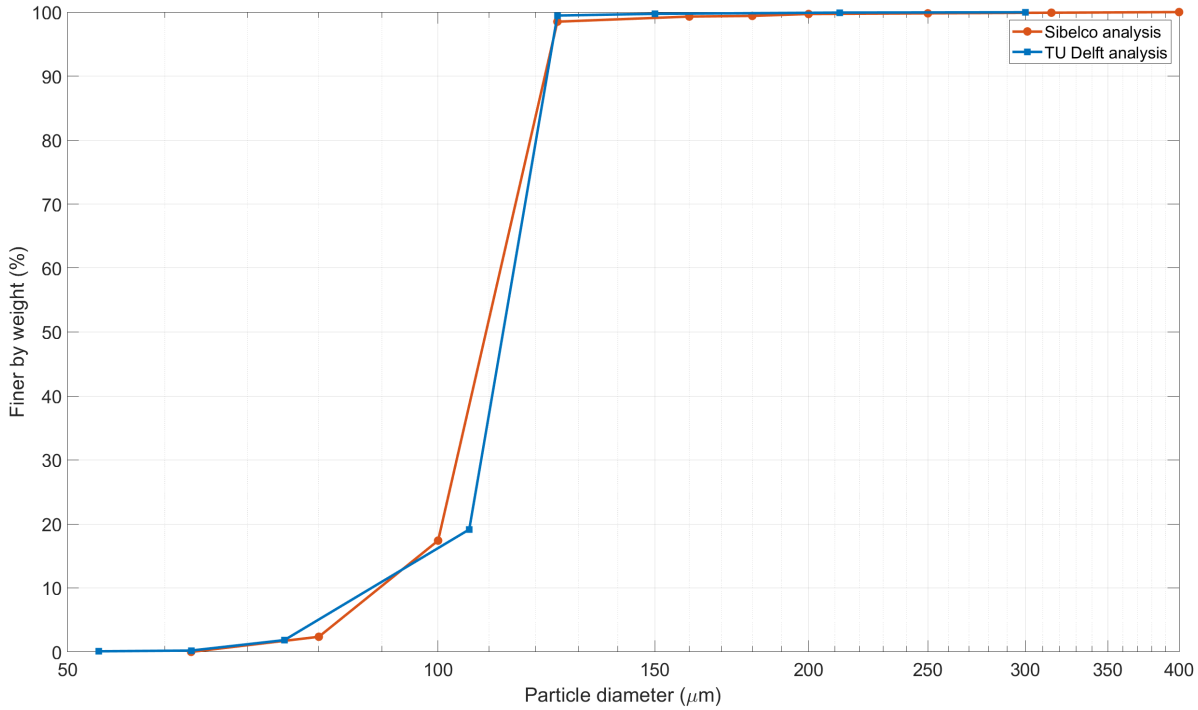

Figure 2.6: Sample grain size distribution

Permeability To estimate the pearmeability of the sample based on grain size, a variety of emperical relationships are available. Van Baaren's model [1] can be used, which uses Kozeny-Carman's equation with a series of substitutions:

$$k = 10 d_{dom}^2 \Phi^{3.64+m} C^{-3.64} \tag{2.1}$$

Where: k = Permeability [mD]
d_{dom} = Dominant grain size [µm]
Φ = Porosity [fraction]
m = Cementation factor [-]
C = Sorting index [-]

We are dealing with an unconsolidated sand that is extremely well to very well sorted. Leading to a cementation factor 1.4 and a sorting index of 0.70. Another approach is using the porosity - permeability correlation for unconsolidated artificial sandpacks by Beard and Weyl [2]. These authors used photographs of thin-sections of a wide range of samples from river sand to make estimations of grain diameters, sorting, porosity and permeability. And lastly Berg's model [3] can be used for additional estimations:

$$k = 80.8 \Phi^{5.1} d^2 e^{-1.385p} \tag{2.2}$$

Where: k = Permeability [D]
Φ = Porosity [fraction]
d = Median grain diameter [µm]
p = Percentile deviation P_{90} - P_{10} [phi]

An overview of the results of these equations for a range of porosities are given in table 2.5.A permeability measurement on this sand is performed using a constant head test. This sample had a porosity of 40.7 % and a permeability of 6.11 Darcy. This is a good match with the estimates of the empirical relationships. Note however, this sample was not subjected to external pressure. The porosity of the experiment samples are also measured before the sample is pressurized. However the results of table 2.5 give a good indication of the order of magnitude of the permeability. It is estimated that the pressurized sample permeability is around the 5 Darcy range.

Porosity	39 %	40 %	41 %	42 %	43 %
Van Baaren	3.93	4.46	5.05	5.71	6.43
Beard and Weyl	4.3	5.2	7.8	8.1	8.3
Berg	8.23	9.37	10.62	12.01	13.54
Average	5.49	6.34	7.83	8.61	9.42

Table 2.5: Sample sand - Permeability estimates [Darcy]

Experiment 6 For experiment 6 a different sample than the previous experiments is used. Two sands are mixed with Kaolinite, which is a non-swelling clay. The largest sand has a P50 of 264.7 micron. The second sand is the same sand as used in experiment 1 to 5 with a P50 of 109 micron. The sands and Kaolinite is mixed by weight, using 65 % of the very fine sand, 25 % of the fine to medium sand and 10 % clay. The physical properties of the fine to medium sand and the Kaolinite are added in table 2.6 and the chemical composition can be found in table 2.7. The grain size distribution of the mixture can be found in table 2.8 and figure 2.7. The properties of the very fine sand are already described in the first paragraph of this section. To prevent clays from infiltrating the injection tube, a 0.5 micron external sand filter was used.

Physical property	Unit	Fine to medium sand	Kaolinite
Bulk density	g/cm^3	2.65	2.60
Hardness	Mohs	7	1.5 - 2
pH	-	7	6
Dry apparent density	g/cm^3	1.5	0.4 - 0.7

Table 2.6: Sample sand experiment 6 - Physical properties

Chemical composition	Fine to medium sand [%]	Kaolinite [%]
SiO_2	99.5	56.91
Al_2O_3	0.20	39.68
K_2O	0.05	0.60
TiO_2	0.03	0.54
Fe_2O_3	0.03	0.93
CaO	0.01	0.16
Na_2O	0	0.60
MgO	0	0.16

Table 2.7: Sample sand experiment 6 - Chemical composition

Grain size property	Unit	Value
D90	µm	286.5
D60	µm	116.5
D50	µm	113.2
D10	µm	3.9
Coefficient of uniformity	-	29.9

Table 2.8: Sample sand experiment 6 - Grain size analysis

2.2.2. Injection fluids & additives

Three injection fluids are used in the experiments with two different solid additives. To test the equipment and compare its results to previous studies, a high viscous gel is used. Once experiments with this fluid are successful, a switch is made to low viscosity fluids to focus on the scope of this research. The first low viscosity fluid used is simply water, which is typically used in the field. The second low viscosity fluid has a high density to visualise its infiltration zone in the CT scanner. Solid additives have also been added to the injection fluids to attempt to plug the formation by creating an internal or external filter cake. An overview of the density and viscosity of the fluids can be found in table 2.9.

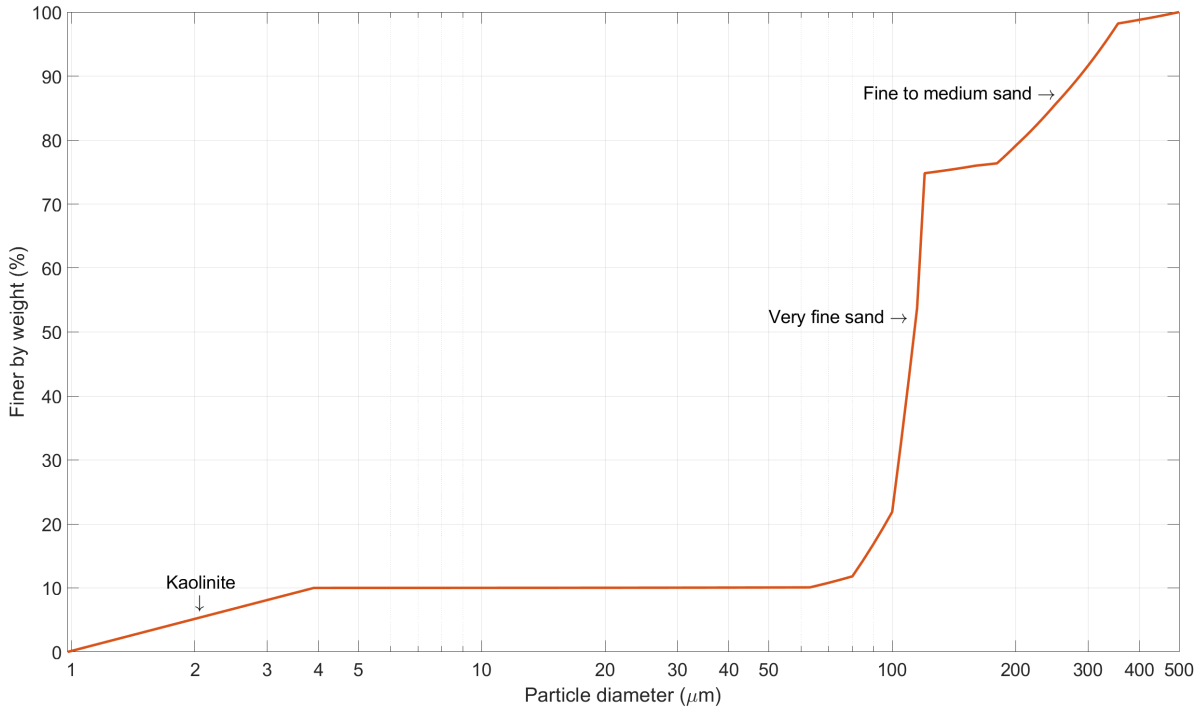

Figure 2.7: Sample experiment 6 grain size distribution

Viscasil 500M Viscasil is a high viscosity dimethyl silicone fluid that is clear and colourless. The fluid is dyed purple to better visualize the infiltration zone and potential fractures when excavating the sample. The high viscosity of over 500.000 mPa s decreases the leak-off potential of the fluid, which increases the probability of fracturing the sample. De Pater [Source] has made multiple fractures using this fluid and equipment setup. The high viscosity also helps keep the fractures open when the pressure is relieved on the sample. The main goal of this injection fluid is to test the equipment, which has not been used for several years. Once fractures have been made and the experimental procedures have been tested, low viscosity fluids will be used instead.

Fluorinert FC-770 Fluorinert is a fluorocarbon-based fluid that is typically used to cool electronics because of its electrically insulating capabilities. We however use it as an injection fluid because it has a high density (1.8 g/cm^3) in combination with a low viscosity (1.6 mPa s). The low viscosity, similar to that of water is the reason this fluid is suitable for this set of experiments. The high density allows it to be identifiable in the CT scanner and gives a clear contrast with the pore water. This lets us visualize any high permeability flow paths that have been created, such as channels or fractures. Next to that, we can see plugged areas within the sample or the clogging of one of the perforations with the use of this fluid. The fluorinert has a neglectable solubility in water of about 1.3 ppmw.

Physical property	Unit	Viscasil 500M	Fluorinert FC-770	Water
Density (20 °C)	g/cm^3	0.97	1.81	0.998
Dynamic viscosity (20 °C)	mPa s	5.05×10^5	1.58	1.002

Table 2.9: Injection fluid - Density and viscosity

Compressibility The isothermal compressibility of the tap water and Fluorinert FC-770 has been determined in the laboratory. Their results are plotted in figure 2.8 and will be used in experiment 4 and 5.

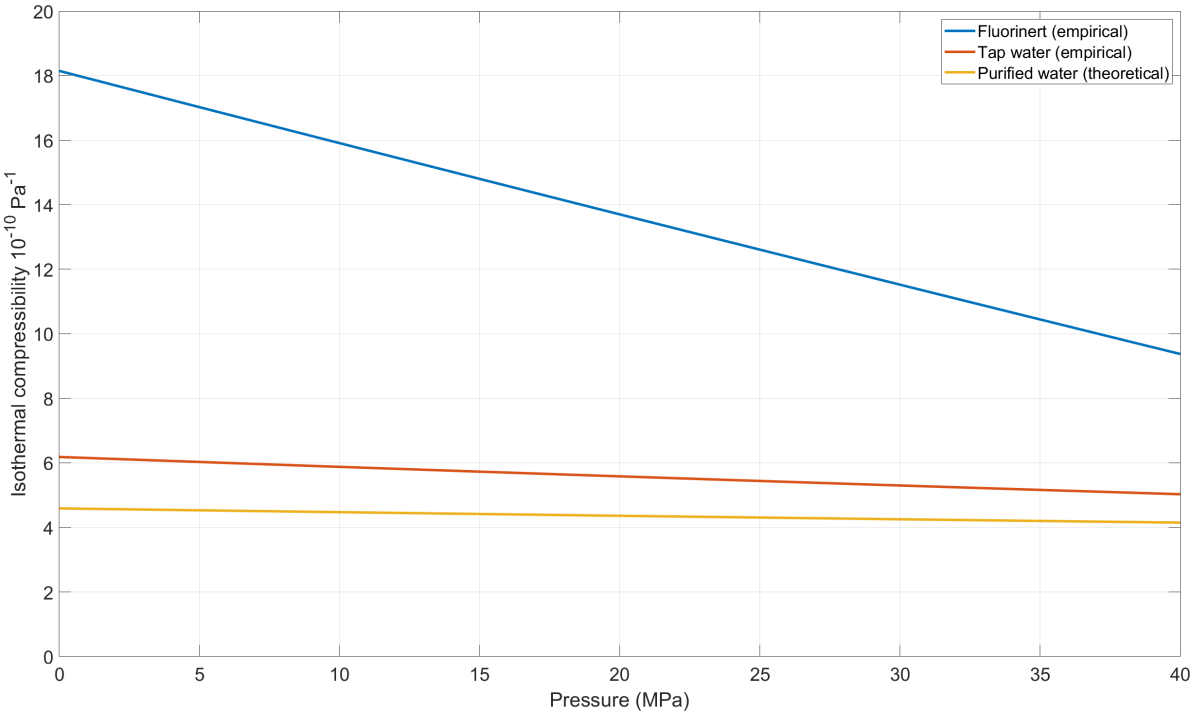

Figure 2.8: Compressibility injection fluids

Solid additives To decrease the leak-off of the injection fluids, solid additives are added in experiment 4 and 5 to try to create an internal or external filter cake in the sample. Both quartz flour and cow bone meal are used. SEM (Scanning Electron Microscope) images of the bone meal can be seen in figure 2.9 and 2.10. They show that the bone meal contain a large amount of fines in combination with some 50 to 100 micron grains. To filter these, the bone meal is sieved with a 32 micron mesh before it is added to the mixing vessel.

2.3. Testing procedures

The testing procedures have divided in three main stages: the sample preparation, the loading phase and the injection. During the sample preparation, the CT cell is prepared and sealed so it can be transported to the CT scanner. During the loading phase, the axial and radial pressure are build up, while the pore fluid system provides a backpressure. The experiment itself takes place in the injection phase, where we inject fluids at a constant rate or in cycles. For systematic procedures from a practical side of view, we refer to appendix .

2.3.1. Sample preparation

During sample preparation, the CT cell is positioned in a vertical position on top of a base pedestal, seen in figure 2.11. Before the sample can be made and compacted, the CT cell needs to be prepared. This includes placing the base brass plug into the base aluminium lid, inserting the injection tube and screwing on the injection nozzle. Once these are in place, the rubber sleeve can be attached to the base brass plug with the use of iron wire. This connection needs to be sealing to prevent pore fluid from leaking out of the sample and hydraulic fluid from entering the sample. The PVC sleeve is placed around the rubber sleeve and the main frame can be attached to the base aluminium lid. To prevent any air from being present in the system, the injection tube is filled with the injection fluid and the pore fluid system is filled with water before the sample is made.

Raining technique The sample is prepared using a wet raining technique. The CT cell is filled with 2.1 kg of water and is checked for any leaks. A tube is attached to the pore fluid system and set to the height of the

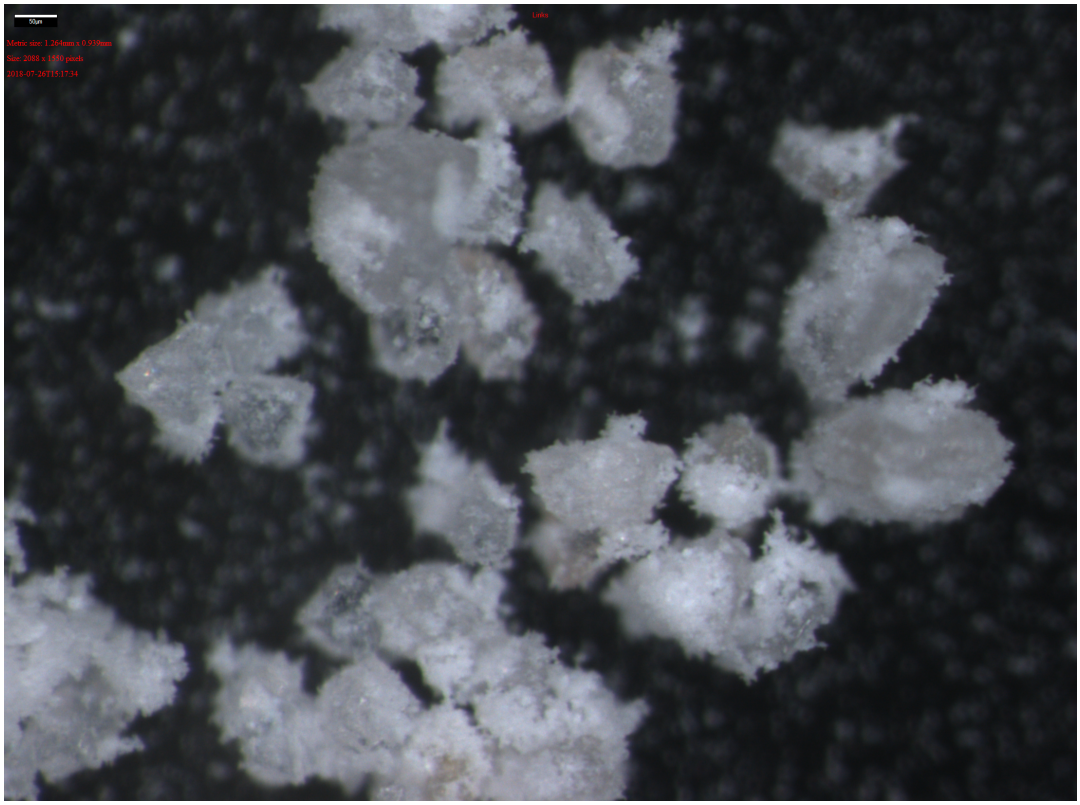

Figure 2.9: Bone meal SEM image 1 (scale = 50 micron)

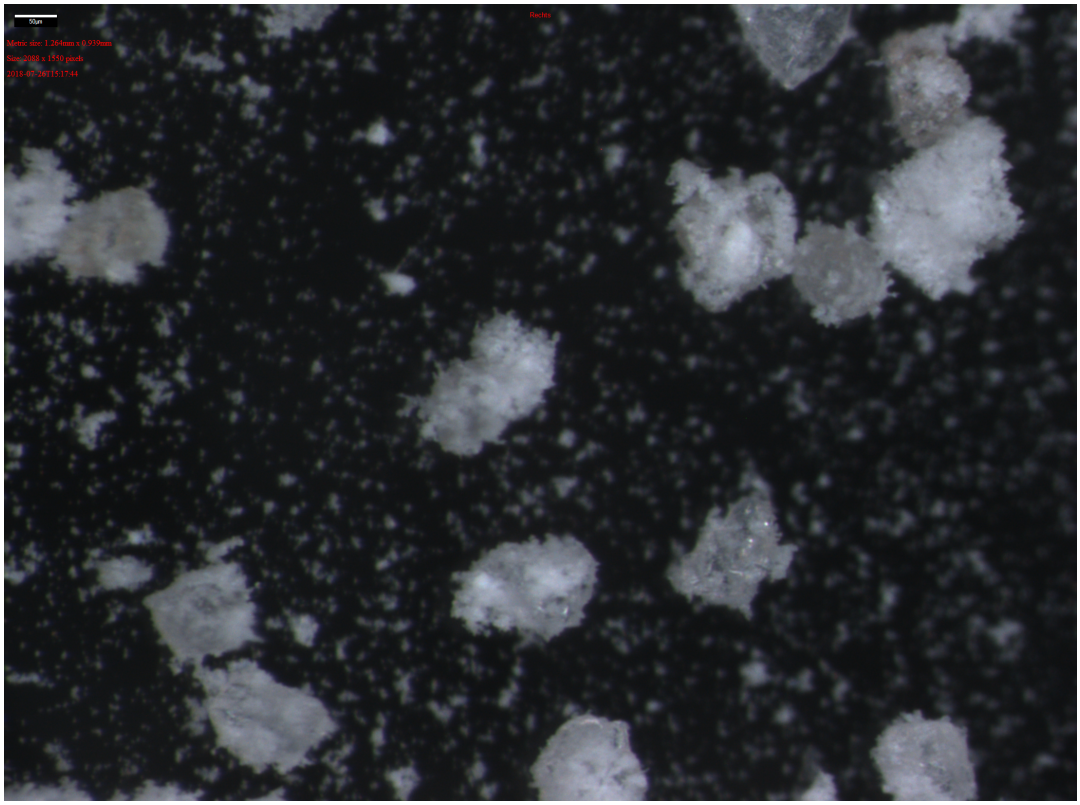

Figure 2.10: Bone meal SEM image 2 (scale = 50 micron)

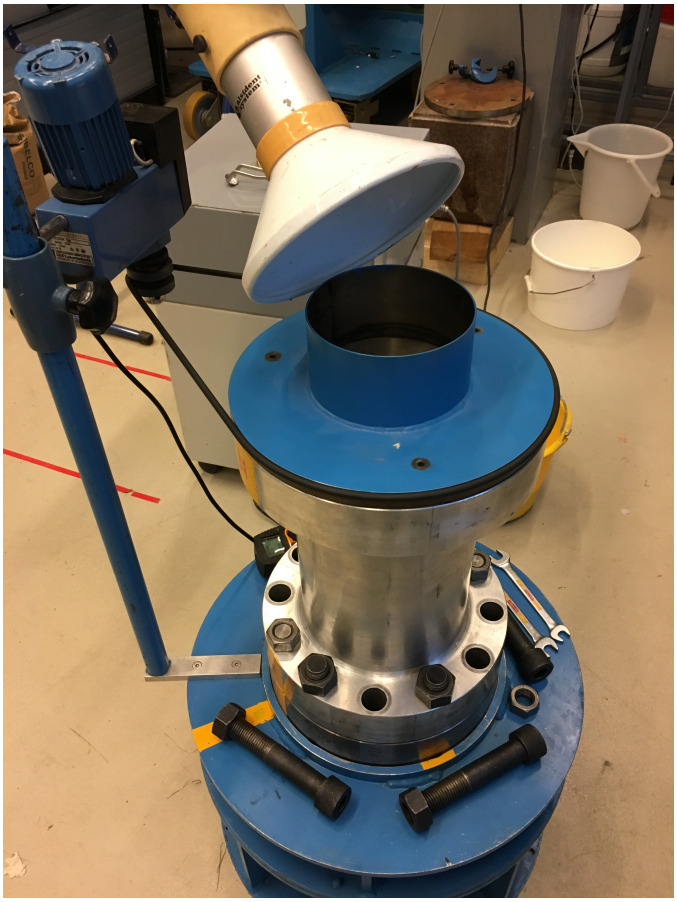

Figure 2.11: CT cell on base pedestral with silo

rubber sleeve, to prevent any water from overflowing when the sample is rained in. A silo with a sieve is then placed on top of the CT cell. The silo has the same diameter as the rubber sleeve in which it is placed, see figure 2.11. To ensure that the sand is distributed evenly along the entire area, the silo is rotated with a motor and a driving belt. The silo is then filled at a constant rate with a total of 6 kg of sand, which falls through the sieve into the rubber sleeve. This method creates a sample with an initial porosity of 42 to 45%. After the CT cell has been filled, the silo is removed. See appendix A for additional information.

Compaction To compact the sample, the CT cell is first attached to the base pedestal. Then both the CT cell and the base pedestal are lifted about 10 cm from the ground and dropped. Dropping is done in a controlled manner using the crane to lower the CT cell to hit the ground. On impact, the sample is compacted while the water is drained through the tube connected to the pore fluid system. This process is repeated 20 times. To ensure the sample has the correct height, sand and water is added or removed depending on the compaction. A 10 kg weight with the same size as the sample is placed on top after which the CT cell is dropped another 10 times. Once again, sand and water is added or removed from the top and the compaction process is repeated another 10 times with an extra 5 kg weight on top. This method creates a sample with a porosity of 41 to 42%.

Completion To complete the sample preparation, the tube connected to the pore fluid system is disconnected and the valve closed. To seal in the sample the top brass plug is placed on top of the sample. The area in between the rubber sleeve and the aluminium frame is filled with hydraulic oil, which will provide radial pressure at a later stage when connected to a pump. The CT cell can then be sealed with the top aluminium lid, which is attached to the main frame with bolts and nuts. To transport the CT cell to the CT scanner, it is removed from its base pedestal and placed on a cart in horizontal position. Once arrived in the CT scanner room, the support beams are connected to the CT cell. The CT cell is lifted in the CT scanner and connected to the medical bed. The cell can be now be connected to the pore fluid system, the injection system, the data acquisition system and the axial and radial pressure pumps.

Samples with clays A different sample preparation method is required for samples that contain clays or multiple sand grain sizes. This is because the raining technique will cause segregation of the grain sizes, resulting in a layered sample. The sands and clays are first mixed with the help of a sand splitter. This is a device with several grooves that mix and split the grains into two batches. By repeating this procedure 4 to 5 times, the grains become decently mixed. The silo that was used in the previous sample preparation method contains a sieve, making it unusable for this method. A large funnel is used instead, which is held 2 cm above the sample surface with a crane. The funnel is filled at a constant rate with the sample mixture, while gradually raising it to maintain the 2 cm gap in the vessel without any water. The funnel is spiralled around the injection tube to evenly distribute the sample mixture across the entire area. The same compaction method is then performed, with the exception that no water is present in the vessel. After the sample has compacted several times and refilled with sand mixture, the vessel is closed.

The sample now needs to be saturated with water. To do so, the sample is first vacuumized, so most of the air is out of the pores. After this, CO_2 is slowly injected from the bottom side of the vessel. This is followed by a very slow water injection rate to ensure the clays migrate as little as possible in the process. The CO_2 will dissolve in the water over time. This process takes several hours due to the slow injection rates.

2.3.2. Loading phase

During the loading phase, the axial and radial pressure is build up in the sample while a pore fluid back-pressure is applied. This is done in three stages to ensure a gradual and consistent pressure build up on the sample.

Initial loading In the first stage, the axial pressure is build up to 1.5 MPa while the radial pressure is build up to 1 MPa. This is done in steps of 0.1 to 0.2 MPa with the use of separate ISCO pumps for the radial and the axial pressure. At each step, the sample gets several seconds to stabilize with a total of about 3 minutes for the first loading stage. During this stage, the LVDT connected to the CT cell, picks up the axial compression of the sample.

Backpressure During the second stage, the pore fluid valves on both sides of the CT cell are gradually opened. This puts a backpressure of 0.2 MPa on the sample, which is maintained until the end of the experiment. When the pore fluid valves are opened, pore fluid flows into the sample. This takes about 3 minutes to stabilize. The radial and axial pressure also need to stabilize once again before the last loading stage can begin.

Final loading In the last loading stage, the radial and axial pressure are build up to their final level. For the set of experiments described in this thesis, an axial pressure of 3.5 MPa and a radial pressure of 2 MPa was used. However as previously mentioned, the CT cell can contain pressures up to 20 MPa. This process is done in steps of 0.1 to 0.3 MPa to once again ensure a gradual pressure build up. At any moment, the axial pressure is kept a minimum of 1.5 times above the radial pressure. Since the pore fluid valves are now open, pore fluid will flow out of the sample as the pressure on the sample is increased. Once the axial and radial pressure, the axial deformation and pore fluid flow have stabilized, the injection phase can begin.

2.3.3. Injection

Once all systems are ready, injection starts with opening the main injection valve. This valve sits directly in front of the injection tube on the outside of the CT cell. The CT scanner room is then exited and the injection pumps are controlled from the CT scanner control room. The pumps used depend on the injection fluid(s), flow rate and expected injection pressures. This can be either the intensifier in combination with the air stroke pump, an ISCO pump or both. Once the injection pump has started injecting, CT scans are made either with constant time steps or at manual times. Once injection has stopped the main injection valve is closed as soon as possible to prevent any flow back of the injection fluid.

3

Image processing

To detect and visualize fractures, low-density regions and/or Fluorinert infiltration zones, an image-processing algorithm needs to be set up. To maintain consistency, the algorithm needs to be applicable to all experiments without major adjustments. The algorithm that has been designed and developed over the course of the experiments will be discussed in this chapter. For this thesis, MATLAB 2018a is used for the computing environment. Some functions used are not compatible with older versions, but the image processing methods used are reproducible in other versions and computing environments as well. The image results can be found in chapter 4.

The main purpose of the image processing is to visualize the Fluorinert flow path. Any fractures or low-density regions, which typically means high porosity and permeability regions, will most likely give a flow path preference to the injection fluids. By visualizing the infiltration zone of the Fluorinert and reconstructing it in 3D, better conclusions can be formed as to how the sample reacted to the injection cycles. Next to the Fluorinert visualization, looking at image differences over time can give information about what happened throughout the experiment. This method can also be applied during injection cycles that do not use Fluorinert.

CT image noise & artefacts CT images contain a variety of noise and artefacts that need to be filtered and processed to facilitate a good image analysis. The main types of noise we encounter are Poisson noise, beam hardening & scatter and helical artefacts. Poisson noise is caused by low photon counts and is a statistical error. It results in random grayscale deviations that preferentially occur in the direction of the highest attenuation [4]. Its effect causes noise across the entire image and is best seen in the air (black region), due to the contrast, in figure 3.1.

When using polychromatic X-ray sources, or in other words, X-ray sources that produce a spectrum of energies, beam hardening can occur. High-density materials will attenuate the lower energy photons, leaving only the higher energy photons to contribute to the beam energy, thus 'hardening' the beam energy. This effect produces dark regions called streaking artefacts in several directions, depending on the position of the detector. In our scenario, the injection nozzle is made out of aluminium, which gives no problems. However, experiments 4 and 5 have a steel screw on top of the nozzle, which does give problems. Next to that, in some experiments a part of the steel injection tube, on which the nozzle is screwed, is also included in the scanned interval. Figure 3.2 shows streaking artefacts in a windmill shape that origins from the steel injection tube.

Helical artefacts can occur in CT scans where to be scanned object moves through the scanner. These artefacts are created due to interpolation processes of the CT scanner. Most visible in our experiments is the so-called zebra artefact, which are alternating high and low density regions. This effect can be seen in figure 3.3. This plots shows the grayscale value of a straight line of pixels in the Z axis. The pixels are all in a Fluorinert saturated sample region. The line should be roughly straight, with the excepts of some sample heterogeneity. However, it visualizes the alternating high and low density regions in 2 to 4 cm intervals that are a results of zebra artefacts. The helical artefacts spiral in the Z direction through the sample depending on the location of the CT scanner detector at the time of the scan. This effect is also clearly visable when image differences over time are compared.

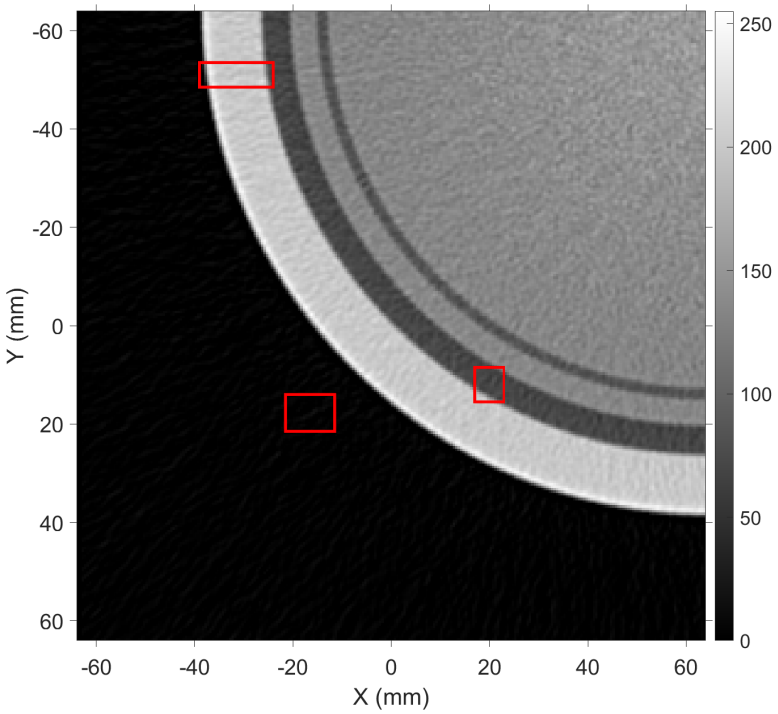

Figure 3.1: Poisson noise

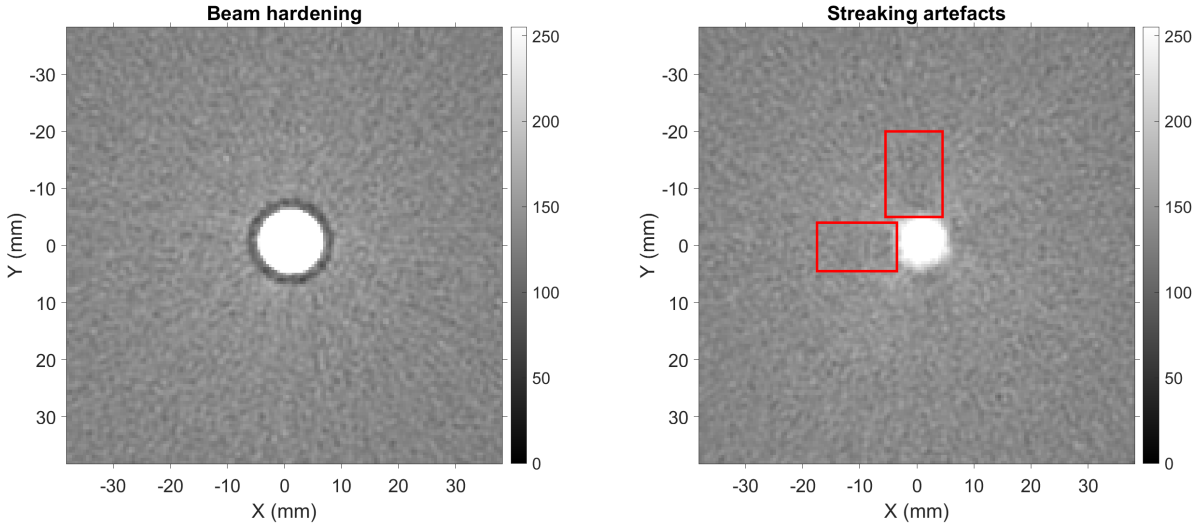

Figure 3.2: Beam hardening

The last type of noise is a natural grayscale gradient over the radial axis of the sample. The centre of the sample has the highest natural grayscale value, which gradually decreases towards the outer borders of the sample, this is best seen in figure 3.8.

To filter, process and visualise the results of the CT images, four main image-processing phases can be distinguished: pre-processing, image difference, static materials filtering and Fluorinert filtering. An overview of these processes are given in a flowchart in figure 3.4 and will be explained in the upcoming sections.

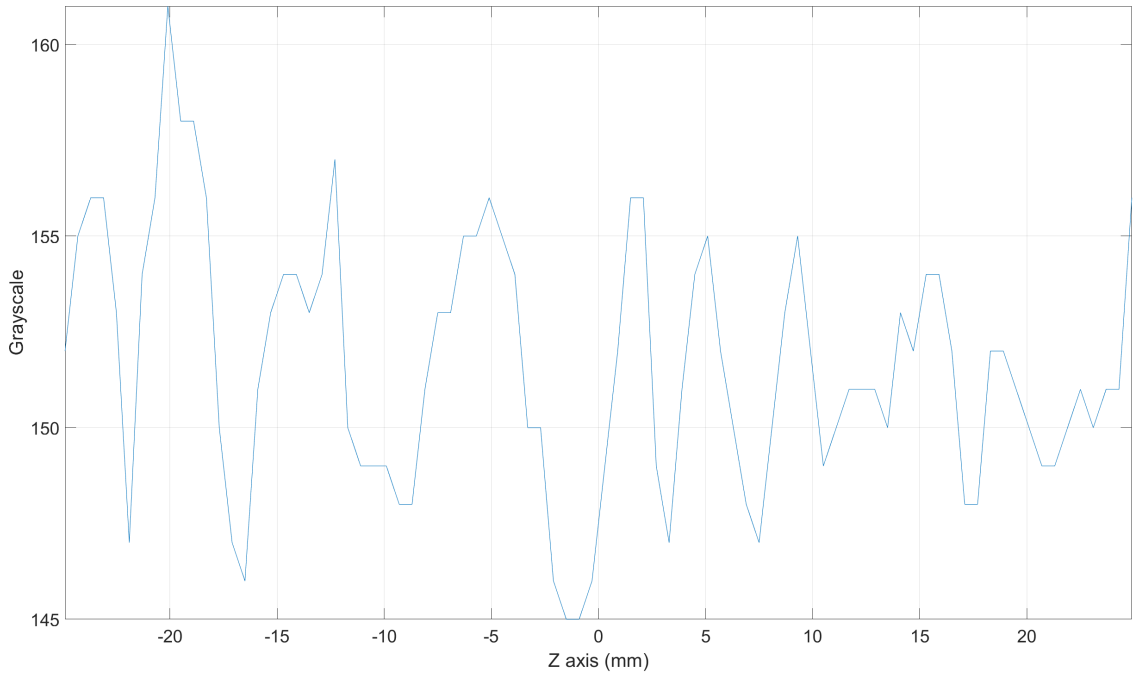

Figure 3.3: Zebra artefact

3.1. Pre-processing

The CT images typically come in an .IMA file format, which most computing environments cannot directly read. Multiple image converter programs are available to convert it to a file extension that is more suitable for importing it into a computing environment. IrfanView is an example of an image converter that can handle the .IMA file extension and is the software used for this set of experiments. All scans are converted into a .PNG file extension, which is a lossless compression file format so no data is lost. As previously mentioned in section 2.1.5, the resolution of the images are 0.5 mm in the X and Y direction and 0.6 mm in the Z direction. We typically scan a Z interval of 5 to 5.5 cm of the CT cell, which results into 84 or 92 slices in the Z direction. All images have 512 by 512 pixels in the X, Y plane. This results in 262.144 pixels per CT scan slice, 22 to 24 million pixels per 3D CT scan and up to 625 million pixels per experiment that need to be processed. The images are imported into the computing environment and saved in a 4D matrix in an X, Y, Z, t format. On two occasions it has occurred that the first CT scan in time had to be shifted 2 pixels in the X plane to align them with the others. This was caused by a different CT scan setting for the first scan and has only occurred for the first set of experiments.

3D Median filter A 3D median filter will be used multiple times throughout the algorithm. It is a commonly used digital filtering technique to remove noise from an image. The median filter takes, as the name suggests, the median grayscale value of the nearby pixels. In our case, every pixel takes the median grayscale value of the 3 by 3 by 3 cube pixels surrounding it. This filter technique does a particular good job at preserving detail near the edges of materials, such as near the injection tube and at the boundary of the Fluorinert infiltration zone. This is because the median filter actually picks an existing grayscale value, rather than a possibly unrealistic value from a mean filter. Next to that, the method is more robust and less affected by outliers than most other filter techniques. Figure 3.5 illustrates the effect of the 3D median filter.

3.2. Image difference

With the term image difference, we mean the difference in grayscale value between an image at time 1 and an image at time 2. This is simply done by subtracting one image from another. It is crucial to do this after pre-processing, otherwise a large portion of the image differences are a result of Poisson noise. An RGB grayscale image has values from 0 (black) to 255 (white). The image difference results are scaled from -255 to 255 towards 0 to 255 and visualized with colour map. Blue represents a decrease in grayscale and thus density, whilst red represents an increase in density. Image 3.6 visualizes the results of an image difference operation.

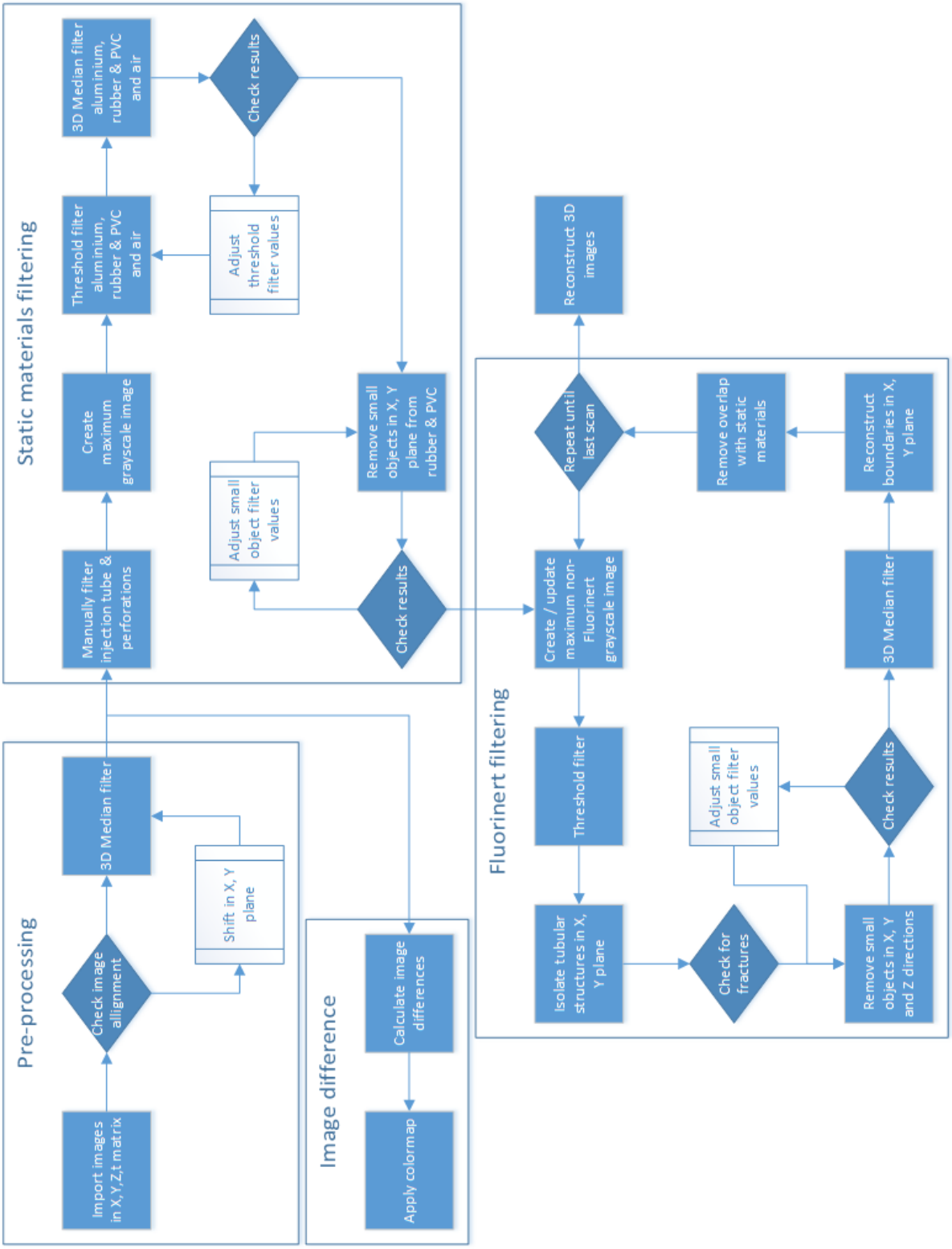

Figure 3.4: Image processing flowchart

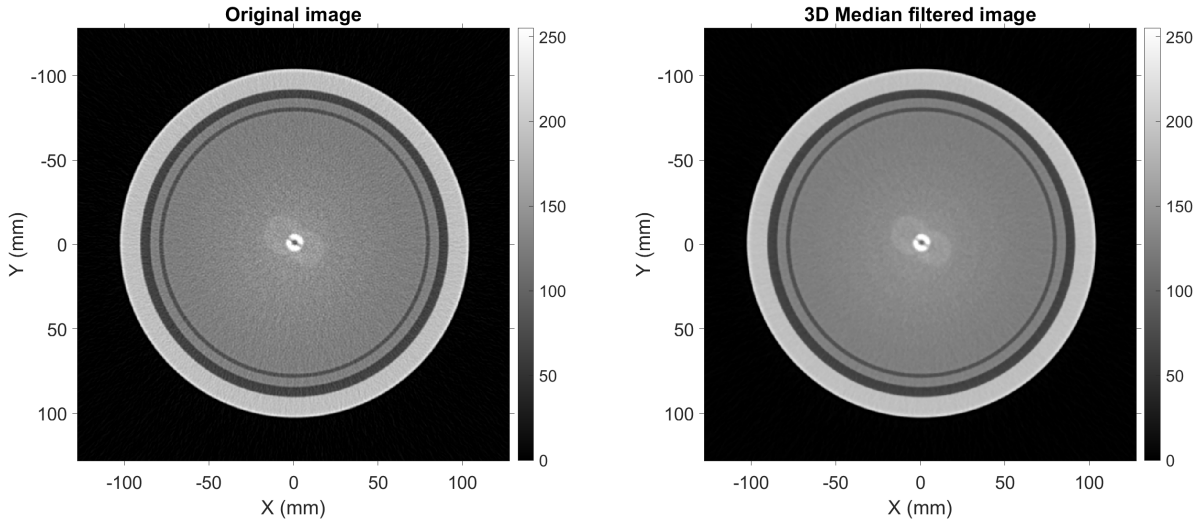

Figure 3.5: 3D Median filter result

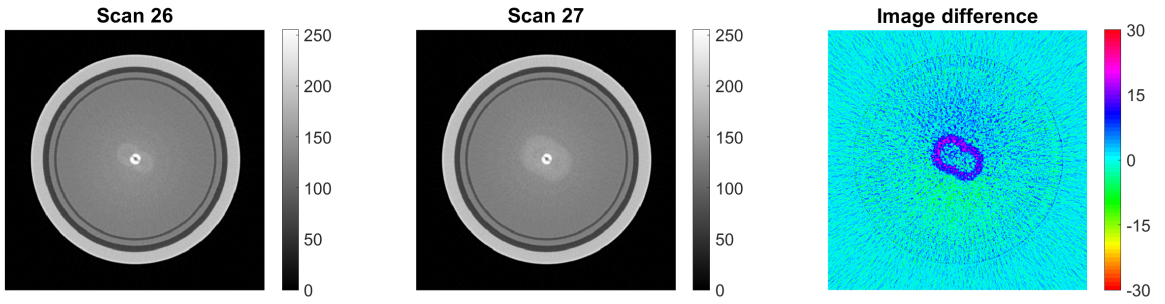

Figure 3.6: Image difference result

3.3. Static materials filter

The image processing phases for detecting and visualising static materials and the Fluorinert are split. Static materials include the aluminium frame and injection nozzle, the rubber and PVC sleeve, the air on the outside and the injection tube core & perforations. They require less processing and filtering since their position does not change over time. This allows us to use all CT scans and make only one X, Y, Z matrix per material. This process is described in the following paragraphs.

Injection tube core & perforations The first step is to detect the injection tube core & perforations. With the term core, we refer to the flow region of the injection tube and not the aluminium itself. This is the only manual process in the image-processing algorithm. The reason for this is the high sensitivity of the core to noise and artefacts previously described. It sits in the centre of the sample where x-ray energy levels are at its lowest. Next to that, screw thread of the injection tube, the transition from injection nozzle to injection tube and the internal sand filter mechanism for experiment 4 and 5 complicate the automatic detection of the core even further. Due to this, a manual selection of the injection tube core & perforation coordinates is done.

Threshold filter As previously described, all CT scans can be used to detect the static materials, since they do not move over time. To combine all images, the maximum of each pixel for all time steps is taken. The combined image is then filtered using thresholds. Typical thresholds are >190 for aluminium, <122 & >=11 for

rubber and PVC and <11 for air. Next to that, pixels that have been manually selected as the injection tube core & perforations, cannot belong to other materials. The exact values can slightly vary since the amount of noise varies per experiment. After separating the materials with the thresholds, the results are 3D median filtered. This is to remove outliers or fill gaps that did not make the threshold. The results are visualised and checked for remaining loose pixels or gaps. If gaps exist in a material, the threshold is too narrow. For aluminium this means the threshold needs to decrease, while for air this means the threshold needs to increase. If loose pixels can be observed, the threshold is too wide. The process of adjusting the threshold is repeated until no more gaps or loose pixels can be observed in any materials. Threshold values range from >188 to >191 for aluminium, <121 to <128 for rubber & PVC and <11 to <15 for air.

Small object filter One region in the CT cell typically gives some noise that cannot be solved with the 3D median filter. This is the transition area between the aluminium and the outer air. When a pixel lies on the border of aluminium to air, its grayscale will be averaged by the CT scanner, leading to stretched regions in the Z direction that fall within the rubber & PVC threshold values. To filter this, a small object filter can be applied which filters all connected pixels that are smaller than a set value. These regions can be up to 2500 connected pixels large but are still significantly smaller than the rubber and PVC sleeve so this filter can be used without any problems.

3.4. Fluorinert filter

Since the infiltration zone of the Fluorinert changes over time, a more extensive filter process is required to detect and visualise this zone accurately. An overview of the steps can be found in flowchart 3.4 and a visualization of the filter process in figure 3.7. As was mentioned at the beginning of this chapter, the sample has a natural grayscale gradient along its radial axis. Grayscale values will be higher in the middle of the sample than they are on the outer edges. When a threshold filter with a single value is applied, this filter will tend to overestimate the Fluorinert volume at the centre of the sample and underestimate it as it expands radially. To solve this problem, the scans before Fluorinert is injected can be used to map this natural grayscale gradient. By taking the maximum of each pixel before Fluorinert injection, we once again combine the information of multiple scans into one. Then instead of a value threshold filter, this combined image can be used as a threshold. Pixels higher than the maximum grayscale image before Fluorinert injection are either Fluorinert or noise. Pixels lower than the maximum grayscale image have most likely not been infiltrated yet. The density difference between the Fluorinert and water is large. Assuming a porosity of 42%, a water-saturated pixel will have an average density of 1.96 g/cm3 while a Fluorinert saturated pixel will have a density of 2.30 g/cm3. This difference is typically larger than any noise, thus using a maximum pre-Fluorinert injection grayscale image as a threshold is a good method.

The more pre-Fluorinert images are available, the better the threshold becomes. Experiments 2 and 3 however, have little to no pre-Fluorinert images. In case little images are available, the first Fluorinert images will be crude and contain a relatively large amount of noise. In case no pre-Fluorinert images are available, the Fluorinert in the first scan will have to use a threshold value rather than an image. This value will have to be manually selected and since the first Fluorinert injection zone is typically small, this does not give too many problems. To increase the quality of the threshold filter over time, the maximum grayscale image is updated with every scan. Pixels that have been determined to not contain any Fluorinert, will be added to the maximum grayscale image. For pixels that have been identified as Fluorinert saturated, the maximum grayscale image will remain the same. This process is especially crucial for experiments where little pre-Fluorinert injection scans are available and reduces the noise over time significantly. Figure 3.8 shows the maximum grayscale image at the end of the image processing of experiment 4. The radial rings with different shades of grey are clearly visible here.

Hessian-based multiscale filter One problematic type of noise is the combination of Poisson noise and zebra artefacts. These are particularly hard to filter when little to no pre-Fluorinert injection images are available. The effect of these types of noise are visible in the top centre image of figure 3.7, which shows the result of the threshold filter of experiment 3. They form elongated and tubular structures along the radial axis. If these structures were not connected with the main Fluorinert infiltration zone, then a small objects filter could take care of this type of noise. Unfortunately, this is often not the case and a string of pixels in the 3D plane typically connects these structures to the main infiltration zone.

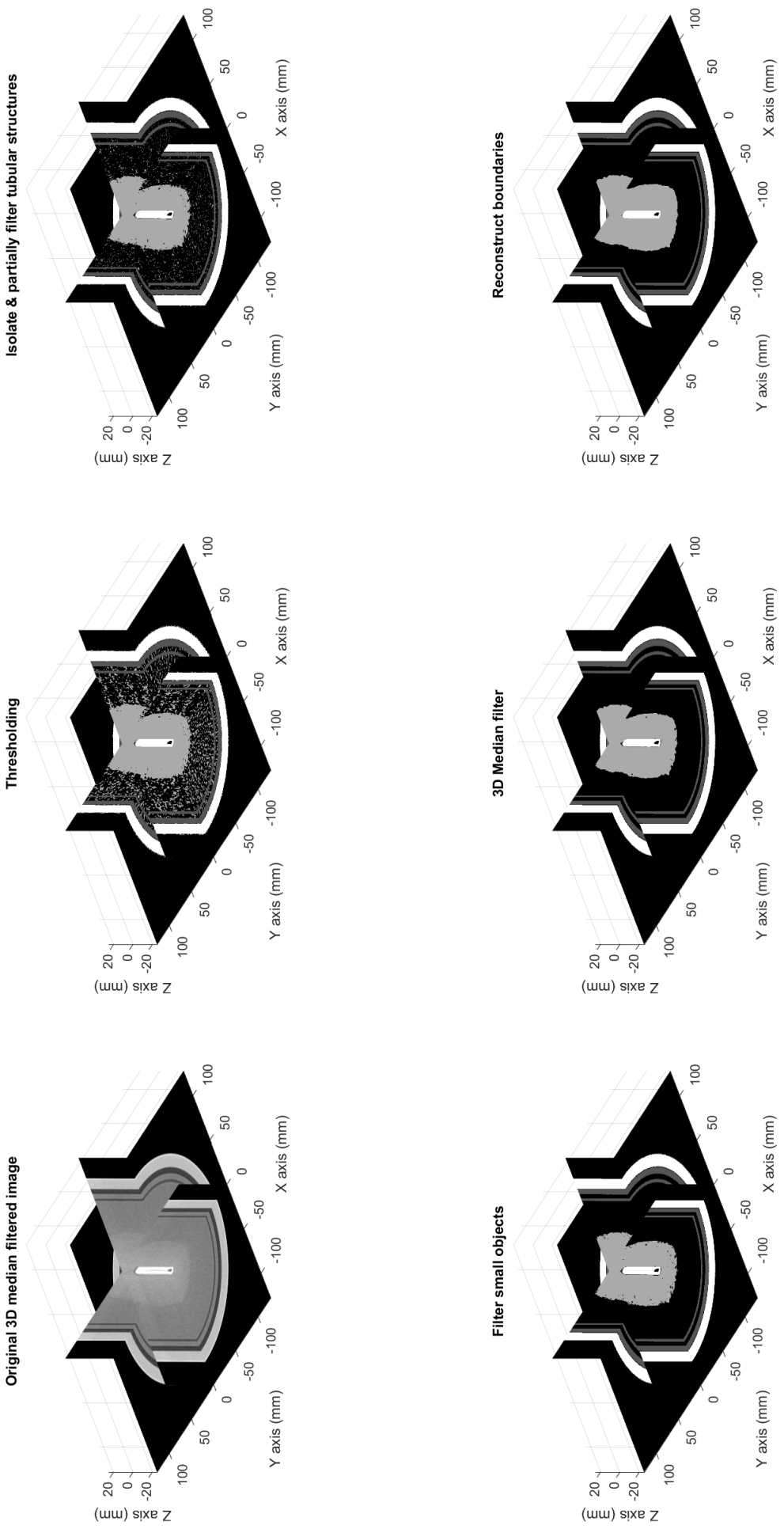

Figure 3.7: Fluorinert filter process

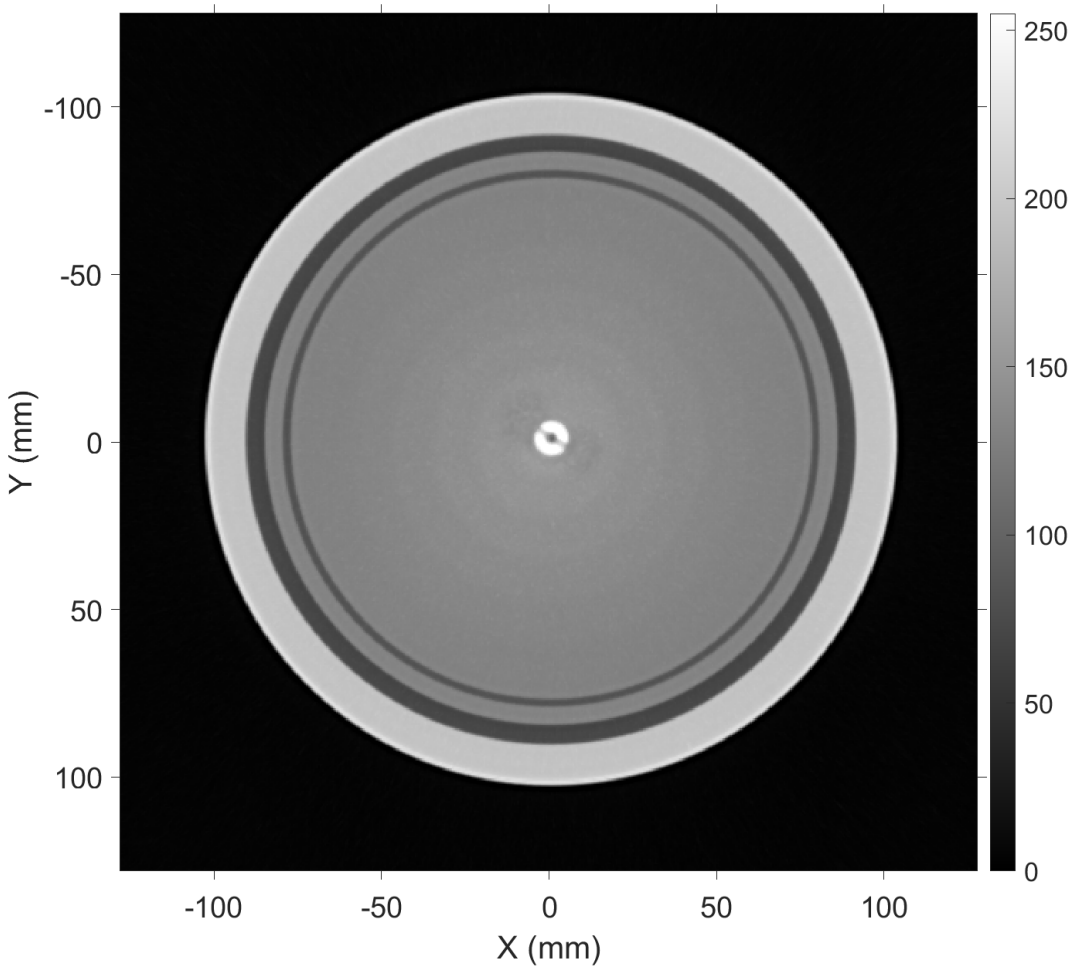

Figure 3.8: Maximum grayscale image

To filter these structures a new type of filter is introduced which is a Hessian-based multiscale filter. In the medical world this filter is used to enhance blood vessels and is able to detect elongated and tubular structures. The filter searches for tubular structures of a specified thickness and returns the border of these structures. Structures with a similar thickness as the specified thickness get a high grayscale value (white) border and structures which are tubular but thicker get a lower grayscale value (grey to dark grey) border. By specifying the filter thickness, we can control the process and determine what we classify as noise. A manual check of the filter results is required, to ensure no fractures are filtered in the process. The filter is applied in the X,Y plane and its results are subtracted from the threshold filter result. This way, all borders of the tubular structures are filtered and this opens the way for a small object filter. See figure 3.7 for a visualization of this process.

Refining What remains is applying a small object filter and a 3D median filter which are previously described in section 3.3. However, the small object filter is not applied in 3D, but one time in each plane. The X, Y plane is treated first, then the Y, Z plane and finally the X, Z plane. This way the small object filter value can remain low which has shown to give better results in combination with the Hessian-based multiscale filter. The 3D median filter is applied to remove any remaining noise. Finally, the boundaries of the infiltration zone are reconstructed with one row of pixels, since these were filtered during the Hessian-based multiscale filter process. To do so the same filter is applied but now added to the results rather than subtracted. A final check is done to see if there is no overlap of the Fluorinert infiltration zone with the other static materials. Any overlap is removed from the Fluorinert interpretation. This process is repeated for each time step, updating the maximum grayscale image with every iteration.

4

Performance, results and discussion

4.1. Experiment 1 - Viscasil

Injection fluid	Viscasil 500M
Injection pump	Air stroke pump + intensifier
Support injection pump	1000D Syringe pump
Injection system	Open borehole with notch
Axial pressure	3.5 MPa
Radial pressure	2 MPa
Backpressure	0.2 MPa
Max flowrate	20.1 ml/min
Max injection pressure	39.4 MPa
# CT scans	0

Table 4.1: Experiment 1 - Overview

The objective of the first experiment is to test the equipment and successfully create fractures with a high viscosity fluid. The experiment procedures are tested and problems resolved before we move on to low viscosity fluid injection in the CT scanner. For the injection fluid, Viscasil 500M is used and dyed purple so its infiltration zone is visible when the sample is excavated. Since the high viscosity fluid will require high pressures to inject, the air stroke pump in combination with the intensifier is used. For the injection system, an 8 cm open borehole interval is created with the notch to create an initial fracture direction. To prevent the open borehole from collapsing before injection, the Viscasil in the borehole is pressurized to 0.2 MPa with the support injection pump, equal to the backpressure supplied by the pore fluid system. Once injection starts, the injection pump switches from the ISCO pump to the intensifier.

Pre-injection As described in the previous chapter, the sample is loaded in two phases. The first phase loads the sample to 1.5 MPa axial pressure and 1 MPa radial pressure. During these loading phases, pore water flows out of the sample as it is compacted. After the first loading phase, the open borehole interval is created by slowly retracting the injection tube. Due to a slightly higher backpressure than the borehole pressure, some pore water flows back into the sample as the injection tube is being retracted. Once an 8 cm interval is reached, the final loading phase can begin to increase the pressure to 3.5MPa axial pressure and 2 MPa radial pressure. At the end of this loading phase, the borehole pressure is also corrected to 0.2 MPa, to keep the system stable.

Injection An overview of all the data logged by the data acquisition system can be found in figure 4.1. Three injection cycles were performed during the experiment. During the first injection cycle, an injection rate of 45 ml/min was attempted. For the second and third injection cycle, the injection rate was halved to 22.5 ml/min. Looking at the pore fluid outflow rate, these injection rates were never met. The air stroke pump and intensifier could not deliver an injection pressure large enough for the high viscosity Viscasil reach such

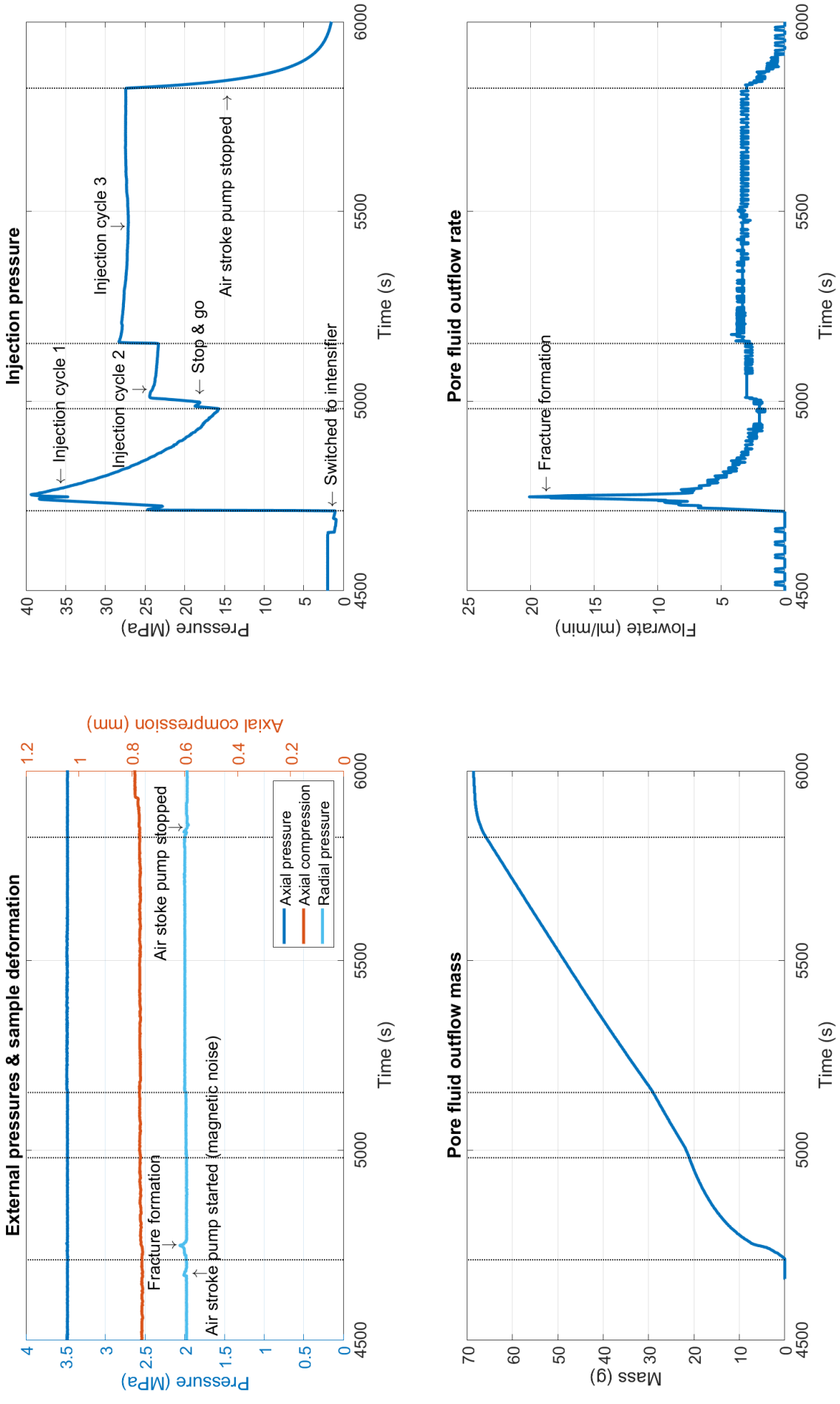

Figure 4.1: Experiment 1 - Data aquisition

injection rates. Using a steady state radial flow equation [4.1], the required pressure for the fluid to infiltrate the sample can be roughly approximated. Note that this is a rough estimation, meant to give an order of magnitude of the injection pressure required.

$$P_{bh} = P_R + \frac{Q\mu B}{2\pi kh} \ln \frac{r_e}{r_w} \tag{4.1}$$

Where: P_{bh} = Borehole pressure [Pa]
P_R = Backpressure [2×10^5 Pa]
Q = Injection rate [m^3/s]
μ = Viscosity [505.2 Pa s]
B = Formation volume factor [1 m^3/m^3]
k = Permeability [4.93×10^{-12} m^2]
h = Infiltration length [8×10^{-2} m]
r_e = Infiltration radius [7.6×10^{-2} m]
r_w = Borehole radius [5×10^{-3} m]

In addition, the pressure drop in the injection system, mainly along the thin injection tube, can be approximated using the Hagen-Poiseuille equation [4.2].

$$P_{is} = P_{bh} + \frac{8\mu LQ}{\pi R^4} \tag{4.2}$$

Where: P_{is} = Injection system pressure [Pa]
L = Injection tube length [33×10^{-2} m]
R = Injection tube radius [1×10^{-3} m]

This pressure drop needs to be taken into account since the injection pressure sensor sits in front of the injection tube, leading to a difference between the borehole pressure and the measured injection pressure.

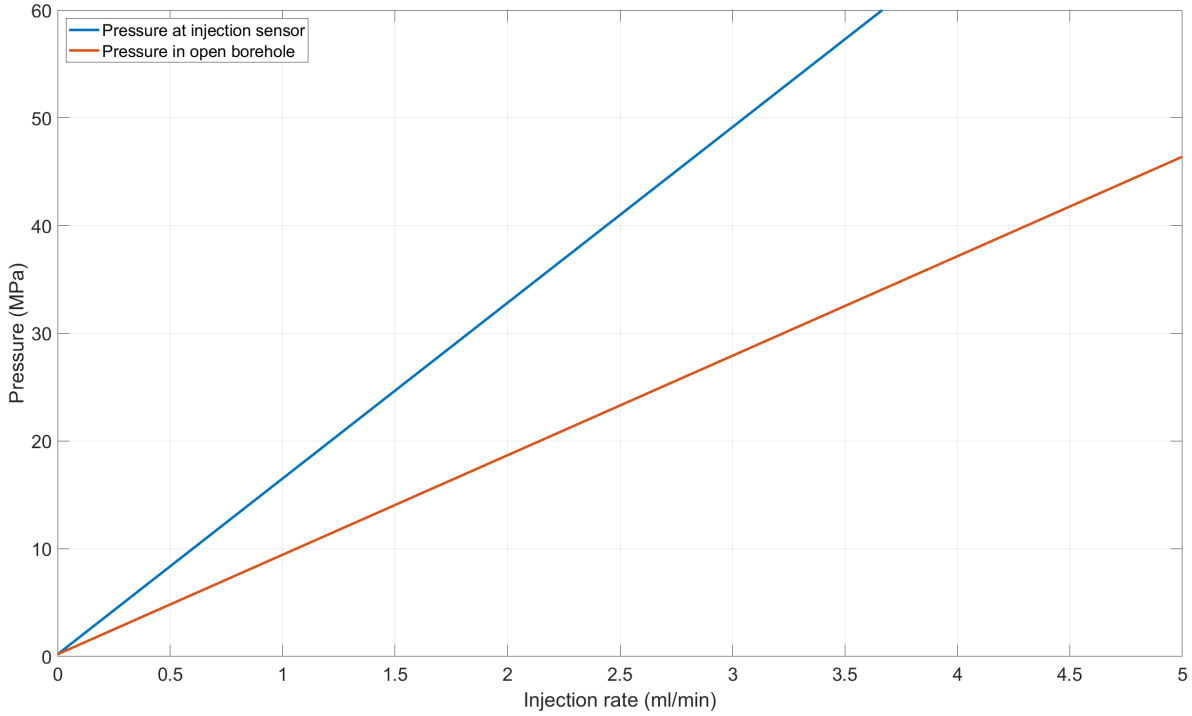

Figure 4.2: Experiment 1 - Injection pressure - rate relation estimation

From figure 4.2 we can conclude that high injection pressures are required to let the Viscasil infiltrate the sample.An injection pressure of 40 MPa would lead to an injection rate of 4 ml/min. However, looking at the data aquisition results, we see a fracture being formed during injection cycle 1. Figure 4.3 shows a fracture

being created at 4748 seconds and possibly another one at the 4725 time mark. The injection pressure drops at these times, while the pore fluid outflow rate increases. The fracture can also be observed by looking at the radial pressure, which shows a clear peak as well.

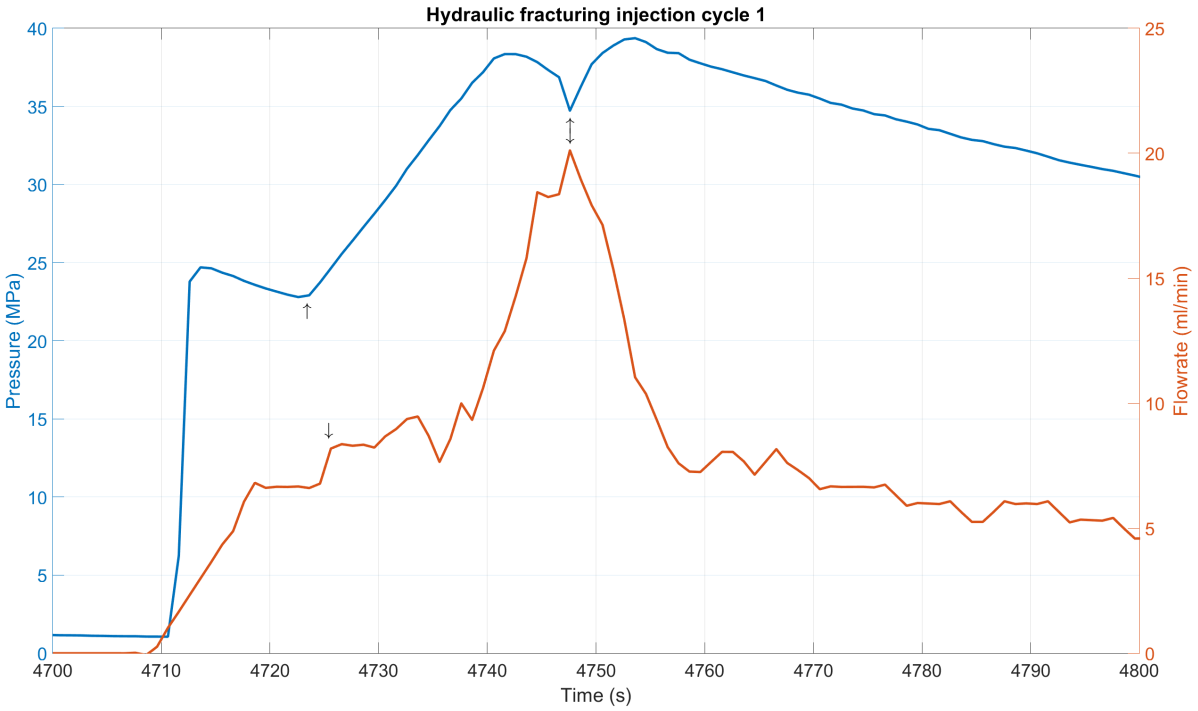

Figure 4.3: Experiment 1 - Injection cycle 1 detail

Injection cycle 1 was stopped once a pressure of 39.4 MPa was reached, after which a leak-off period can be observed. Injection cycle 2 was limited to a pressure of 24.4 MPa by the air stroke pump and included a short pause at the beginning. Lastly, for injection cycle 3, the pressure limit was increased to 28.3 MPa and injection continued for a longer time than previous cycles. A total of 69.1 ml Viscasil was injected.

Sample excavation Since no CT scans were made for this experiment, a careful sample excavation was performed. The Viscasil was dyed purple beforehand to visualise the infiltration zone. Along the open borehole interval, several fractures were created and can be seen in the figures of 4.4.

Around the open borehole and at the end of the fractures, a darker purple colour can be observed indicating a higher Viscasil saturation or a segregation of the dye. This indicates that the injection fluid has a high preference to infiltrate the formation at the fracture tip, rather than along the fracture body. This is most noticeable in figure 4.4a where it seems almost no Viscasil has deposited along the fracture length. The infiltration zone has the shape of a 6cm diameter cylinder along the borehole length, with some fluid infiltrating above and below the borehole interval. The open borehole was still intact and did not collapse when the sample was being excavated.

Micro CT scans A part of the sample was carefully preserved to better visualise the fractures with the use of a micro CT scanner. In this process, the sample is quite heavily disturbed because the sample needs to be pulled off the injection tube. However, fracture directions and fluid infiltration zones are still visible after this process and can be seen in the figures of 4.5.

The open borehole originally had a notch, which either collapsed during the loading phases of the experiment or after the borehole was no longer pressurized and the sample was excavated. It is still visible in the micro CT scans, leaving behind a white high-density region in the NE - SW direction. The main fracture direction has the same orientation as the notch, however fractures were created in all directions along the borehole length. The largest fracture can be observed in figure 4.5a, with a length of almost 1 cm and a width of 2 mm. The borehole has expanded and been deformed in several directions along the borehole length.

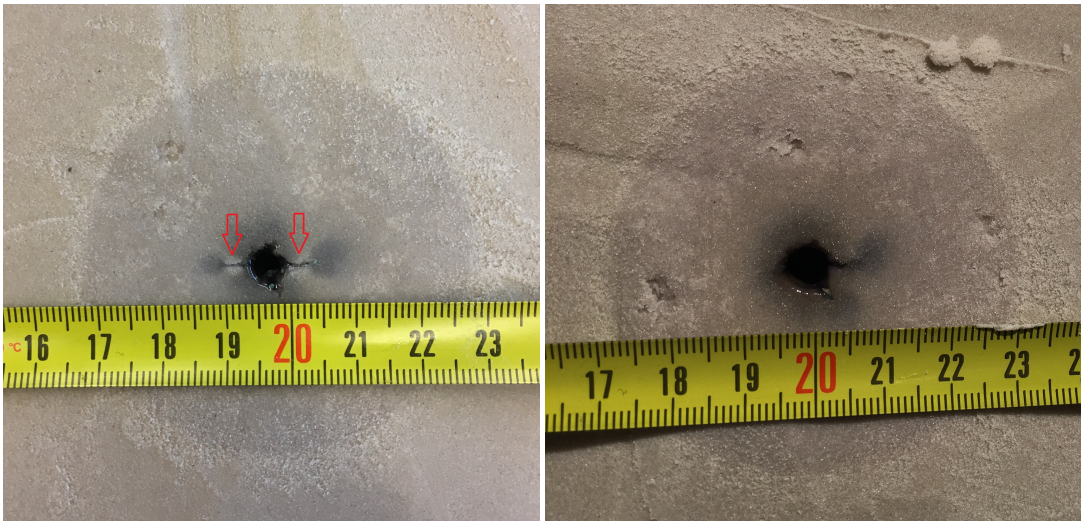

(a) (b)

Figure 4.4: Experiment 1 - Fracture photos

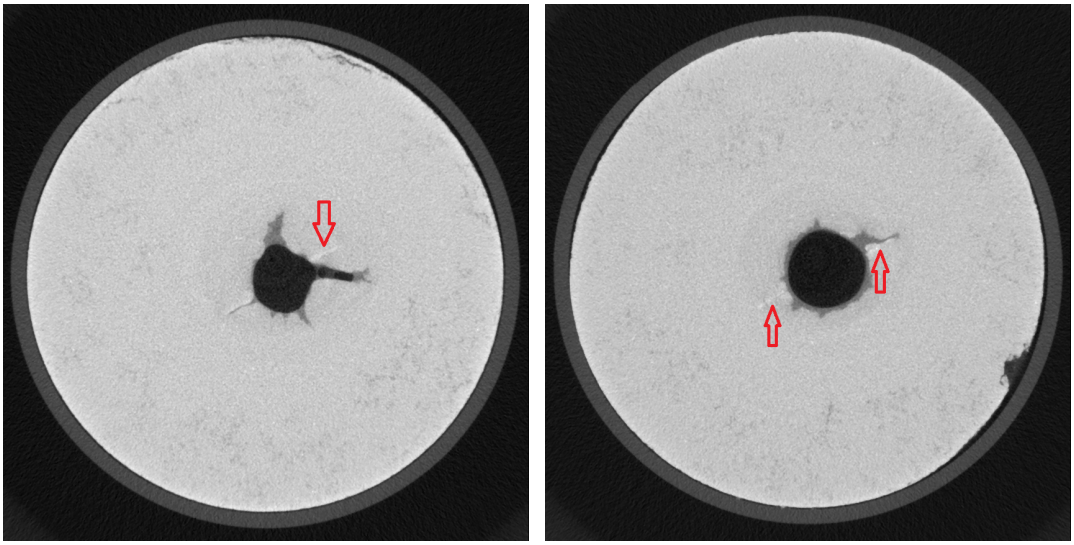

(a) (b)

Figure 4.5: Experiment 1 - Micro CT fracture photos

4.2. Experiment 2 - Low flowrate Fluorinert

Injection fluid	Fluorinert FC-770
Injection pump	1000D Syringe pump
Injection system	Two 1 mm diameter perforations
Sand filter	-
Axial pressure	3.5 MPa
Radial pressure	2 MPa
Backpressure	0.2 MPa
Max flowrate	46.7 ml/min
Max injection pressure	12.8 MPa
# CT scans	20

Table 4.2: Experiment 2 - Overview

After successfully testing the equipment and fracturing the sample in experiment 1, we switched to low viscosity fluids. Experiment 2 is the first experiment in the CT scanner and to visualise the injection fluid the high-density Fluorinert is used. Axial, radial and backpressure are kept the same as in experiment 1. Since no high injection pressures are expected when using low viscosity fluids, the 1000D syringe pump is used which can handle pressures up to 13.79 MPa and flowrates up to 408 ml/min. To increase fracturing chances, an injection system with two opposite perforations is used with a small diameter of 1 mm. The smaller the perforations the larger the local velocity and pressures are. The CT scans are made during the injection cycles and scan an interval of 5 cm along the injection tube. The perforations are positioned in the middle of the 5 cm interval. In total, five injection cycles took place, of which the first four were injection rate controlled and the last one was pressure controlled. No sand filter was used for this first low viscosity fluid experiment.

Data aquisition system Output of the DAS system can be found in figure 4.6. During the first 250 seconds, the second loading phase takes place where the axial and radial pressure is increased from 15 and 10 MPa to 35 and 20 MPa respectively. As the pressure on the sample is increased, pore fluid flows out of the system. Next to that, the LVDT measures the axial compression, which shows a deformation of 0.52 mm as the axial pressure is increased.

The first two injection cycles attempted to inject 408 ml/min, the highest flowrate that the ISCO pump can deliver. Both were pre-emptively stopped by the injection pump, since the injection pressure exceeded the pump pressure limit. The same goes for injection cycle three, where 400 ml/min injection was attempted and for injection cycle four where two times an injection of 300 ml/min was attempted. The pressure limits of 13.79 MPa are not detected by the injection system pressure sensor. This is most likely because the ISCO pump shuts off and reduces its pressure so quickly, that the sampling frequency of 1 second of the pressure sensor misses the actual pressure peak. For the last injection cycle, a constant pressure of 11.9 MPa was applied by the pump, resulting in a flowrate of 46 ml/min. The injection pressures were much higher than expected beforehand. Upon further research, it was concluded that the injection tube was clogged up with sand. Sand was found in the injection tube when the sample was excavated and the use of the right sand filter in future experiments prevented such problems. Since the injection pressures were large from the start, sand infiltrated the injection tube either during sample preparation or during the loading phases. Regardless of the injection problems, a total of 138.2 ml of Fluorinert was still injected, mainly during injection cycle four and five. Because of the clogged injection tube, the high pressures most likely did not reach the sand phase.

CT scanner The use of Fluorinert allows us to visualise the infiltration area of the injection fluid in the CT scanner. If any high permeability channels or fractures were formed, the injection fluid should have a flow direction preference. Figure 4.7 shows the first CT scan at the height of the perforations on the left side. It shows a lower density region just right of the injection tube. Since the sample preparation method we use has proved to give reliable homogeneous samples, a region like this is most likely due to sample disturbance. The injection tube could have been hit while transporting the vessel to the CT scanner, disturbing one side of the sample along the injection tube. The image on the right side of figure 4.7 shows the first visible Fluorinert in the sample at the height of the perforations. It is clear that the Fluorinert has a preference to accumulate in the lower density region. What is also visible is that bottom side perforation is clogged, since no Fluorinert can be observed here. This is better visible in a 3D re-construction as shown in figure 4.8 and 4.9.

The scans that follow show that the bottom perforation is no longer fully clogged and that the Fluorinert distributes in a spherical shape through the sample as in figure 4.10. The injection pressure is still large, suggesting that sand is still clogging the injection tube, rather than the perforations itself. No preferred flow directions can be observed except for the low-density region at the start.

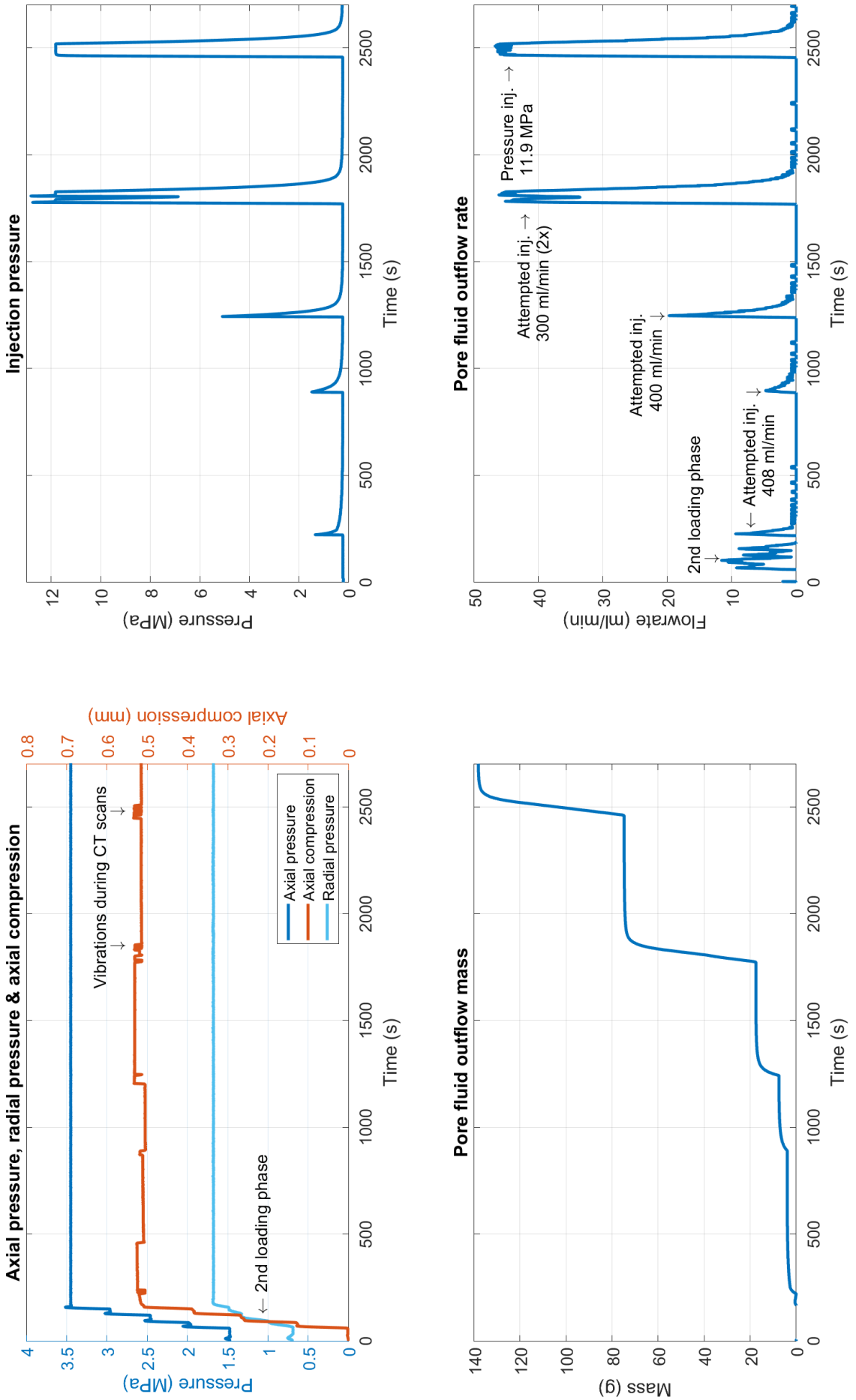

Figure 4.6: Experiment 2 - Data aquisition

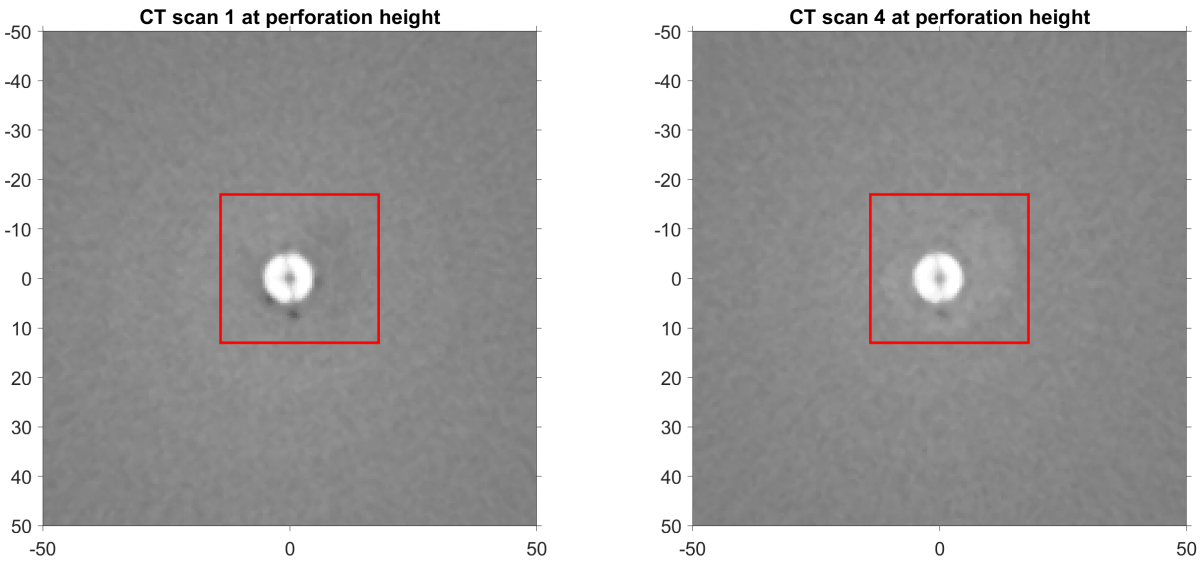

Figure 4.7: Experiment 2 - Low density region

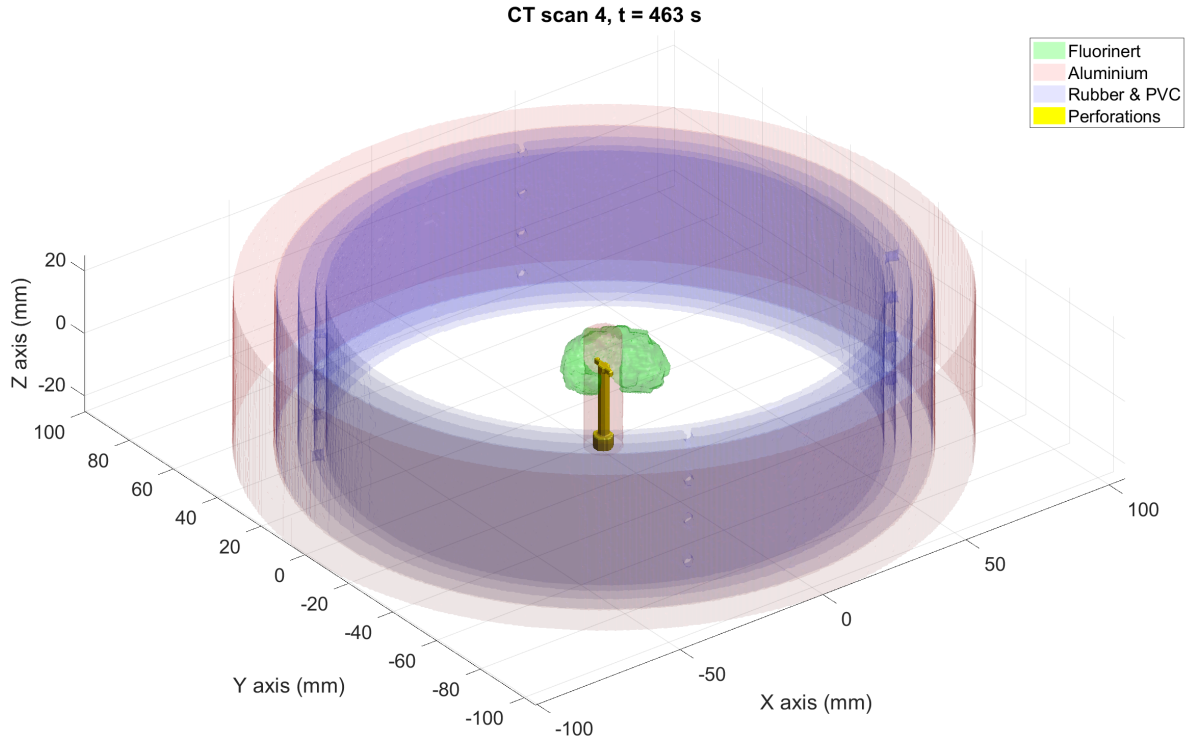

Figure 4.8: Experiment 2 - Fluorinert scan 4 - 3D view

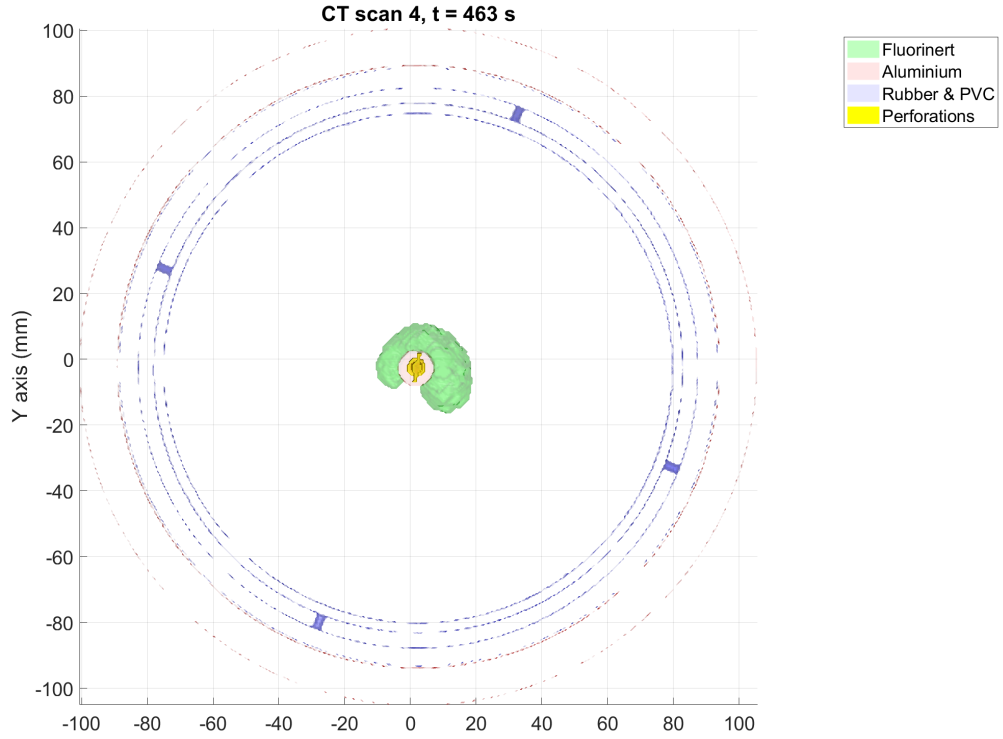

Figure 4.9: Experiment 2 - Fluorinert scan 4 - Top view

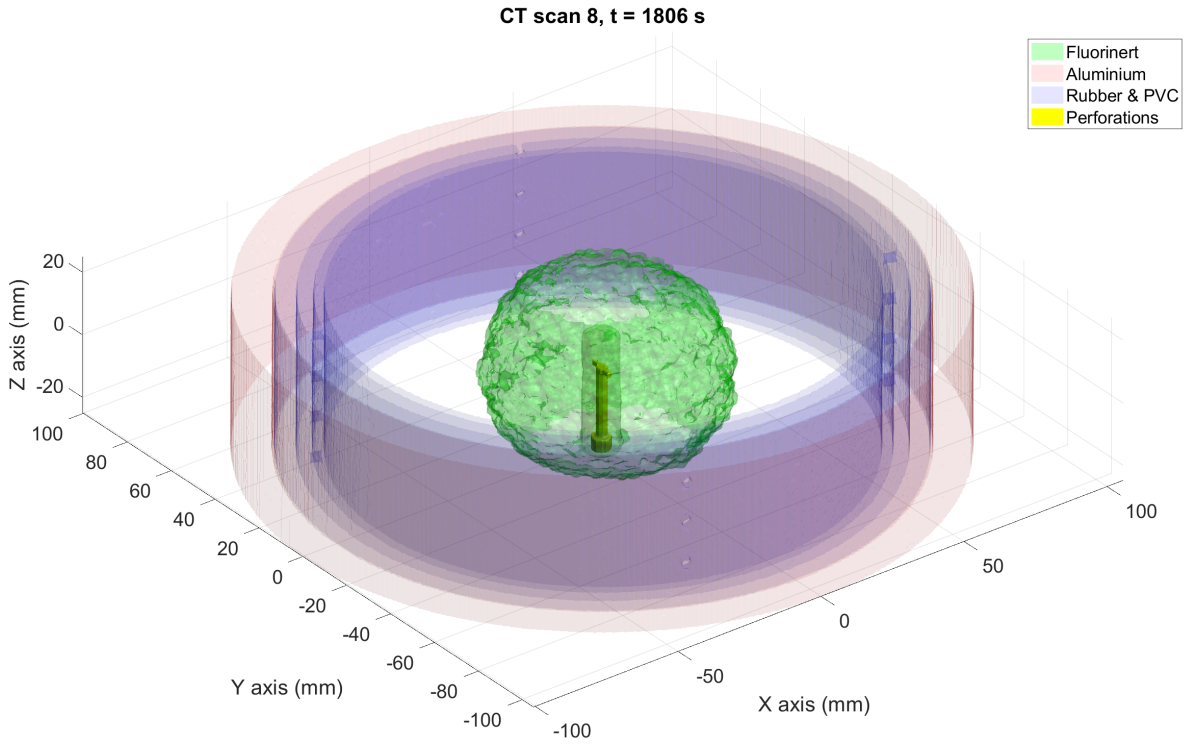

Figure 4.10: Experiment 2 - Fluorinert scan 8 - 3D view

4.3. Experiment 3 - High flow rate Fluorinert

Injection fluid	Fluorinert FC-770
Injection pump	Air stroke pump + intensifier
Support injection pump	1000D Syringe pump
Injection system	Two 1 mm diameter perforations
Sand filter	180 micron sand screen
Axial pressure	3.5 MPa
Radial pressure	2 MPa
Backpressure	0.2 MPa
Max flowrate	2460.9 ml/min
Max injection pressure	30.0 MPa
# CT scans	9

Table 4.3: Experiment 3 - Overview

Experiment 2 results showed that a sand filter was necessary to prevent sand inflow into the injection tube and/or perforations. Therefore, an external sand filter was placed in front of the perforations for experiment 3. The sand filter consisted of a filter cloth with 180-micron wide square slots and was wrapped around the injection nozzle. To prevent the pre-emptively shutdown of the injection cycles, a switch was made to the air stroke pump in combination with the intensifier, to be able to provide higher injection pressures. Also, since no fractures were observed using the relatively low injection rates of experiment 2, higher injection rates were used for this experiment. The axial, radial and backpressure were not changed in comparison to previous experiments. Fluorinert FC-770 was once again used to visualise the infiltration region of the injection fluid. Before every injection cycle, the injection system was pressurized to 0.2 MPa to prevent backflow from occurring when the main injection valve is opened. Three injection cycles took place, the first lasting 15 seconds with an injection rate of 600 ml/min. The second with an injection rate of 1000 ml/min, also for 15 seconds and the last with an injection rate of 2400ml/min for 5 seconds.

Data acquisition system Figure 4.11 shows the output of the data acquisition system of the first two injection cycles. There is a significant difference between the injection rate and the pore fluid outflow rate during the first injection cycle. The injection rate is deduced from the position of the piston of the intensifier. If all the equipment and sensors function correctly, it is possible to recognize whether a difference in the volume injected and the mass outflow is either due to air in the system, or due to sample expansion. If there is air in the pore fluid outflow system, then the mass recorded does not translate properly into the outflow volume. When the sample expands, the injected volume is partially stored within the newly created sample volume, rather than flow into the pore fluid outflow system. Looking at the axial deformation records however, we can conclude that the sample does not expand in the axial direction. Upon further research, it has been concluded that in experiment 2 the intensifier was not functioning properly and was leaking internally. During the first injection with a high-pressure response, part of the injection fluid leaked instead of being injected.

Looking at the second injection cycle, a large drop in injection pressure can be observed even though the injection rate is higher than the previous injection cycle. We can conclude that the injection tube was partially clogged during the first injection cycle and the blockage was blown out either during the first or at the start of the second injection cycle. The sand screen reduced the problem but did not fully prevent any clogging of the injection tube and/or perforations. Some magnetic noise again has been observed in the radial pressure records when starting and stopping the air stroke pump.

The final injection cycle can be observed in detail in figure 4.11. A small delay between the pore fluid outflow rate and the injection rate can be observed due to the compressibility of the Fluorinert. A response to the high injection rate can be seen in the axial and radial pressure. Indicating that the pressure drop inside of the sample also influences the sample boundaries. The pumps delivering the axial and radial pressure are set to a constant pressure and adjust to the pressure fluctuations with some delay.

CT scanner A total of 9 CT scans were made during the experiment. The moments that the scans are made are visible in the vibrations of the axial LVDT. 4 Scans were made during the first injection cycle and 5 during the second. At the time of the experiment it was chosen not to make any scans during the last injection cycle,

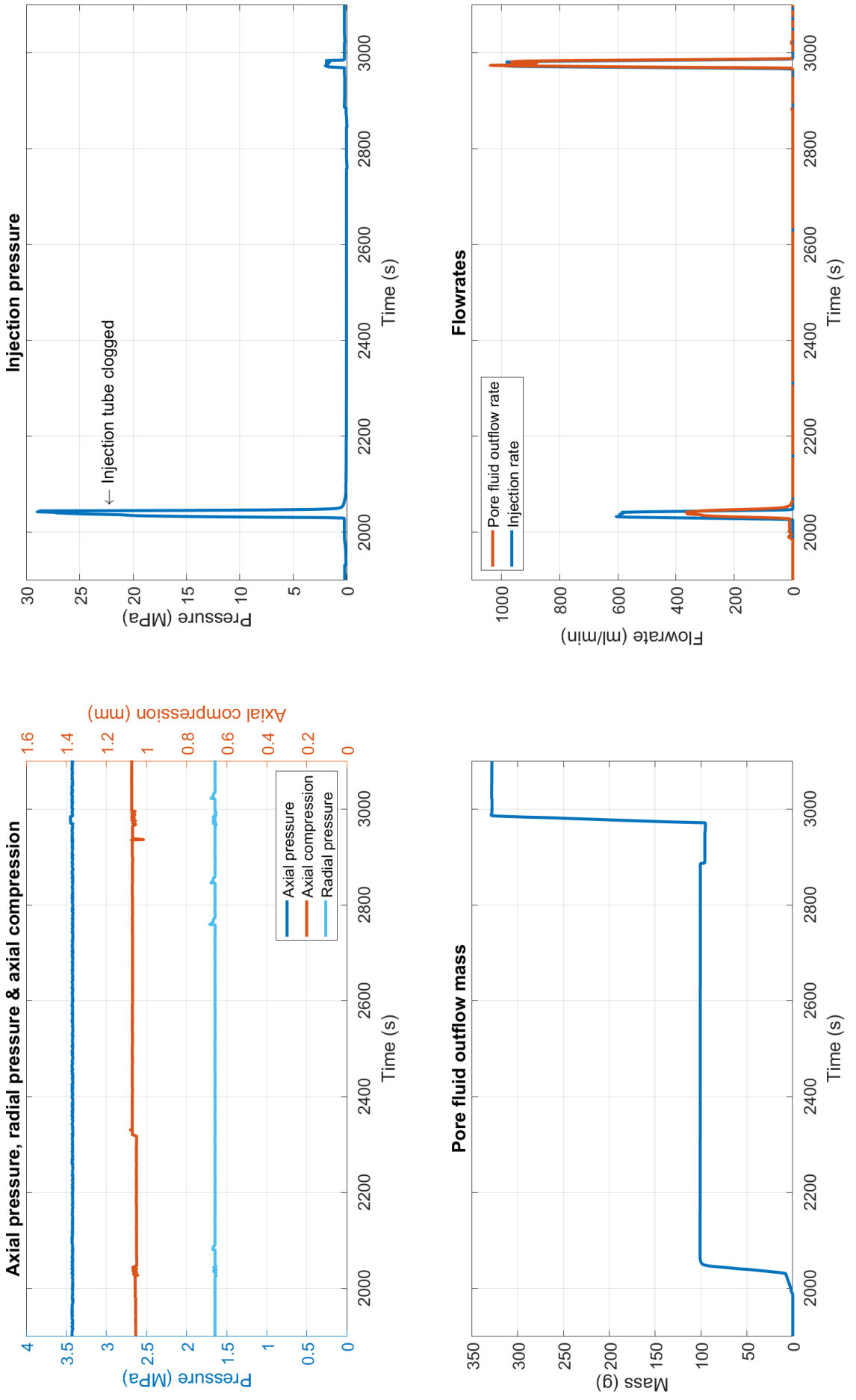

Figure 4.11: Experiment 3 - Data aquisition injection cycle 1 & 2

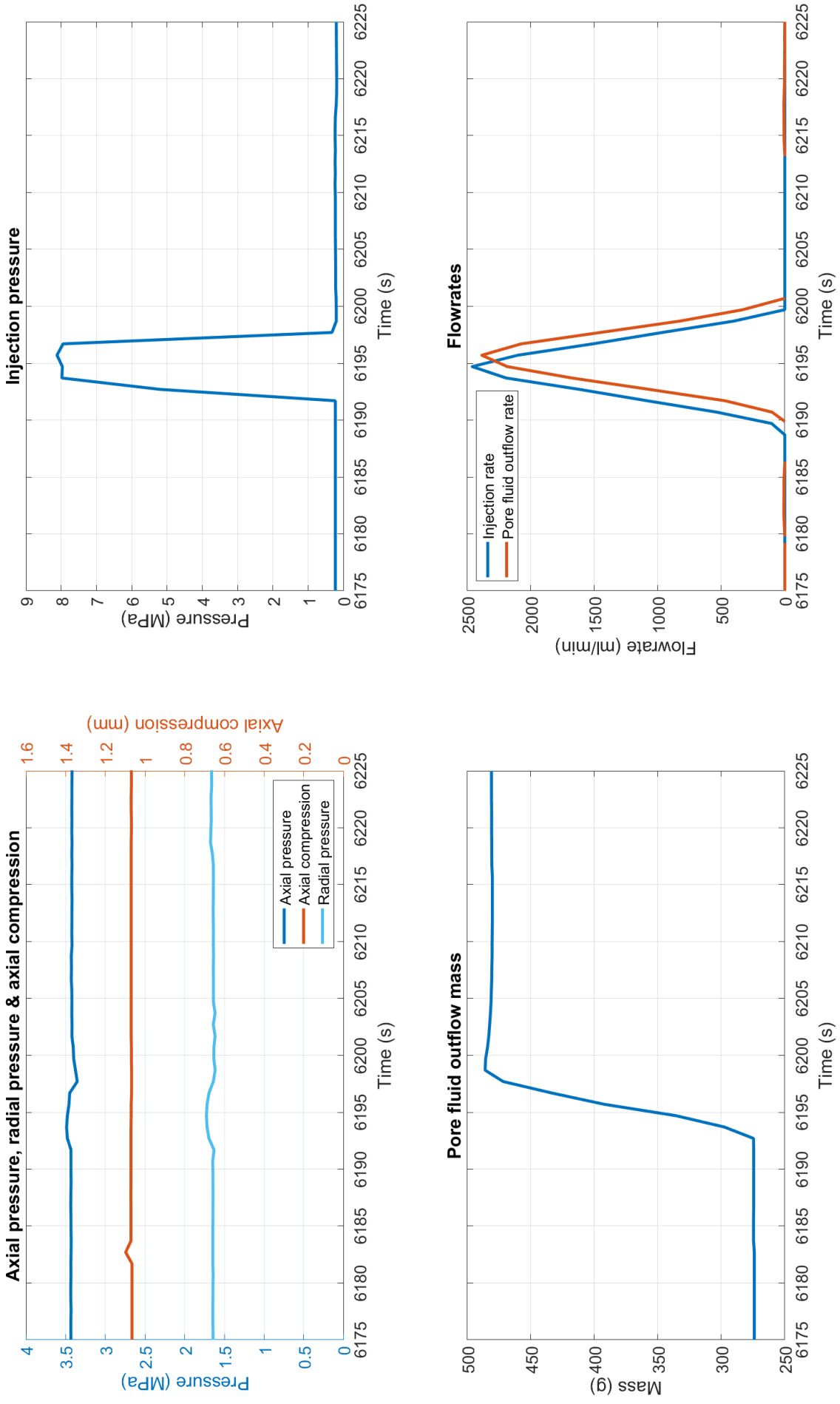

Figure 4.12: Experiment 3 - Data aquisition injection cycle 3

since the scan interval was already almost fully saturated with Fluorinert. Image 4.13 shows the Fluorinert reconstruction of the first CT scan. The injection fluid prefers to flow along the injection tube in the axial direction at first. This is a significant difference compared to experiment 2, where the initial flow direction was spherical rather than cylindrical. Scans 2 and 3 in figure 4.14 and 4.15 respectively, show that the infiltration zone transforms from a cylinder into a sphere over time.

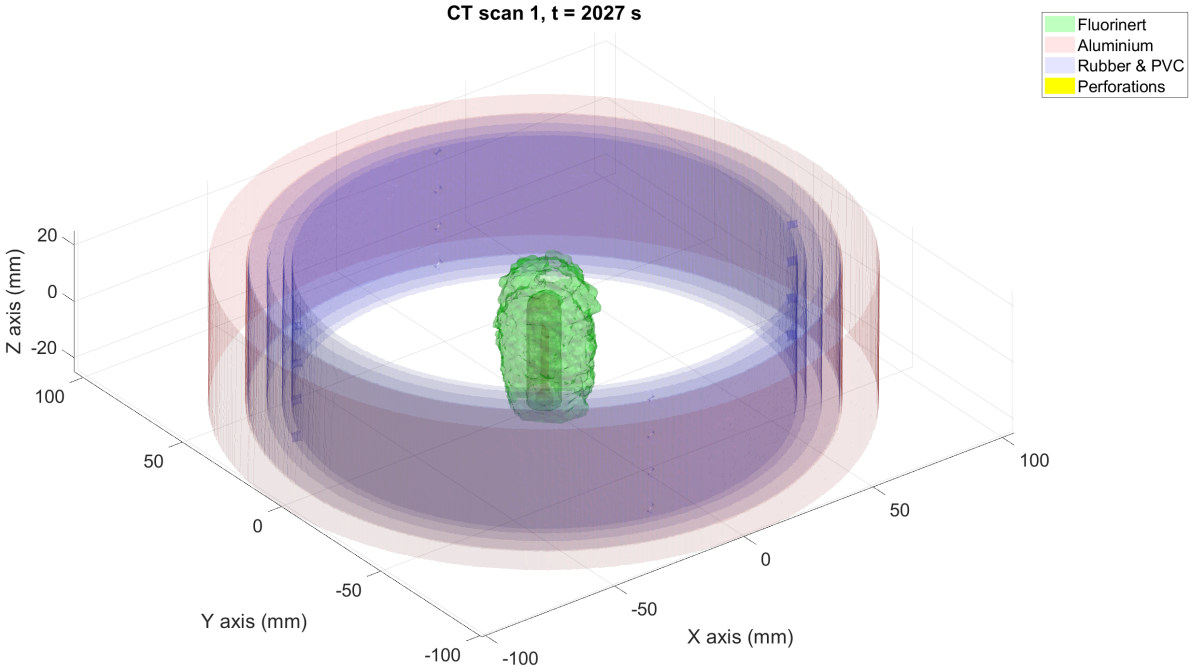

Figure 4.13: Experiment 3 - Fluorinert scan 1 - 3D view

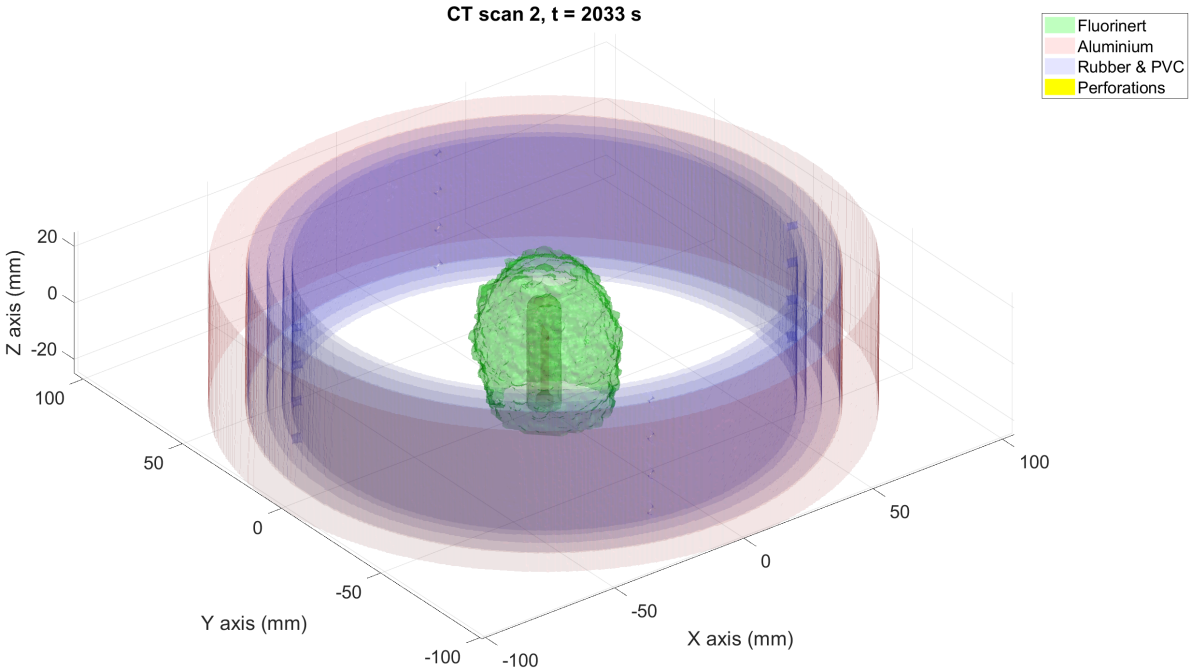

Figure 4.14: Experiment 3 - Fluorinert scan 2 - 3D view

Figure 4.16 shows the density difference between the last scan of the first injection cycle and the first scan of the second injection cycle. Dark blue colors indicate an increase in density while green colors indicate

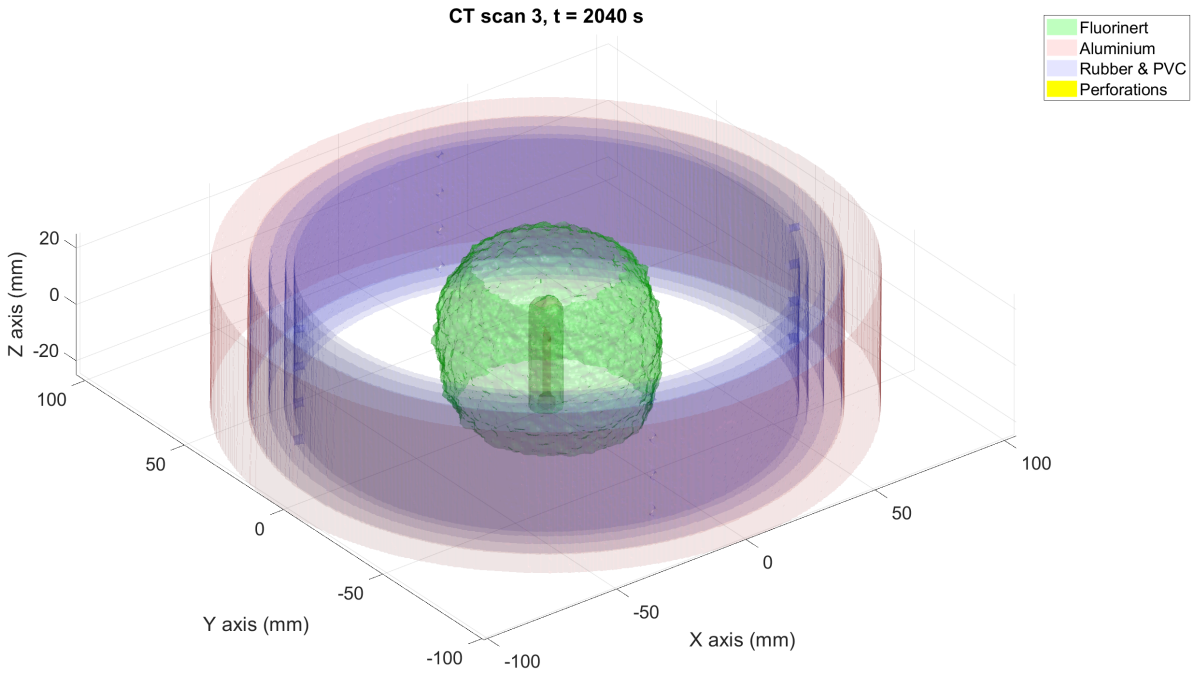

Figure 4.15: Experiment 3 - Fluorinert scan 3 - 3D view

a decrease in density. It can be observed that the Fluorinert creeps through the sample due to gravity in between the injection cycles. The blue colours in the infiltration zone show that the Fluorinert saturation decreases and mobilises downwards during the approximately 15 minute time span where no injection takes place. However, in the subsequent CT scans and in figure 4.17 which is the last CT scan, a clear preference can be seen for the bottom perforation. This preference is not observed in the first 4 CT scans. The effect of gravitational pull would be more notable at lower injection rates rather than at high injection rates. This could indicate that the top perforation is still partially clogged during the second injection cycle.

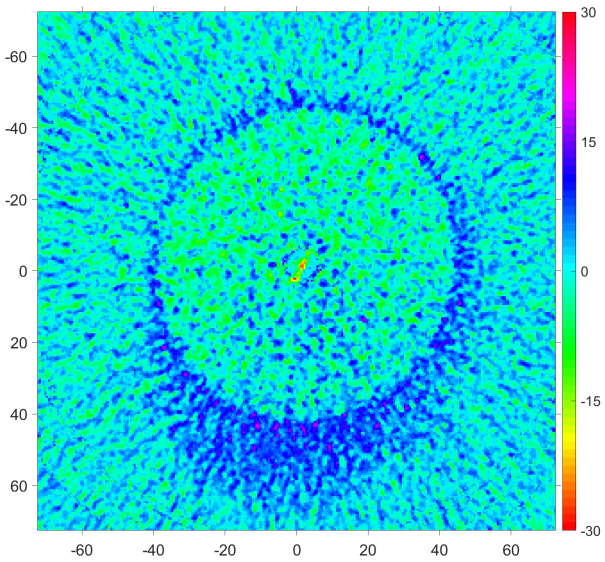

Figure 4.16: Experiment 3 - Image difference scan 4 & 5 at peforation height [Grayscale]

Figure 4.18 shows the average grayscale of the injection tube. As the Fluorinert injection starts, the density in the partially water filled injection tube goes up, with the highest density to be observed at scans 3 and 4. The subsequent CT scans of the second injection cycle show a lower average density in the injection tube. This

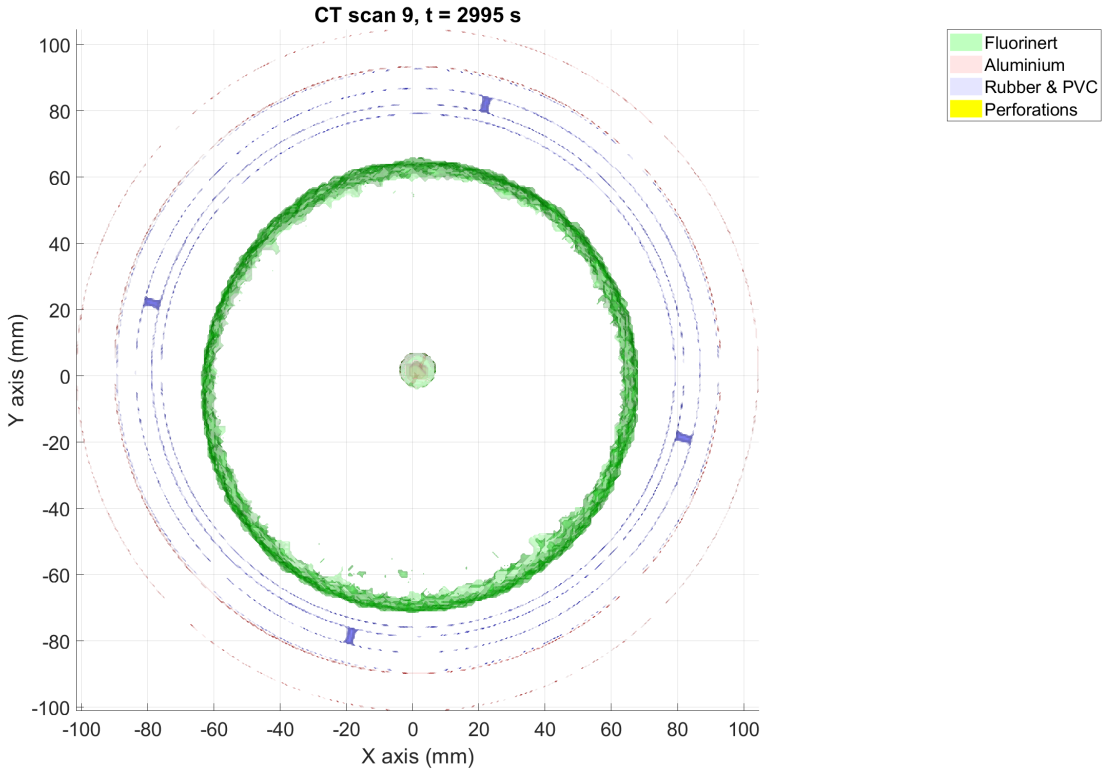

Figure 4.17: Experiment 3 - Fluorinert scan 9 - Top view

could serve as additional evidence that the sand particles that were blocking the injection tube during the first injection cycle, were (partially) blown out at the end of the first injection cycle.

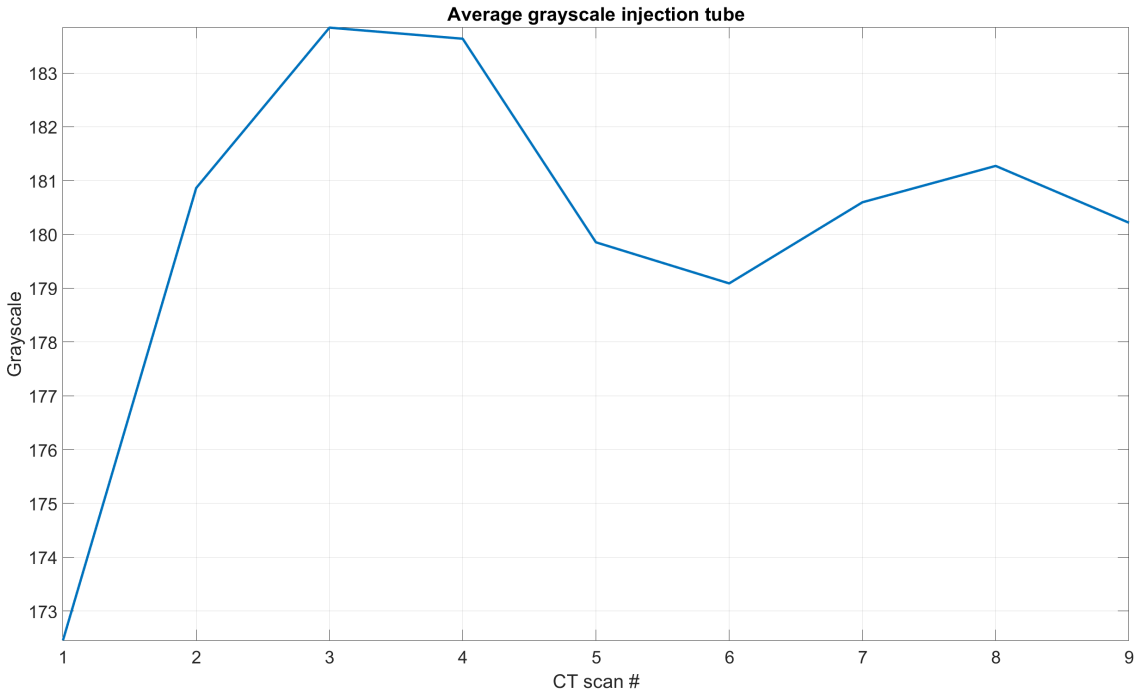

Figure 4.18: Experiment 3 - Average grayscale injection tube

4.4. Experiment 4 - Quartz powder

Injection fluids	Water
	Water + quartz powder
	Fluorinert FC-770
Injection pumps	Dual 500D syringe pump
	65D Syringe pump
Injection system	Two 1.5 mm diameter perforations
Sand filter	Rubber pin
Axial pressure	3.5 MPa
Radial pressure	2 MPa
Backpressure	0.2 MPa
Max flowrate	25 ml/min
Max injection pressure	32.8 MPa
# CT scans	27

Table 4.4: Experiment 4 - Overview

To reduce the leak-off of the injection fluid, experiment 4 and 5 attempt to reduce the permeability of the sample by adding solid additives to the injection fluid. The solid additives are meant to create an internal and/or external filter cake. For the first experiment in this series, quartz powder is added to the injection water. The axial, radial and backpressure is kept equal to previous experiments. The perforations are slightly enlarged from 1 to 1.5 mm to reduce the chance of clogged perforations.

Five injection cycles take place, the first three use the dual 500D syringe pump and the last two that require higher pressures use the 65D syringe pump. All injection cycles use an injection rate of 25 ml/min so the injection pressure can be directly related to the permeability and viscosity changes. Viscosity is only changed during the last injection cycle when Fluorinert is used instead of water. During the first injection cycle, only water is injected to get an idea of the initial permeability. A switch is then made to the mixing vessel containing 10 grams of quartz powder and 2.22 l of water. The mixing vessel is at equal pressure as the rest of the injection system, so no pressure shocks are created when switching. Water is injected in the bottom of the vessel and the quartz powder and water mixture exits at the top of the mixing vessel. At all times the mixing vessel is stirred to keep the quartz powder in suspension. Since no new quartz powder is added during the injection, the concentration slowly decreases over time. The mixing vessel can sustain pressures up to 15 MPa, once this pressure is reached the third injection cycle is started with once again only water. When the third injection cycle reaches 20 MPa, the injection is stopped and a switch is made to the 65D syringe pump. This pump injects the fourth cycle with only water and the fifth cycle with Fluorinert. This series of injection cycles is meant to first plug the formation during cycle 2, then create fractures or localized flow regions during cycle 3 and/or 4 that are visualized with the Fluorinert from cycle 5.

Data acquisition system The data acquisition recordings of experiment 4 can be found in figure 4.19. The different injection fluids are indicated by the colours. The injection pressure during the first injection cycle stabilises around 2.8 MPa. When a switch is made to the water with quartz powder mixture, its effect is directly noticeable in the injection pressure recordings. In previous discussions, we ignored the compressibility of the fluids and the expansion of the injection system. However, in this experiment a 2.22 l mixing vessel is connected to the injection system during injection cycle 1 and 2. Next to that, the pressure rises gradually as the quartz powder is injected, meaning that the effect of compressibility is noticeable for a prolonged time rather than just at the start and end of an injection cycle. Looking at the data acquisition records, a significant decrease in the pore fluid outflow rate can be observed as the injection pressure rises during the quartz powder injection. Once the pressure stabilises during injection cycle 3, so does the pore fluid outflow rate. The isothermal compressibility factor of the injection fluids as a function of pressure are described in section 2.2.2. By calculating the pressure change per time step, the volume of injection fluid that is compressed or expanded can be calculated with equation 4.3.

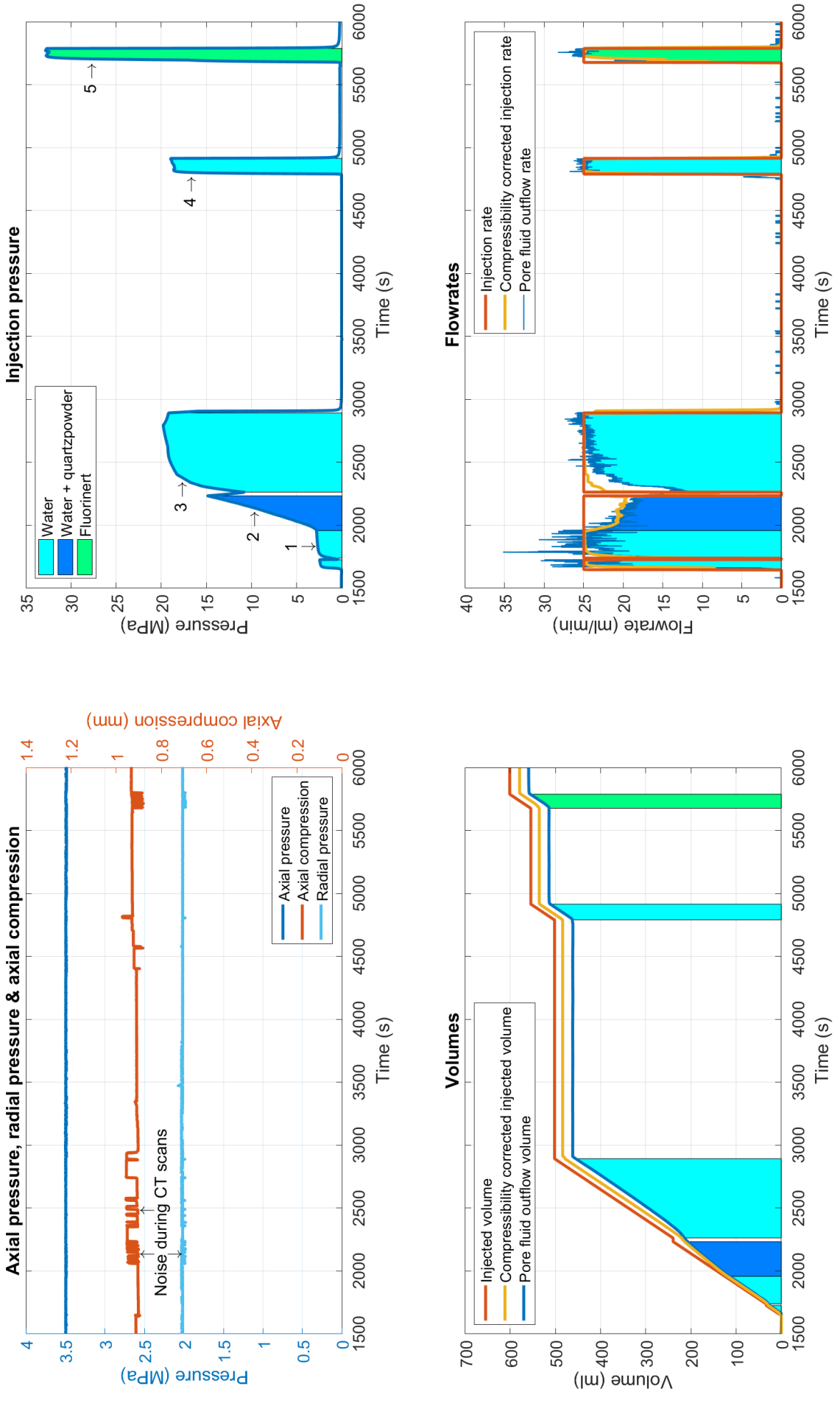

Figure 4.19: Experiment 4 - Data acquisition

$$\partial V = -\beta_T V \partial P \tag{4.3}$$

Where: β_V = Isothermal compressibility [1/Pa]
V = Volume [m^3]
P = Pressure [Pa]

By subtracting the compressed injection fluid from the injection rate per time step, or adding in case of expansion, a compressibility corrected injection rate can be calculated. Looking at the bottom right plot of figure 4.19, there is a good match between the compressibility corrected injection rate and the pore fluid outflow rate during injection cycles 1, 2, 4 and 5. As was previously mentioned, the effect is most noticeable when there is a gradual pressure change. At the end of injection cycle 2, the mixing vessel is disconnected from the injection system with the use of valves, meaning the compressed volume inside the vessel is lost in the sense that it is not injected as the pressure in the injection system decreases. This effect is visable in the volume plot at the end of injection cycle 2, when a difference is created in between the injected volume and the pore fluid outflow volume. The compressibility corrected injected volume is corrected for this effect. However, a mismatch between the compressibility corrected injection rate and the pore fluid outflow rate during the beginning of injection cycle 3 eventually leads to a mismatch between the compressibility corrected injection volume and the pore fluid outflow volume. The reason for this low pore fluid outflow rate at the beginning of injection cycle 3 is unknown and eventually does restore to the 25 ml/min flowrate. At this point it is suspected that air entered the injection system when changing from injection cycle 2 to 3, which is compressed at the start of injection cycle 3. The compressibility corrected injection rate only corrects for the compressibility of water and not air, leading to a mismatch. There is a pressure difference of a factor 1.7 between injection cycle 4 and 5, which is in the same order of magnitude as the viscosity difference between the fluids of a factor 1.6.

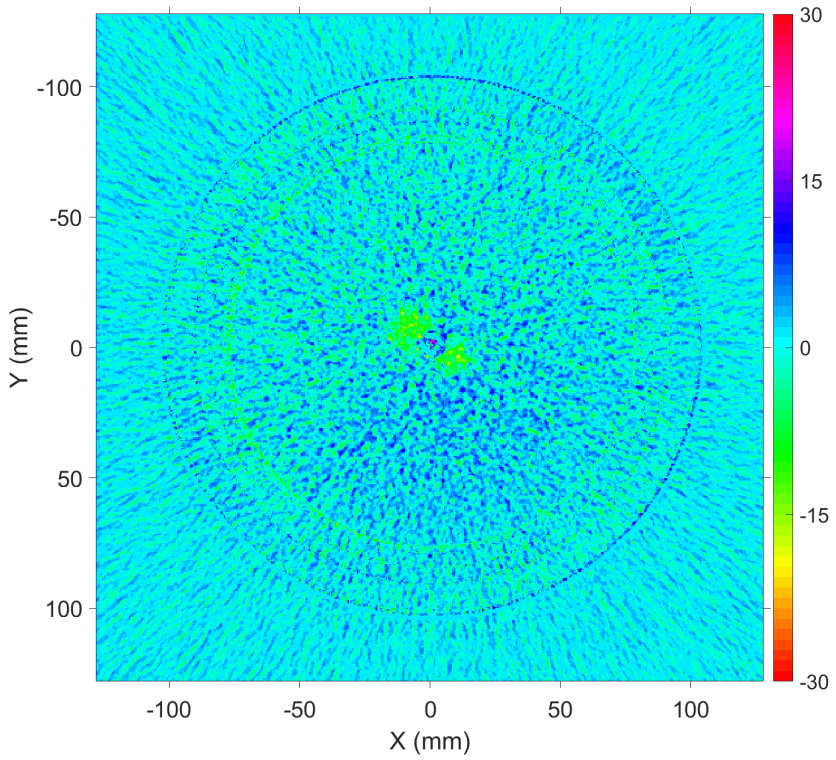

Figure 4.20: Experiment 4 - Image difference CT scan 1 & 2 at perforation height [Grayscale]

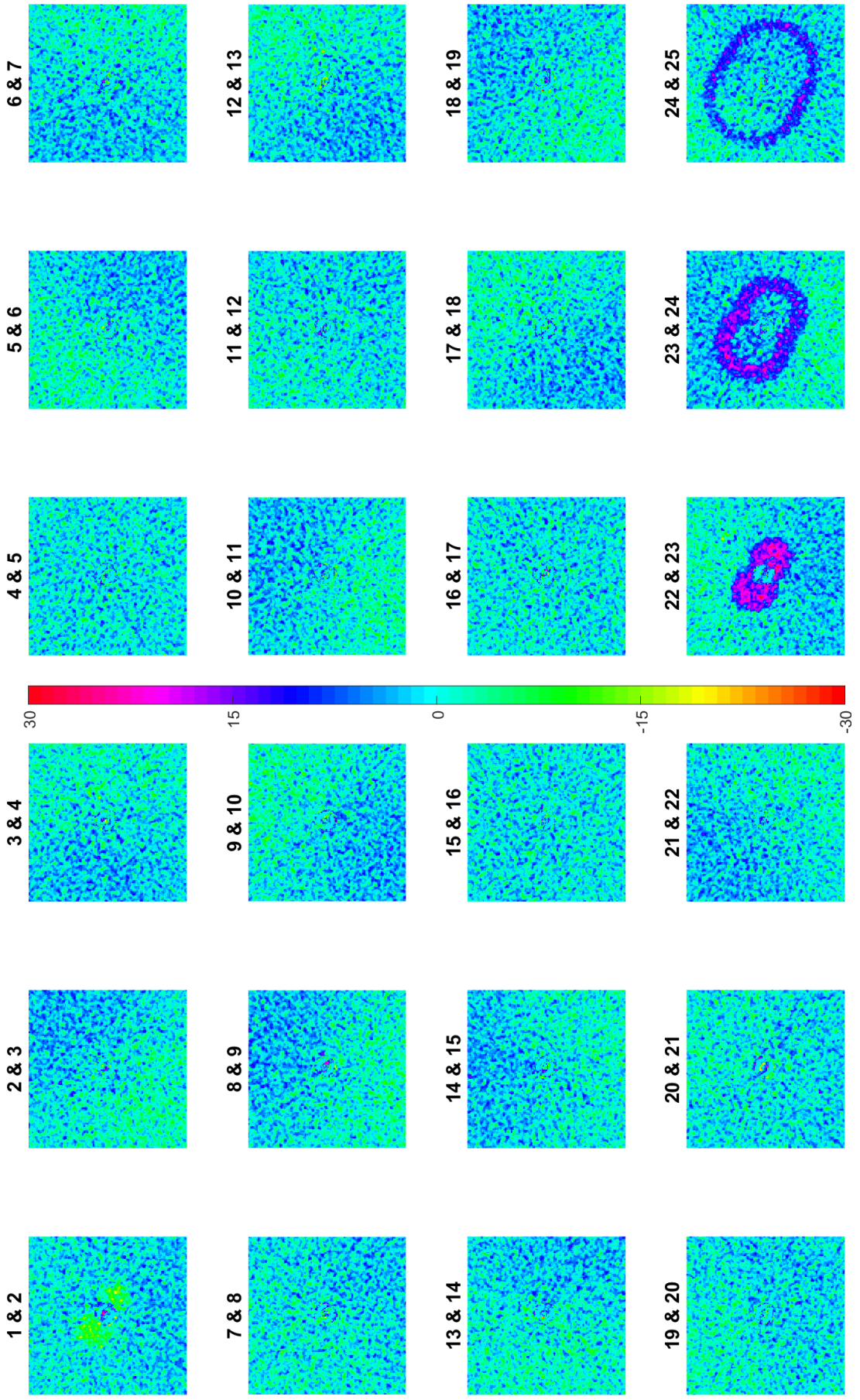

Figure 4.21: Experiment 4 - Image difference scans 1 to 25 at perforation height [Grayscale]

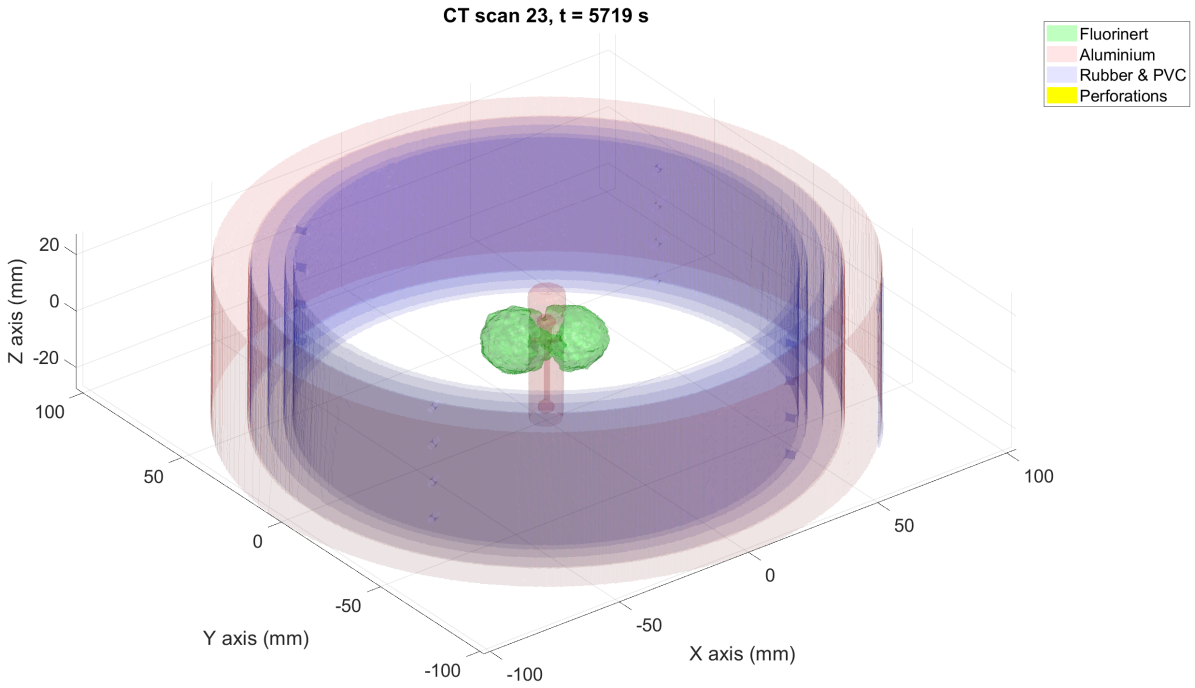

Figure 4.22: Experiment 4 - Fluorinert scan 23 - 3D view

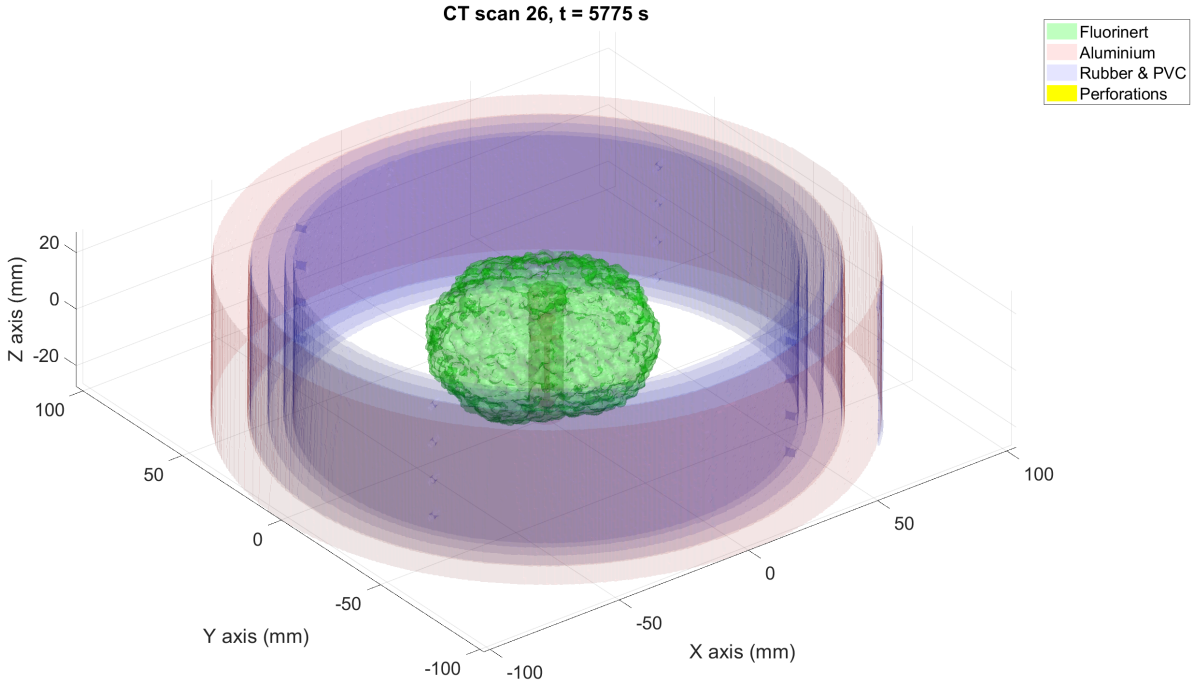

Figure 4.23: Experiment 4 - Fluorinert scan 26 - 3D view

CT scanner There is a notable density difference near the perforations between the first CT scan and the subsequent ones. The low-density region is located exactly in front of both perforations, as can be seen in figure 4.20. In this figure a decrease iin grayscale means an decrease in density. The first scan is made before injection has started, which means at this point the rubber pin that serves as a sand filter is still blocking the perforations. When injection starts, the rubber ball is displaced upward into the injection tube, unplugging the perforations. It seems that due to the pressure difference between the injection tube and the sample, a

pressure surge was created that sucked nearby sand particles into the injection tube. The low-density region stays in place throughout the experiment and does not increase or decrease in size.

The quartz powder as a component of the image density, has not been detected in the CT scans. It should first be detectable in the CT scans at the height of the perforations, but as can be seen in figure 4.21, no density changes can be observed around the injection tube until Fluorinert is injected in the last 5 scans. Some light noise in the CT scans and small changes in the injection tube itself can be observed, but no irregular shapes have been observed in front of the perforations. It is possible that the quartz powder has not infiltrated the sample, but instead accumulated in the injection system over time. The Fluorinert infiltrates the low-density region first before spreading in a ellipsoid shape as can be seen in figure 4.22 and 4.23.

4.5. Experiment 5 - Bone meal

Injection fluids	Water
	Water + quartz powder
	Fluorinert FC-770
Injection pumps	Dual 500D syringe pump
	65D Syringe pump
Injection system	Two 1.5 mm diameter perforations
Sand filter	Rubber pin
Axial pressure	3.5 MPa
Radial pressure	2 MPa
Backpressure	0.2 MPa
Max flowrate	25 ml/min
Max injection pressure	41.2 MPa
# CT scans	26

Table 4.5: Experiment 5 - Overview

Since no quartz powder could be detected in the CT scans, it is questionable if the solid particles have actually made their way into the sample. It is possible that the majority of the quartz powder has precipitated in the injection system before reaching the perforations. The relatively low flow rate and high density difference between the injection water and the quartz could be responsible for the precipitation. To decrease the density difference between the water and the solid particles, a switch has been made to cow bone meal, which has a bulk density of 0.88 to 0.96 g/cm3 that is much closer to the density of water. The exact same injection system, external pressures, flowrates and pumps are used as in experiment 4. The concentration of the solid particles remains the same at 10 grams in the 2.22 l mixing vessel. Five injection cycles are performed, the first three the same as in experiment 4. The first cycle starts with water injection after which a switch is made to the water with bone meal mixture to a maximum of 15 MPa. The third cycle injects only water up to a maximum of 20 MPa. Finally two Fluorinert cycles take place, the first is shut-down due to the pressure exceeding the maximum pressure of the injection system. The second Fluorinert injection cycle is pressure controlled at a constant pressure of 41.3 MPa.

Data acquisition system The results of the data acquisition system can be found in figure 4.24. The pressure during the first injection cycle tops at 3 MPa, which shows that the sample has a very similar permeability as in experiment 4 where it topped at 2.8 MPa. The pressure during injection cycle 2 rises to 15 MPa in 272 seconds, which is the same as when quartz powder was used in experiment 4, which took 275 seconds. The compressibility corrected injection rate is once again added and shows a good match during injection cycle 2, 4 and 5. A similar mismatch between the pore fluid outflow rate and the compressibility corrected injection rate is observed with injection cyle 3, following the injection of fines. The pore fluid outflow rate restores to 25 ml/min at the end of injection cycle 4. The reason for this behaviour is still unclear, the compressibility of the water is not nearly large enough to explain this effect. The same experimental procedure is performed as in experiment 4. As described in the previous section, a possible explanation is air in the injection system resulting from the switch from injection systems once the mixing vessel is disconnected. The injection pressures during injection cycle 4 and 5 are higher than the Fluorinert injection during experiment 4. This indicates that the bone meal has either more successfully plugged the sample, or that the injection system

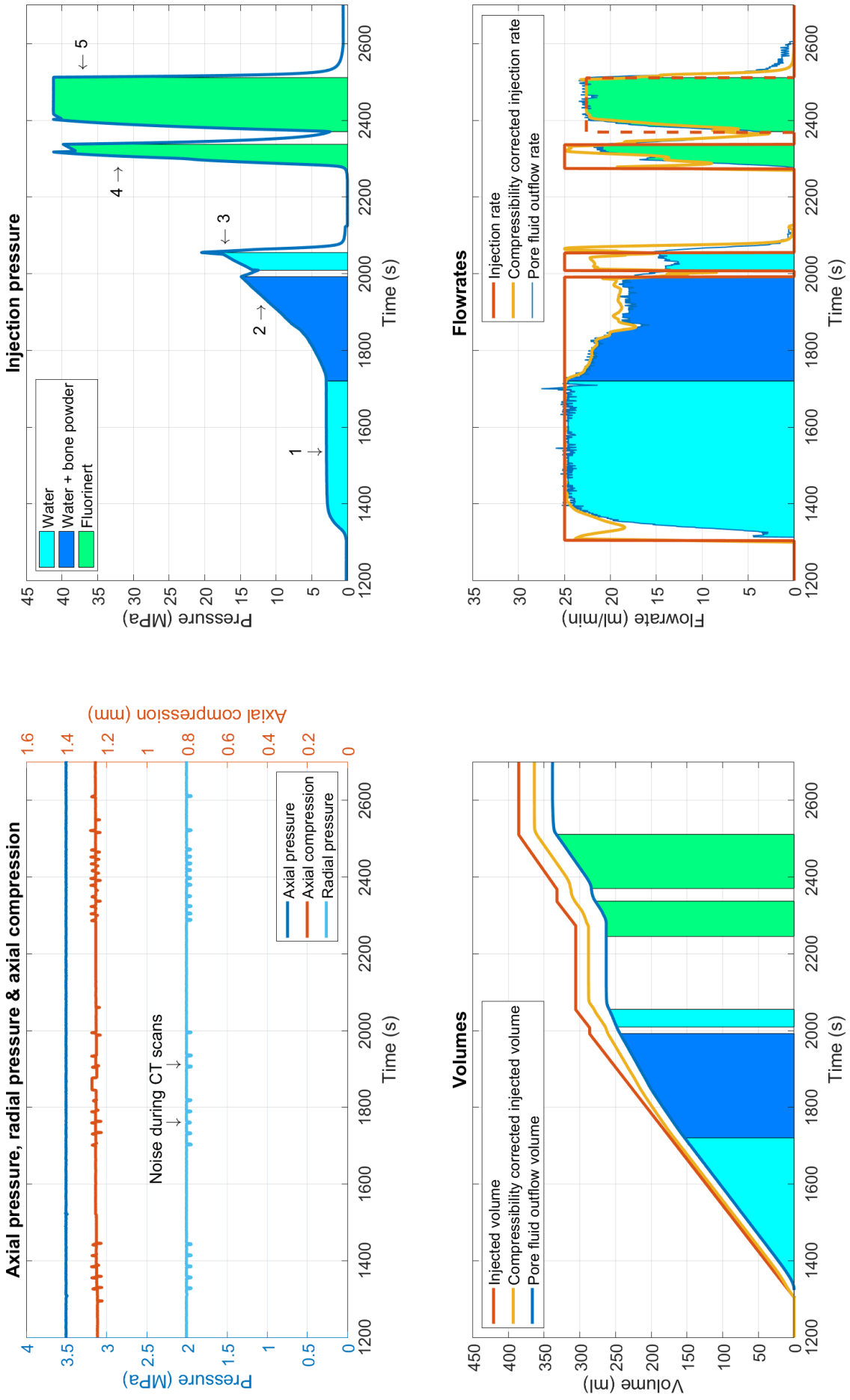

Figure 4.24: Experiment 5 - Data acquisition

has been clogged. There are no signs of fracturing when looking at the injection pressure and flowrate plots except possibly during injection cycle 4 where the pressure slightly drops and the flowrate increases. This could also be due to an injection system clog coming loose.

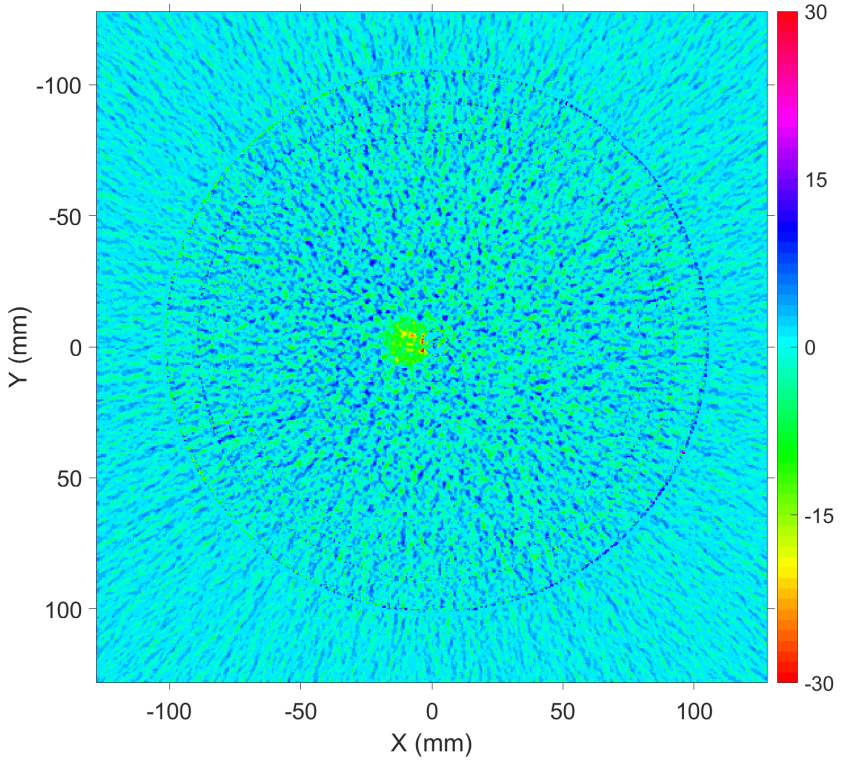

Figure 4.25: Experiment 5 - Image difference CT scan 1 & 2 at perforation height [Grayscale]

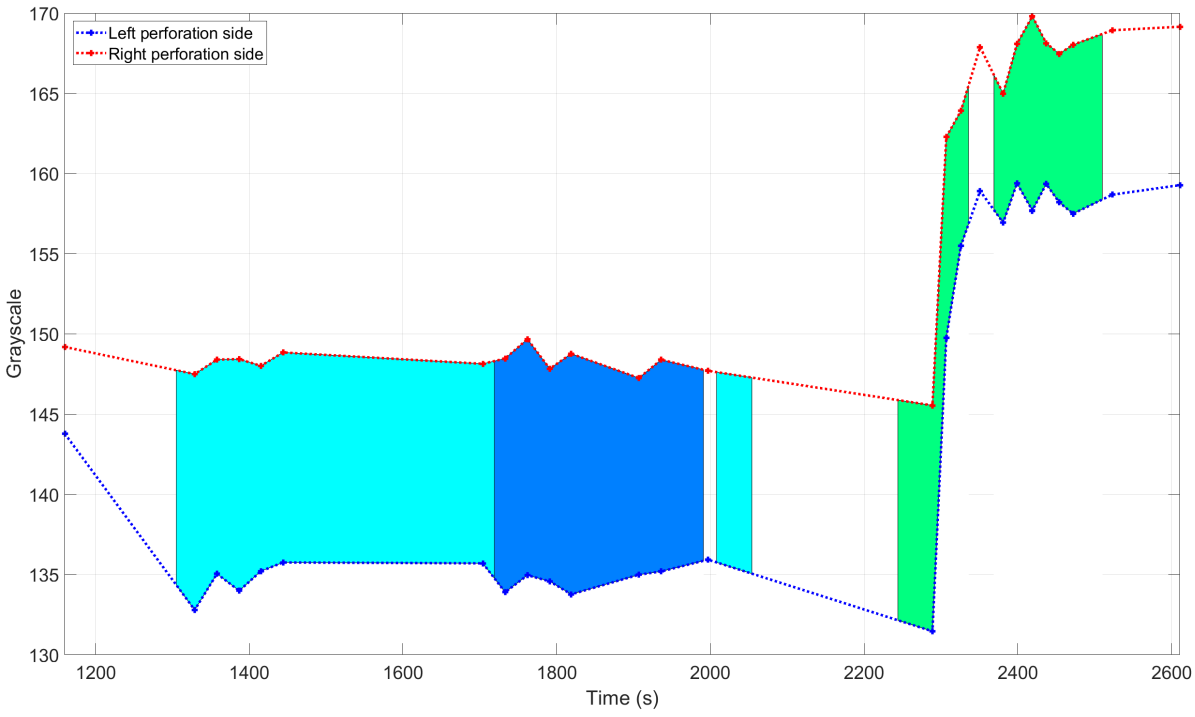

Figure 4.26: Experiment 5 - Average grayscale near perforations

CT scanner Just as in experiment 4, a low-density region is created in-between the first and second CT scan. This time however, only one perforation side is affected as can be seen in figure 4.25. This indicates that the pressure shock that was created by the pressure difference between the sample and the injection tube only occurred at the left perforation and that the right perforation was still (partially) closed at the time. Even a small cavity can be observed on the left side, indicated by the dark blue colour. This cavity is filled back up over time, this is most noticeable in the image differences between scan 2 & 3 and 6 & 7 in figure 4.27.

The low density difference between the water and the bone meal is an advantage when it comes to injecting the particles, but is a disadvantage when it comes to detecting them on the CT scanner. If particles plug the pores and fill the pore space with bone meal instead of water, the decrease in density is most likely too low to detect in grayscale variation. A small decrease in density in front of the perforations can be observed during the third injection cycle, in-between scan 14 and 15. If this is related to the bone meal is unclear. To help visualise the grayscale of the scans over time, figure 4.26 can be used. It shows the average grayscale of 6 by 6 by 5 pixels in the X, Y and Z plane in front of the perforations at both sides. As was previously observed, the grayscale in front of the left perforation decreases in between scan 1 and 2. No noticeable grayscale changes can be seen throughout injection cycles 1 to 3. Once the Fluorinert is injected, the grayscale rises significantly with a small delay. The Fluorinert reconstructions of figure 4.28 and 4.29 show a flow path preference for the left perforation side.

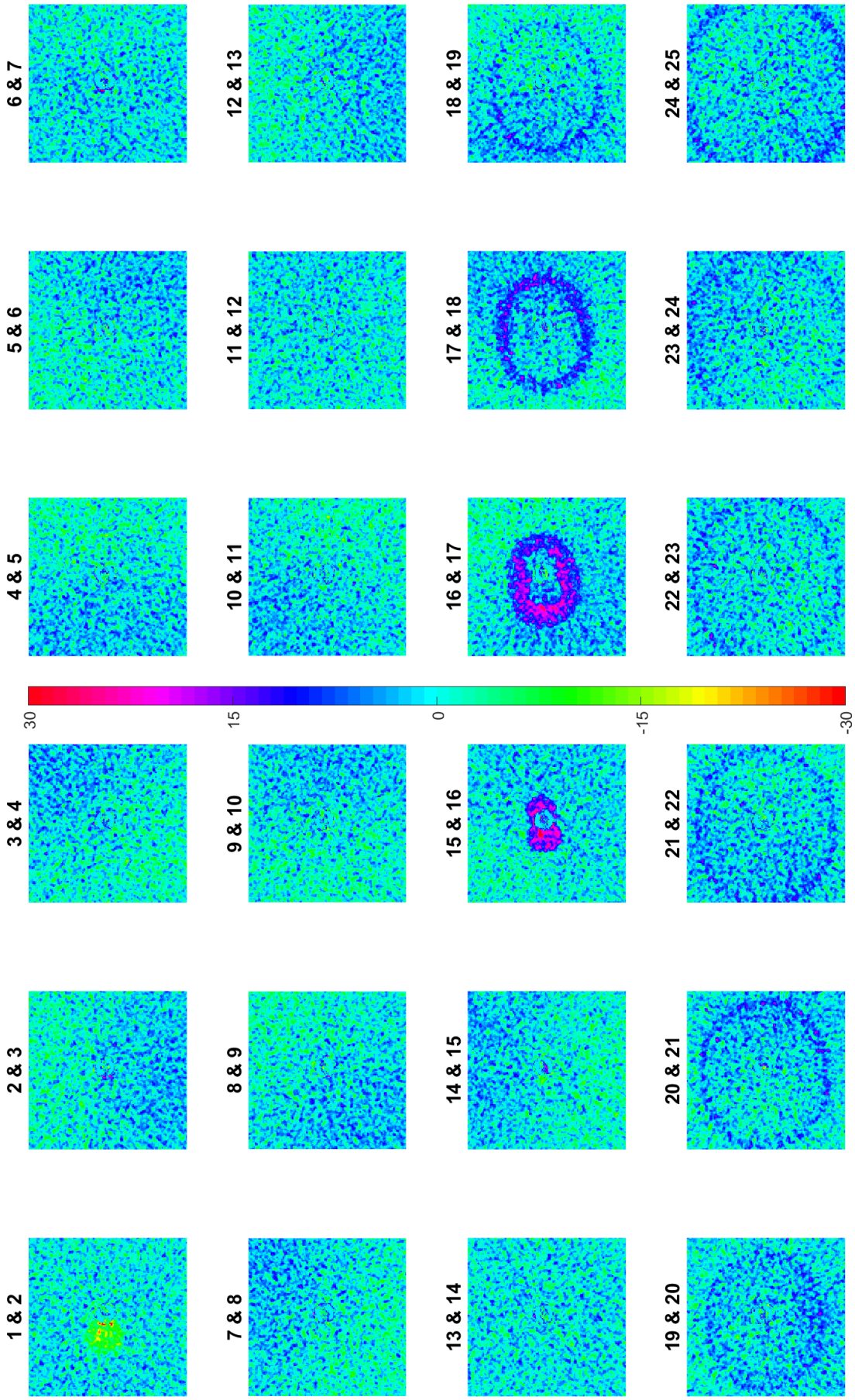

Figure 4.27: Experiment 5 - Image difference scans 1 to 25 at perforation height [Grayscale]

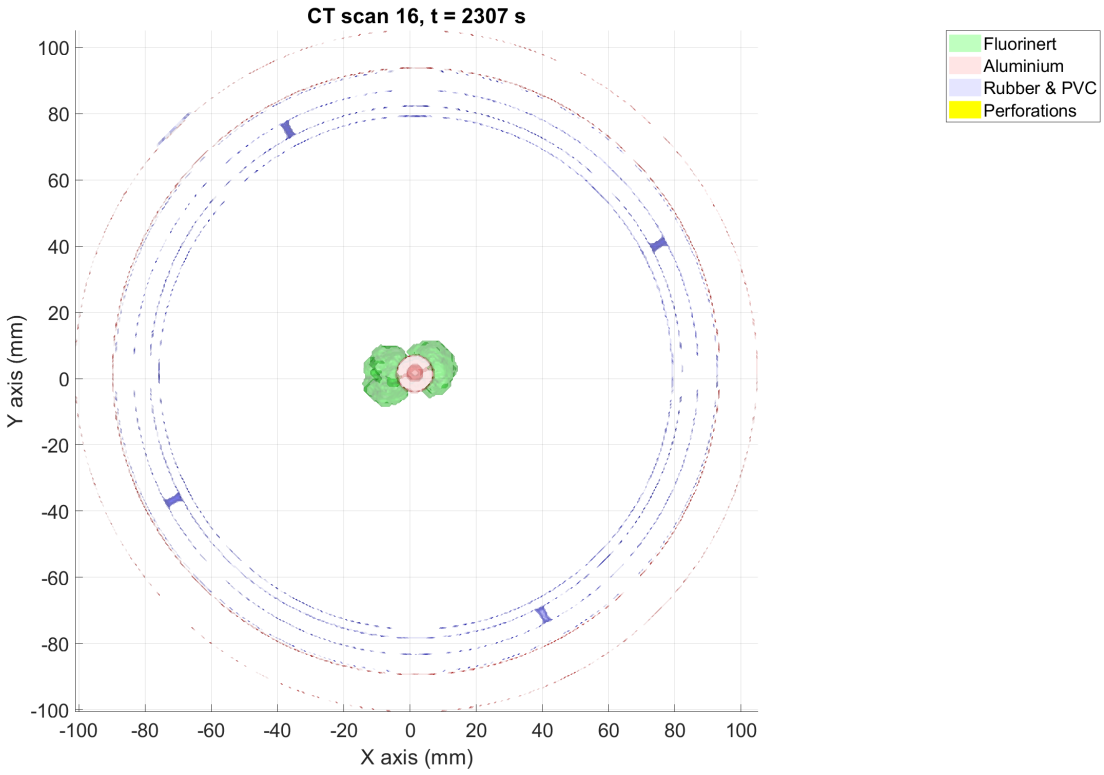

Figure 4.28: Experiment 5 - Fluorinert scan 16 - Top view

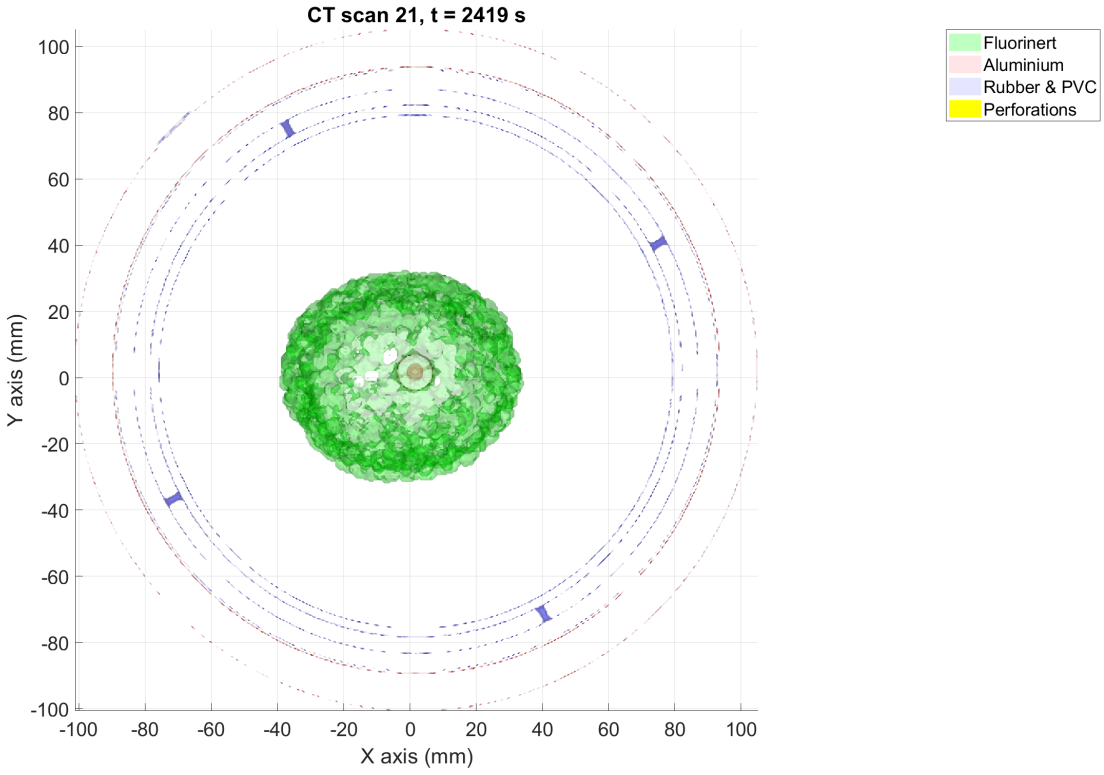

Figure 4.29: Experiment 5 - Fluorinert scan 21 - Top view

4.6. Experiment 6 - Internal pressure sensors

Injection fluids	Water
	Fluorinert FC-770
Injection pumps	Air stroke pump + intensifier
	Dual 500D syringe pump
Injection system	Two 2.5 mm diameter perforations
Sand filter	5 µm external sand screen
Axial pressure	1 MPa
Radial pressure	1 MPa
Backpressure	0.2 MPa
Max flowrate	2040 ml/min
Max injection pressure	6.5 MPa
# CT scans	31

Table 4.6: Experiment 6 - Overview

For the last experiment in this series, several parameters were changed. The largest change is the use of a different sample, using 3 grain sizes instead of 1. The combination of fine to very fine sand with a clay will decrease the permeability and mimic field conditions more closely. Next to that, the fines could migrate during the injection cycles, creating higher and lower permeability regions. The sample properties are described in section 2.2.1. The second change is the use of a larger injection tube with an inner diameter of 3 mm instead of 2. In addition, the perforations are enlarged to 2.5 mm. This is to minimalize the pressure drop in the injection tube and perforations, especially at higher flowrates. The third change is the use of different external pressures. In the previous experiments, the axial pressure was kept at 3.5 MPa and radial pressure at 2 MPa. By decreasing the external pressure, the grains can mobilize more easily to create fractures, channels or low permeability regions. The backpressure is kept the same as previous experiments at 0.2 MPa. An external sand screen is used with a small mesh to ensure no clay particles can pass.

A major improvement of the data acquisition system is the addition of internal pressure sensors. Three sensors were added for this experiment, which were located 5, 10 and 15 mm in front of the perforations. These sensors will help determining the pressure drop within the sample. This allows us to have four injection pressure measurement points in total.

For the injection, mainly the air stroke pump in combination with the intensifier is used. The pump can handle the high injection rates that are desired during this experiment. As a secondary injection system, the dual 500D syringe pump is used for the low injection rates because of its accuracy. There are 18 injection cycles of which the first 16 are with degasified water. The injection cycles are divided in 3 phases. The first phase injects water at 5 different low injection rates, to get a measurement of the injectivity of the sample. These injection cycles last roughly 20 seconds and a scan is made during each of them. The second phase consists of a series of high injection rates, also with water. Mainly an injection sequence of 1200 ml/min and 2040 ml/min for 10 seconds each is repeated several times. The purpose of this phase is to fracture the sample. For the last phase, Fluorinert is injected to visualize flow paths that possibly have been created.

Data acquisition system The results of injection cycles 1 to 11 can be found in figure 4.30 and cycles 12 to 18 in figure 4.31. To keep an overview of all the data and the of injection cycles, the results are summed up in table 4.7. The first thing that should be noticed is the relatively low injection pressures. The highest injection pressure during this experiment was 6.5 MPa. This is notably lower than previous experiments even though the flowrate is higher at most times. This can be attributed to the lower external pressures, the wider injection tube & perforations and no clogging due to the small filter mesh. The highest injection pressure occurs during injection cycle 6, where 1200ml/min is injected. Looking at table 4.7, it can be observed that the injectivity increases after the pressure peak of injection cycle 6. To visualise this even better, figure 4.32 plots the injection rates of cycles 1 to 6 and cycles 7 to 16 against their injection pressures. After injection cycle 6, the injectivity remains stable with pressure responses of 1.4, 1.6 and 1.5 MPa during the 2040 ml/min cycles.

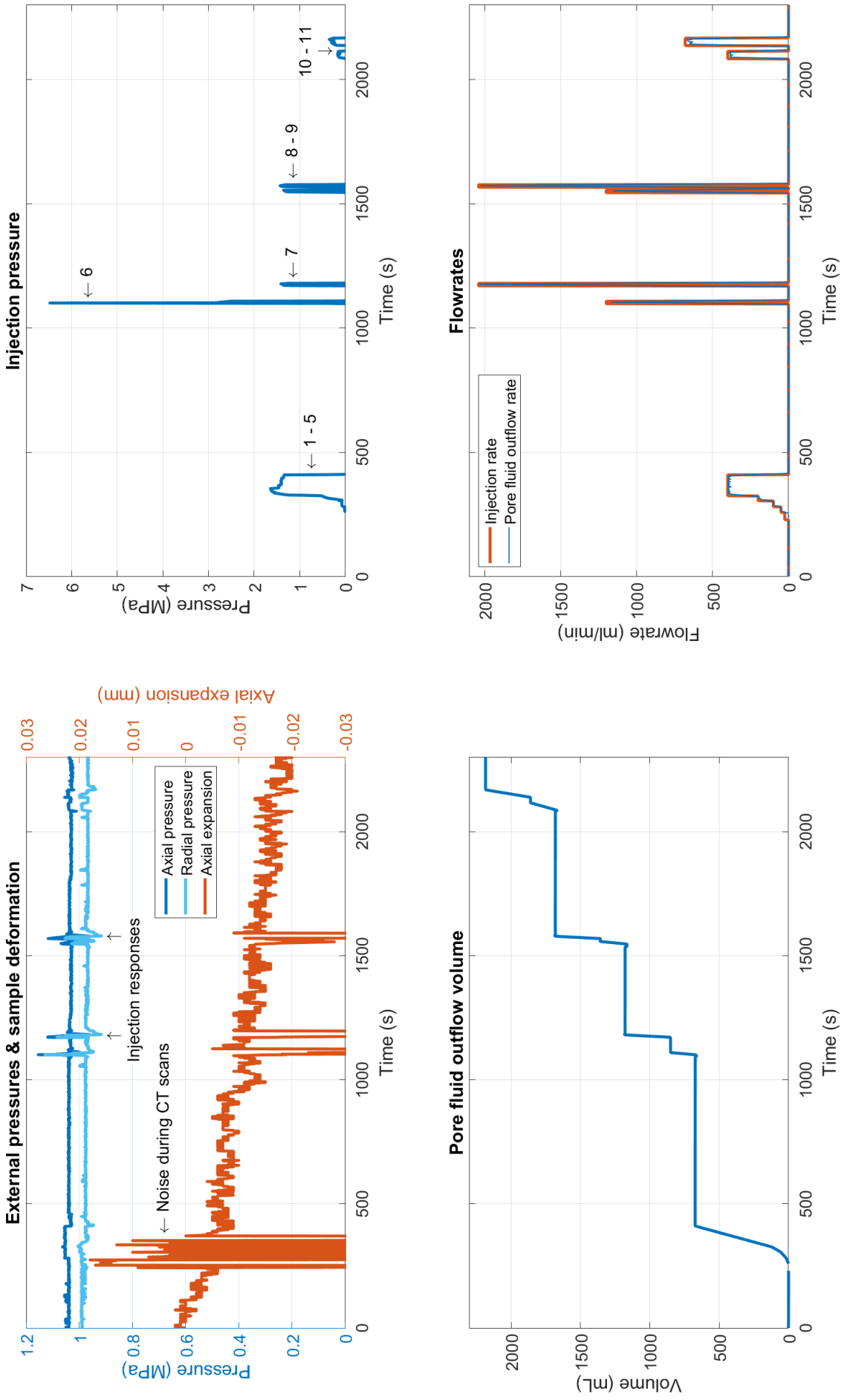

Figure 4.30: Experiment 6 - Data acquisition - Overview 0 - 2300 s

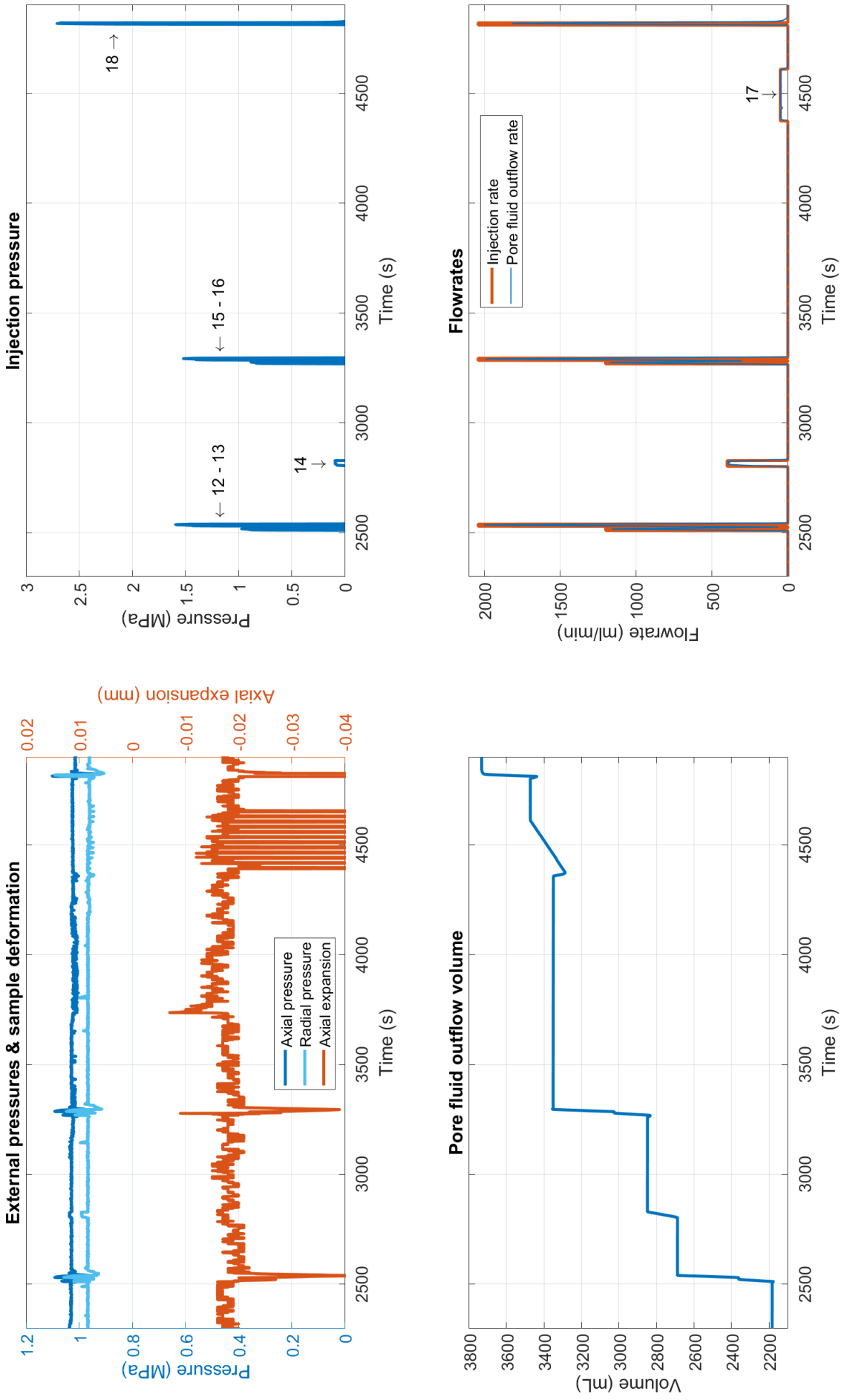

Figure 4.31: Experiment 6 - Data acquisition - Overview 2300 - 4900 s

Cycle	Injection fluid	Time	Injection rate	Injection pressure	Outflow volume	CT scans
#	-	s	ml/min	MPa	ml	#
1	Water	28	25	0	0	2
2	Water	22	50	0.015	17.2	3
3	Water	23	100	0.080	36.1	4
4	Water	19	200	0.503	58.4	5
5	Water	84	400	1.641	546	6 - 7
6	Water	10	1200	6.482	151.8	8 - 9
7	Water	10	2040	1.415	295.2	10 - 11
8	Water	10	1200	1.355	152.2	-
9	Water	10	2040	1.431	282.6	12 - 13
10	Water	30	400	0.168	174.9	-
11	Water	30	680	0.352	311.9	-
12	Water	10	1200	0.973	150.7	-
13	Water	10	2040	1.593	292.4	-
14	Water	26	400	0.096	151.5	-
15	Water	10	1200	0.885	170.4	14 - 15
16	Water	10	2040	1.521	266	-
17	Fluorinert FC-770	235	50	0	182.7	16 - 28
18	Fluorinert FC-770	10	2040	2.710	221	29 - 31

Table 4.7: Experiment 6 - Data acquisition overview

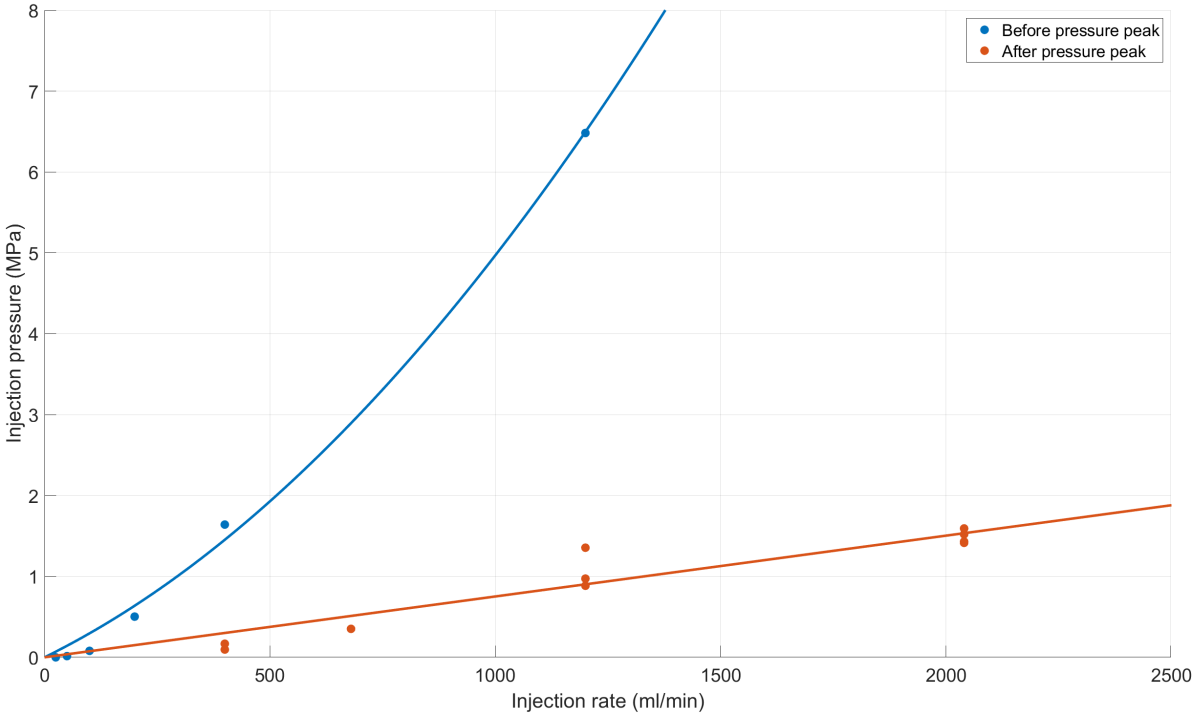

Figure 4.32: Experiment 6 - Injection pressure - rate correlation

The LVDT measuring the axial deformation shows that the sample is steadily compressing over time during the first 2200 seconds. It stays stable after being compressed about 0.02 mm. There is no direct correlation visible between the injection cycles and the sample deformation other than noise when the CT cell moves through the CT scanner. This makes us conclude that the sample was not yet in full equilibrium at the start of the experiment. The compression of 0.02 mm equals to a volume of 0.36 ml, which is little enough to not be visible on the mass balance. Also notable is the pressure response of the axial and radial pressure system to the injection cycles. The pumps are set to a constant pressure of 1 MPa, but injection fluids exert a high enough pressure on the matrix that the pumps require time to get to equilibrium. The injection pressure ratio between the high flowrate water and Fluorinert injection is of a factor 1.7 to 1.9. Slightly higher than the viscosity difference between the water and Fluorinert.

Internal pressure sensors The results of the internal pressure sensors can be found in figure 4.33. For an overview of the pressure differences between the sensors, see table 4.8. The sensors record relatively high pressures for their respective injection rates during cycles 1 to 5 compared to injection cycles 7 to 16. Injection cycle 6 gives a slightly higher injection pressure than the other 1200 ml/min injection rate cycles, but not as significant of a difference as the injection system pressures. The pressure peak of 6.5 MPa in the injection system only lasted 1 second, after which it dropped back to 2.8 MPa. It is possible that this peak was not recorded in the internal pressure sensors, which is not synchronized with the data acquisition system. The pressure difference between the 15 mm and 5 mm sensor of injection cycle 6 at 0.033 MPa is similar to other 1200 ml/min cycles that have a pressure difference of 0.034, 0.031 and 0.034 MPa. This helps conclude that the sample in between these sensors does not significantly change in its permeability. There is a difference for the 10 and 5 mm sensor however, which is at 0.017 MPa for injection cycle 6 and at 0.011, 0.008 and 0.012 MPa for other 1200 ml/min cycles. In the next paragraph, we will have a closer look at the CT scans before and after the pressure peak of injection cycle 6.

Cycle	dP 10 mm - 5 mm	dP 15 mm - 5 mm
#	MPa	MPa
1	-0.009	-0.002
2	-0.007	0.002
3	0.002	0.007
4	0.012	0.015
5	0.010	0.041
6	0.017	0.033
7	0.026	0.060
8	0.011	0.034
9	0.019	0.059
10	0.005	0.012
11	0.007	0.020
12	0.008	0.031
13	0.021	0.059
14	0	0.009
15	0.012	0.034
16	0.016	0.055
17	-0.002	0.002
18	-0.002	0.002

Table 4.8: Experiment 6 - Internal sensors pressure differences

CT scans Figure 4.35 visualises the image difference over time at the height of the perforations for the first 16 scans. For information as to which scan belongs to which injection cycle, see table 4.7. The scans contain a large amount of noise, described in section 3, but the noise can be distinguished from larger region density changes. In between scans 1 & 2 and 5 & 6, some moving grains in front of the perforations can be observed. The image difference between scan 4 and 5 shows a slightly lower density region being created on the right side of the injection tube. Scan 8 is the start of high flowrate injection cycle 6. A large region around the injection tube decreases in density during this injection cycle. For a clearer picture, see the left image of figure

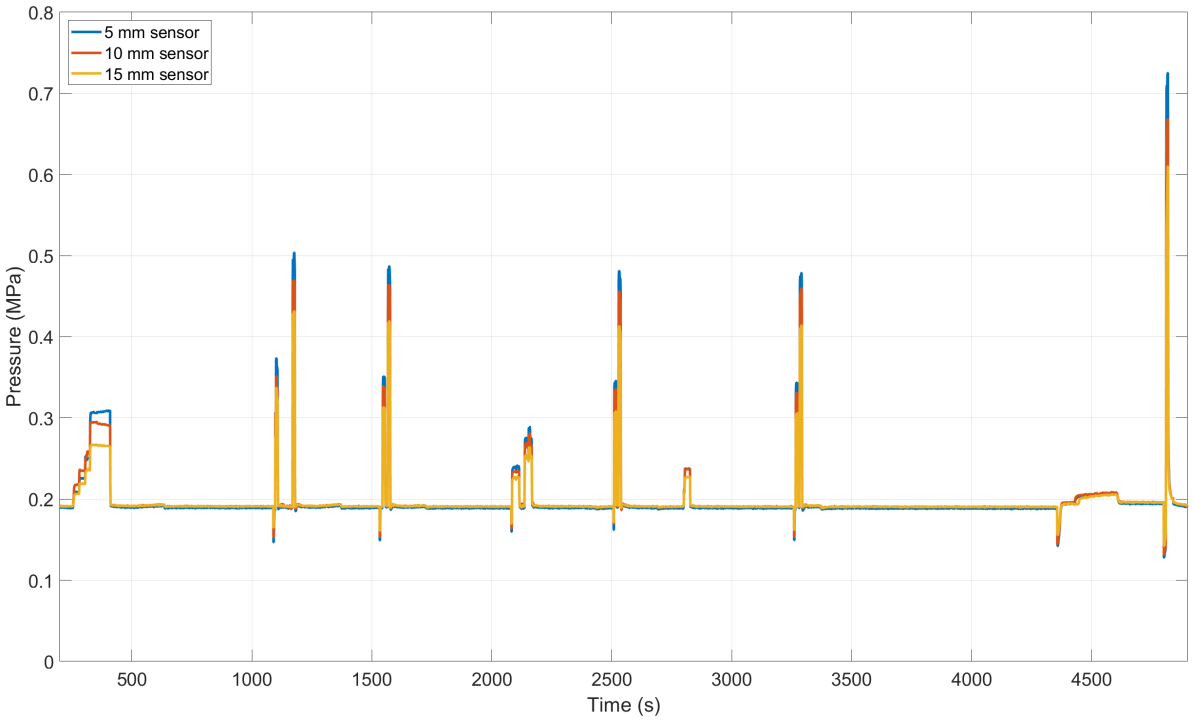

Figure 4.33: Experiment 6 - Internal pressure sensors results

4.34. The injectivity increase after injection cycle 6 can be explained with the creation of this lower density region. Clay in this region has most likely migrated to the surrounding area. Note that the higher density region at the top right corner of the image difference of scan 7 and 8, is a zebra artefact and not necessarily the main accumulation region for the migrated clays. More information on this type of noise is described in section 3.

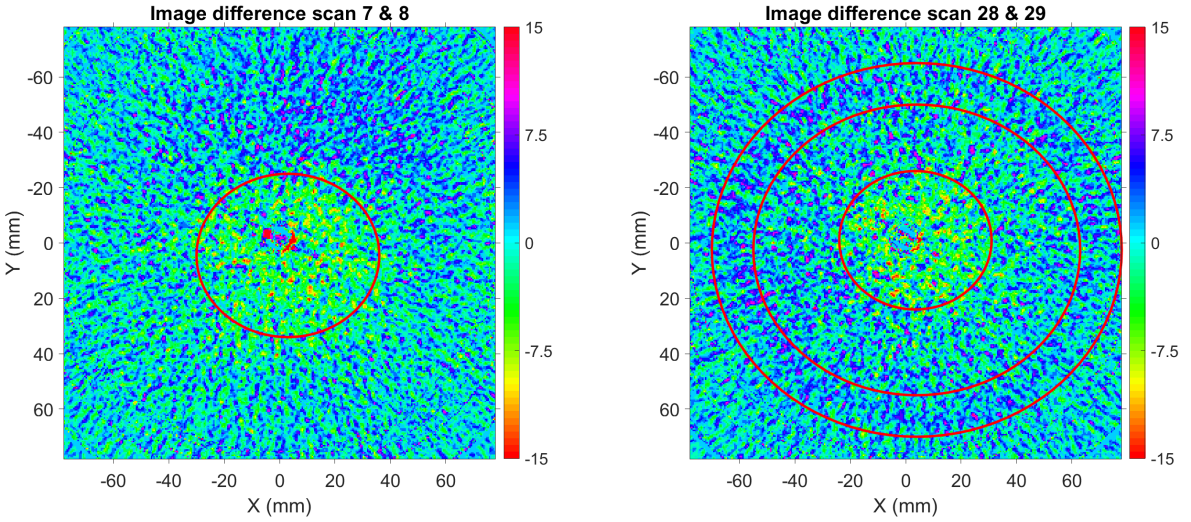

Figure 4.34: Experiment 6 - Formation of low density regions

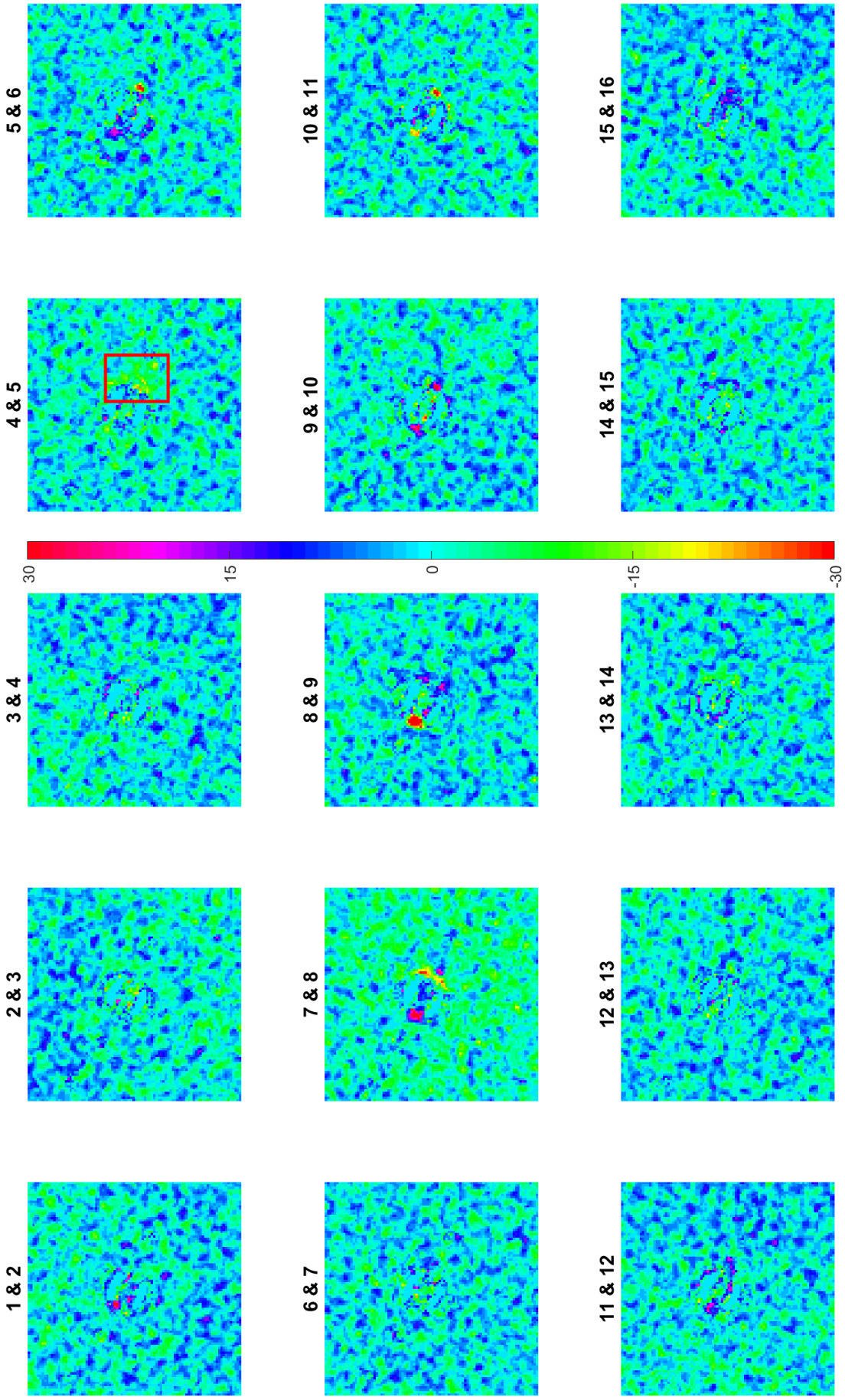

Figure 4.35: Experiment 6 - Image difference at height of perforations - Overview scan 1 - 16 [Grayscale]

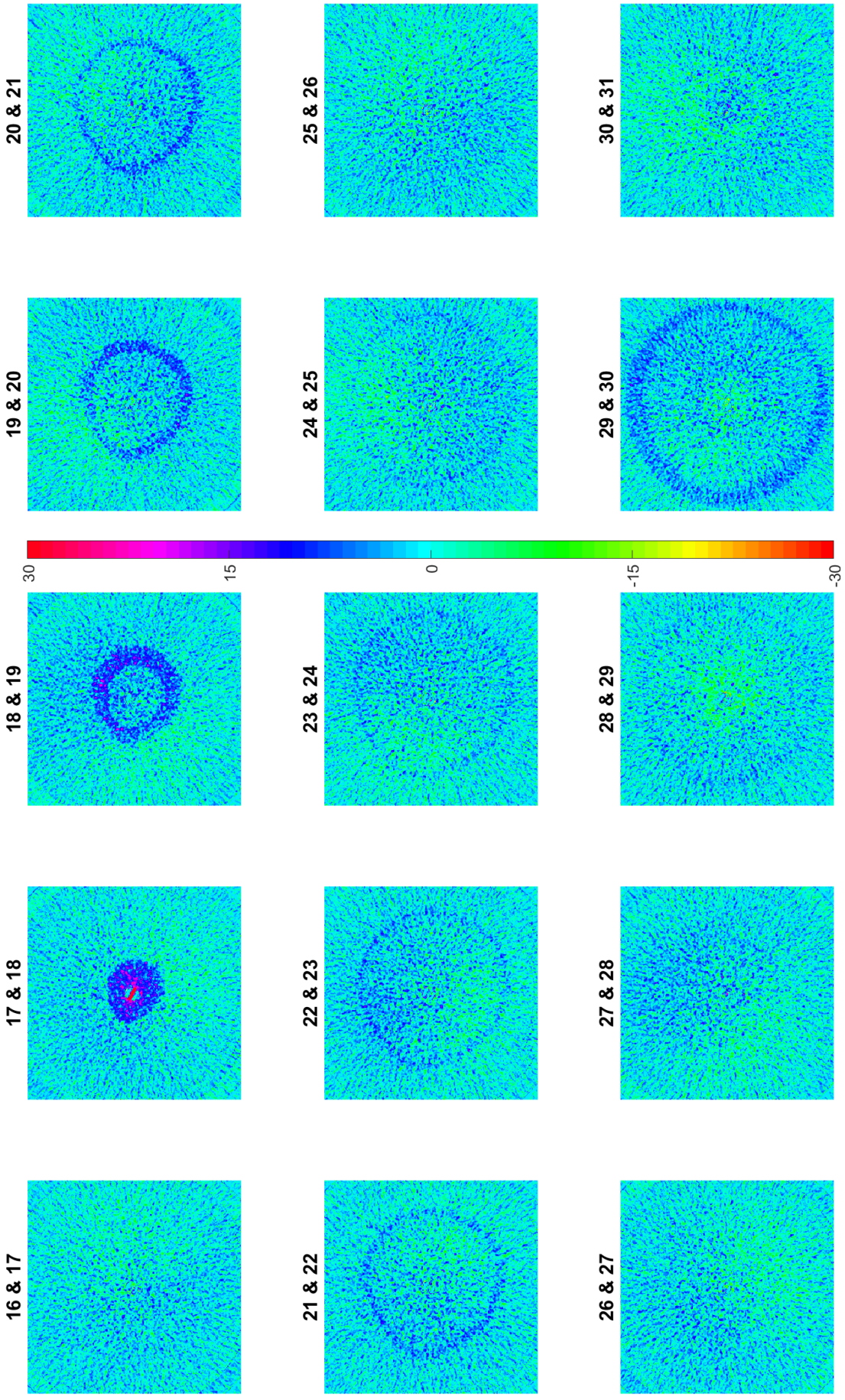

Figure 4.36: Experiment 6 - Image difference at height of perforations - Overview scan 16 - 31 [Grayscale]

Figure 4.36 visualises the image difference of scans 16 to 31, which is when Fluorinert is being injected. The helical artefacts that were previously mentioned are clearly visible in these scans. The seemingly low and high density region spirals through the sample, depending on where the CT scanner detector is at the moment of the scans. However, the formation of a low-density region around the injection tube as in scans 28 to 29, is not noise. This image is enlarged in figure 4.34 and visualises the density difference between the first and second scan during the high flow rate Fluorinert injection. The outer ring shows the expansion of the Fluorinert infiltration zone. The injection pressure for this cycle was higher than previous cycles due to the higher viscosity Fluorinert. This pressure has caused another migration of grains.

Due to the high amount of helical artefacts in this set of CT scans, the 3D reconstructions of the Fluorinert are noisy. Figure 4.37 visualises the internal pressure sensors, held together with glue to the injection tube. Figure 4.38 and 4.39 show that the right perforation side has a flow preference. This agrees with the image difference of figure 4.34 that shows that the low-density region is larger on the right side of the injection tube. This is also the side where only one pressure sensor is located, thus sample disturbance can also play a role. During the high flowrate Fluorinert injection cycle, the entire sample within the scanned region is saturated with Fluorinert.

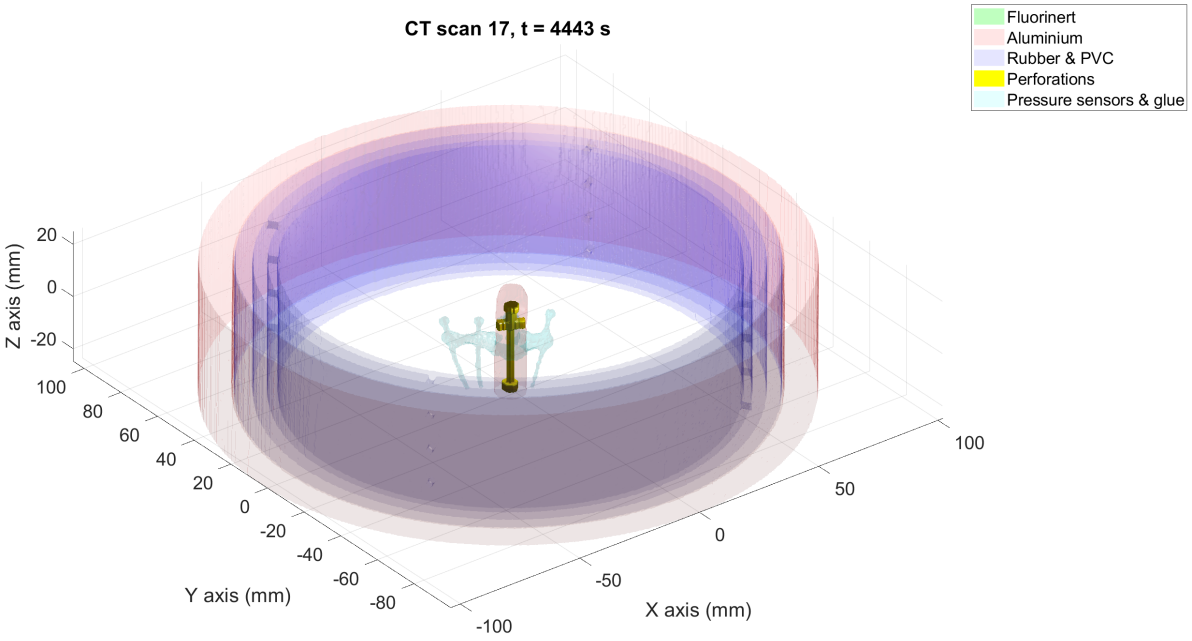

Figure 4.37: Experiment 6 - Internal sensors scan 17 - 3D view

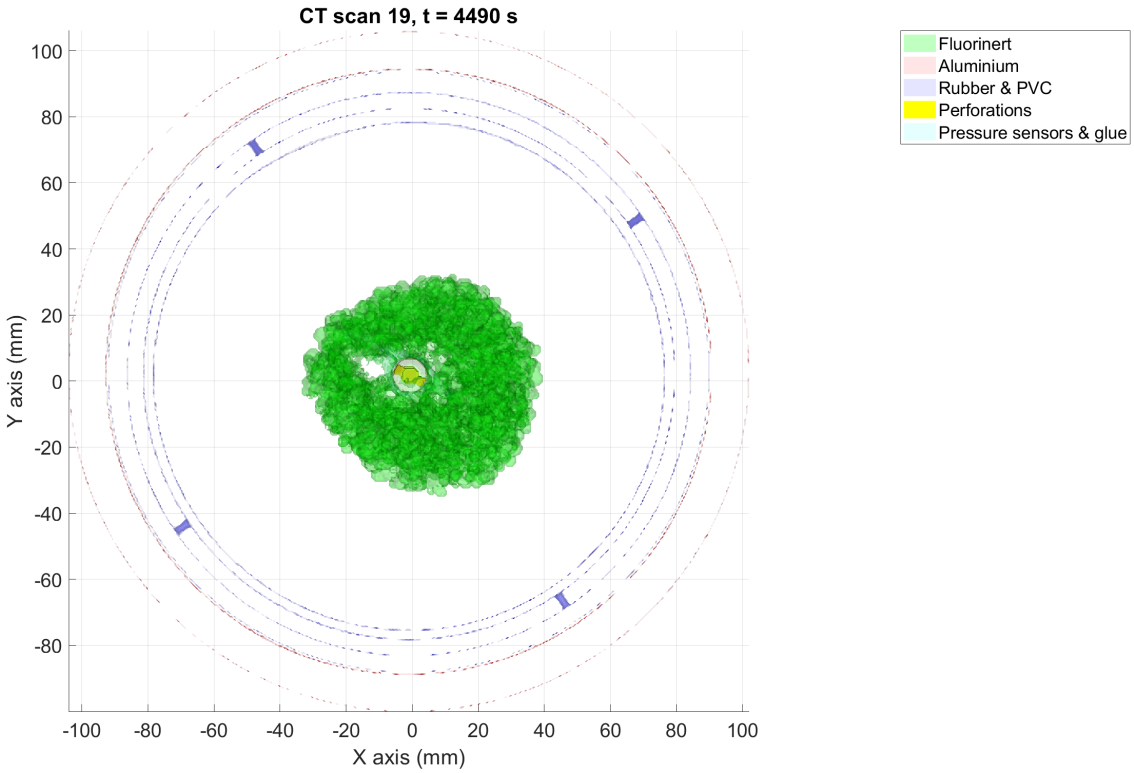

Figure 4.38: Experiment 6 - Fluorinert scan 19 - Top view

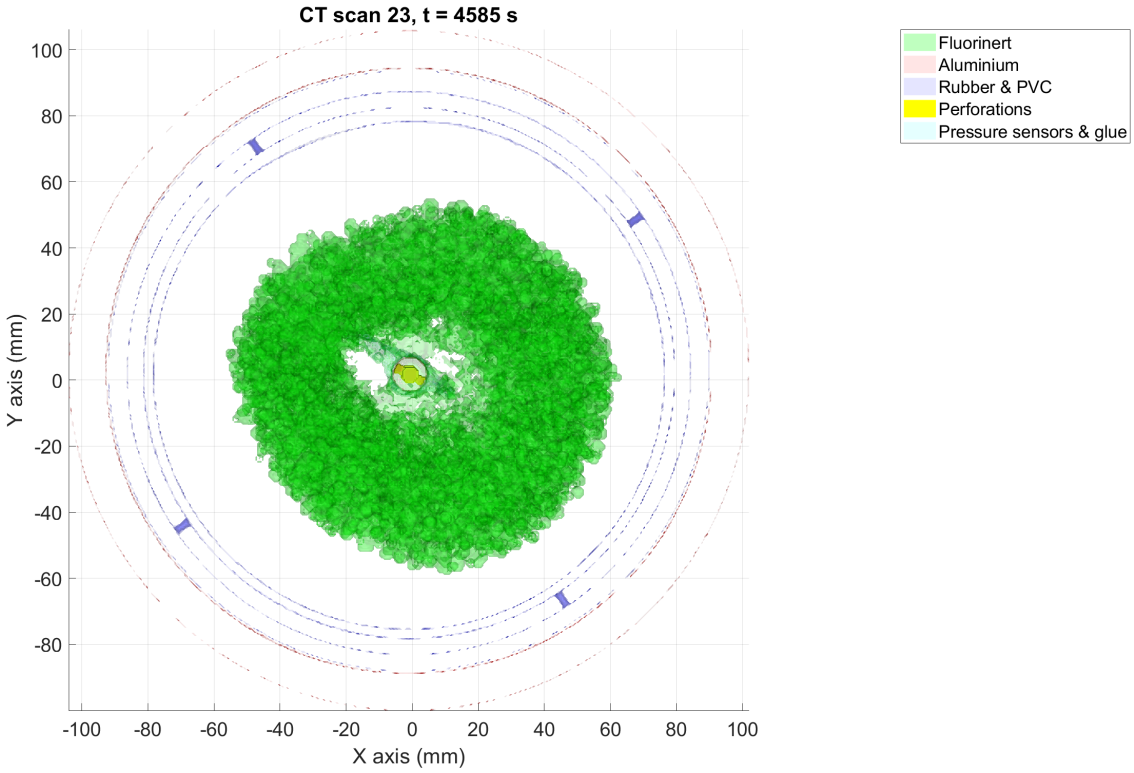

Figure 4.39: Experiment 6 - Fluorinert scan 23 - Top view

5

Conclusions

The main goal of this research was to explore the capabilities of the equipment to create and detect fractures under waterflooding conditions in unconsolidated sands. By doing so, we hope to better understand the fracture mechanisms that are involved when fracturing unconsolidated materials. The answers to these questions will help develop a better qualitative and quantitative description of the fracturing process. Most importantly, they will help to explain the injectivity decline that is observed in the field after fracturing processes take place.

Testing of equipment Experiment 1 has shown that the equipment works as intended and fractures can be created within the CT cell using a high viscosity fluid. Similar fractures have been observed as the ones seen in the work of De Pater and Dong, which used the same equipment. Fractures in several directions along the length of the open borehole were observed when the sample was excavated and placed in the micro CT scanner. The fractures were formed at higher pressures during our experiment than during the experiments of De Pater. An injection pressure of 38 MPa was required to fracture the sample with a radial pressure of 2 MPa. This is a ratio of 19, much larger than the observed injection pressure to radial pressure ratios of De Pater, which were in the range of 3.2 to 3.6 using Viscasil. Reason for this could be the higher permeability of the sample of De Pater, which was in the range of 20 Darcy, 4 times higher than the permeability of our sample. Next to that, the length and inner diameter of the injection system plays a large role when using high viscosity fluids like Viscasil. Estimations with the Hagen-Poiseuille equation [4.2], predict a large pressure drop in the injection tube. Different injection systems can lead to significantly different injection pressures.

Fracture mechanisms After the switch to low viscosity fluids for experiments 2 to 6, no more fractures were observed in the data acquisition system or in the CT scans. Shear bands as described in section 1.2 could not be seen in the CT scans. With the help of the internal pressure sensors during experiment 6, measurements of the fluid pressure at different locations in the sample could be performed. These measurements can help test the fluidization hypothesis as a fracture mechanism. This mechanism describes that when fluid pressure exceeds the confining stresses, sand rearrangements take place, resulting in fluid localizations. The internal pressure sensor that was located 5 mm in front of the perforations recorded a maximum fluid pressure of 0.73 MPa, which is lower than the confining pressures of 1 MPa during that experiment. However, the formation of a low-density region surrounding the injection tube can be observed twice throughout the experiment. The first low-density region was created during the first high flowrate injection cycle. The second low-density region was created during the high flowrate Fluorinert injection cycle, which was the injection cycle where 0.73 MPa was recorded by the internal pressure sensor. See image 4.34 for the visualization of the low-density regions. The creation of the first low-density region resulted in a clear increase in injectivity for the injection cycles that followed, indicating a higher local permeability. The migration of the clays in the sample is the current explanation for the creation of the low-density regions, but future experiments with similar samples need to confirm this.

Impairment mechanisms Even though fractures have not been created, several impairment mechanisms that were identified in the field have been observed. Plugging, wellbore fill and the resorting of grains and

finer particles are suspected to be the main reasons behind the injectivity decline in unconsolidated sand reservoirs. Experiments 4 and 5 were designed to investigate the effect of plugging which involves the creation of an external and/or internal filter cake to locally reduce the permeability. The effect of adding the quartz and bone fines to the injection fluid was noticeable within seconds. The injection pressure rose gradually over time. The injection of the fines did not lead to an increase in density that was visible on the CT scans. This observation makes it likely that the solid particles did not infiltrate the sample but instead clogged the injection system. Due to this, no conclusions regarding this impairment mechanism can be made other than the injectivity decrease due to a clogged injection tube.

The second identified impairment mechanism in the field is wellbore fill resulting from backflow during injection well shut-ins. The shut-ins create a well pressure that is lower than the reservoir pressure, allowing the inflow of reservoir fluids and solid particles into the well. This mechanism is observed in both experiment 4 and 5. The sample is pressurized to 0.2 MPa with the use of the pore fluid system. To prevent inflow from sand into the injection tube before injection takes place, a rubber pin is placed in front of the perforations on the inside of the injection tube. When injection starts, the rubber pin is pushed upwards, opening the perforations and allowing pressure communication between the injection tube and the sample. The pressure in the injection tube was lower than the sample fluid pressure when the rubber pin was pushed upwards. When the perforations opened up, backflow occurred and migrated sample grains from the region in front of the perforations, inward towards the injection tube. This left behind a lower density region in front of the perforations, visible in CT scans and images 4.20 and 4.25. We can conclude that backflow has a noticeable effect on the near wellbore region in unconsolidated sands.

The resorting of grains and finer particles within the reservoir is the last main impairment mechanism identified in the field. Since experiments 1 to 5 used a very well sorted sand and no movement of grains were observed except for the backflow, these experiments do not provide information regarding this mechanism. Experiment 6 used a sample with a bad sorting and contained Kaolinite clays. As previously described in this chapter, the migration of these clays were observed during two injection cycles. They resulted in an increase of injectivity however. The clays flushed through the sample and did not result in a denser packing in the near wellbore region. Perhaps when fluidization takes place and the smaller sand particles also migrate, this mechanism will result in a denser packing. However, this is not observed in the experiments of this thesis.

Capabilities of the equipment The focus of this thesis was to explore the capabilities of the equipment to create and detect fractures and impairment mechanisms. Creating fractures with low viscosity fluids in unconsolidated sand samples in a laboratory environment is breaking new ground. A qualitative and/or quantitative description of the conditions required to fracture with water in unconsolidated sand is not available. This thesis has shown that a large of variety of parameters can be investigated, including high pressures, high flowrates, different injection systems, fines added to the injection fluid and samples with a variety of grain sizes. Problems encountered such as the clogging of the injection tube have largely been resolved. The addition of the internal pressure sensors allows us to get multiple pressure measurement points in the sample that will greatly help with investigating under what conditions possible fractures are formed and grains mobilize. The use of a sample with fines helps mimic field conditions more closely and will lead to more interesting results regarding the rearrangement of grains.

The high density Fluorinert has proven to be clearly visible on the CT scans and help visualize flow paths. It can be hard to distinguish noise in the CT scans from density changes in the sample, especially on small scale. The tubular nature of the Poisson noise, described in chapter 3, will give difficulties detecting localized flow paths. Sand and/or clay particles that mobilized in front of the perforations during experiment 6 have been detected on the CT scans. Future experiments will have to show if flow channels can also be distinguished from the CT scanner noise.

We can conclude that phase 1 of this research was successful in investigating the equipment capabilities and the experiments in combination with this thesis will form a solid basis for future experiments. Fractures and/or crack-like displacement discontinuities have yet to be created using low viscosity fluids. However, the equipment has shown to be capable in investigating several impairment mechanisms. In chapter **??** we will discuss the recommendations for the continuation of this project.

6

Discussion & Recommendations

Impairment mechanisms Phase 2 of this research will focus on the impairment mechanisms that lead to an injectivity decline. The most difficult mechanism to investigate at this moment is plugging. Attempts were made during experiment 4 and 5, but resulted in a clogged injection tube. The use of internal pressure sensors during these plugging experiments will greatly help identifying what causes the increase in injection pressure. If the injection tube is clogged, no changes should be detected at the internal pressure sensors. If the formation is plugged, the pressure difference between the sensors will change over time. With the use of a wider injection tube and larger perforations, a clogged injection tube could be prevented. Next to that, the rubber pin mechanism as a sand screen has proven to not work as desired, leading to pressure surges and perhaps even assist the plugging of the injection tube when fines are injected. Depending on the sample sand, an external sand filter could be used with a mesh large enough to pass the injection fines and small enough to prevent sand particles from infiltrating. Quartz injection is preferable since this would be detectable on the CT scans, while bone meal with a similar density as water is not.

The equipment is very suited to investigate wellbore fill caused by backflow. Several pressure surges could be created by creating a vacuum in the injection system and then opening the main injection valve. To mimic field conditions more closely, multiple perforations along the injection tube could be made. These perforations can clog one at the time, decreasing the injectivity over time. Discussions concerning cross flow have also started. With the use of an impermeable layer in the middle of the sample, two reservoir sections can be made in the CT cell. These sections can be pressurized at different pressures, with the use of the pore fluid system on both sides. A mechanism will have to be designed that allows us to control the cross flow process along the injection tube.

Experiment 6 has shown that samples with multiple sands and clays can be used. The results show that the clays migrate through the sample at certain injection cycles. This forms a solid basis for additional research on the rearrangement of grains and fines as an impairment mechanism. With the use of the internal pressure sensors, we can also investigate the permeability changes within the sample.

Fracturing As expected beforehand, fracturing with low viscosity fluids has proven to be very difficult. However, the use of low confining stresses will lead to lower required injection pressures to migrate sands and fines. Higher injection rates can be attempted with the air stroke pump and intensifier to a point where fluidization possibly takes place. Lower permeability samples can also be created with the use of additional sands, silts and clays. This process of lowering confining stresses, increasing flow rates and decreasing the sample permeability should be continued and hopefully will eventually lead to fracture formation.

Other Several other things can be improved on the equipment. The LVDT measuring the sample deformation has shown to contain a large amount of noise. This is caused by both the magnetic field of the air stroke pump and the movement of the CT cell when CT scans are made. The movement noise could be reduced by creating an improved mount mechanism for the LVDT. The current mechanism that holds the LVDT in place is not rigid enough to steady the sensor. In addition, the current LVDT can measure much more displacement than necessary, ranging several centimeters rather than the required millimeters. A more compact sensor has less momentum to move during CT scans.

The algorithm used in this thesis is initially designed to visualize the infiltration zone of the Fluorinert. It will do less good of a job identifying fractures or flow channels. As previously mentioned, the Poisson noise takes tubular shapes, which will give difficulties distinguishing subtle flow channels from noise in future experiments. A good amount of calibration scans before fracturing is attempted will help in this process. These scans could be made before injection, or during the first slow injection cycles. High-density materials such as steel should be prevented around the scan interval at all times. It is also recommended to keep the axial pressure slightly higher than the radial pressure, for example at a ratio of 1.2 or 1.5. This leads to fractures and channels having a preferential direction in the X, Y plane. Searching in a 2D plane for fractures and channels is easier than searching in all directions.

Lastly, I recommend a more extensive parameter study in the upcoming research phase. The focus of this phase was on exploring the equipment capabilities. New methods and adjustments to the equipment were made every experiment, proving it difficult to compare their results. Once the same fluids, injection system and samples are used, the results can be compared and outliers can be detected. Modeling and simulations can help with this process and with the use of the internal pressure sensors, more data points are available to check the viability of the simulation results.

Bibliography

[1] J.P. Van Baaren. Quick-look permeability estimates using sidewall samples and porosity logs. In *paper presented at 6th Annual European Logging symposium*. Society of Professional Well Log Analysts, 1979.

[2] D.C. Beard and P.K.Weyl. Influence of texture on porosity and permeability of unconsolidated sand. *AAPG Bulletin*, 57(2):349 – 369, February 1973.

[3] R.R. Berg. Method for determining permeability from reservoir rock properties. *Gulf Coast Association of Geological Societies*, 20:303 – 317, 1970.

[4] F.E. Boas and D. Fleischmann. Ct artifacts: Causes and reduction techniques. *Stanford University School of Medicine*, 2012.

[5] B. Bohloli and C.J de Pater. Experimental study on hydraulic fracturing of soft rocks: Influence of fluid rheology and confining stress. *Journal of Petroleum Science and Engineering*, 53:1–12, 2006.

[6] H. Chang. *Hydraulic Fracturing in Particulate Materials*. PhD thesis, Georgia Institute of Technology, November 2004.

[7] A. Chudnovsky, Y. Shulkin, E. Golovin, H. Zhang, J.W. Dudley, and G.K. Wong. Observation and modeling of fluid flow under matrix and fracturing injections in unconsolidated sand. In *paper presented at 49th US Rock Mechanics / Geomechanics Symposium*. ARMA, June 2015.

[8] Y. Dong. *Hydraulic Fracture Containment in Sand*. PhD thesis, Delft University of Technology, May 2010.

[9] L.N. Germanovich, R.S. Hurt, J.A. Ayoub, E. Siebrits, W.D. Norman, I. Ispas, and C. Montgomery. Experimental study of hydraulic fracturing in unconsolidated materials. In *paper presented at SPE International Symposium and Exhibition on Formation Damage Control*. SPE, February 2012.

[10] M. Khodaverdian and P. McElfresh. Hydraulic fracturing stimulation in poorly consolidated sand: Mechanisms and consequences. In *paper presented at SPE Annual Technical Conference and Exhibition*. SPE, October 2000.

A

Experiment procedure flowcharts

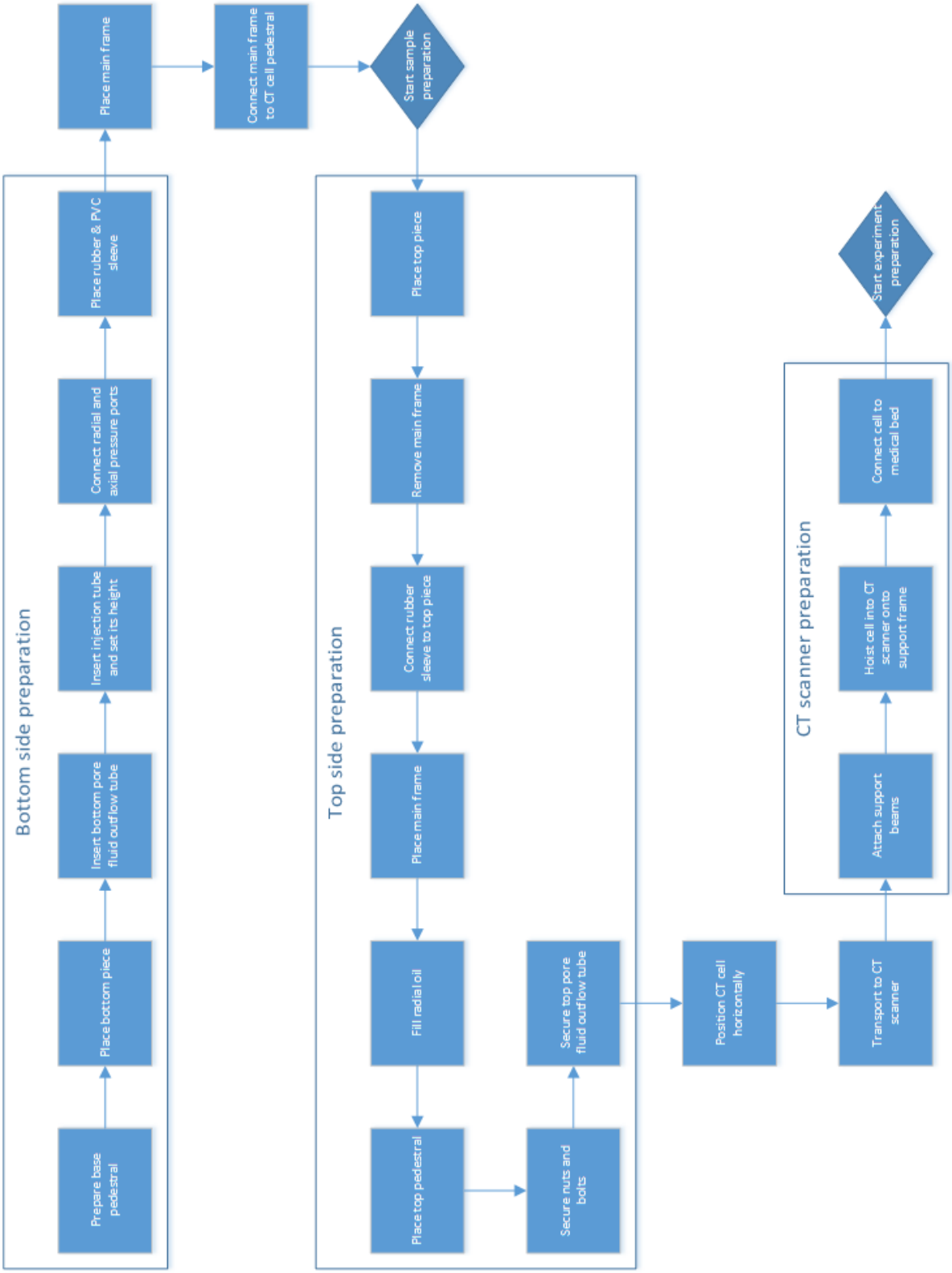

Figure A.1: Flowchart - CT cell preparation

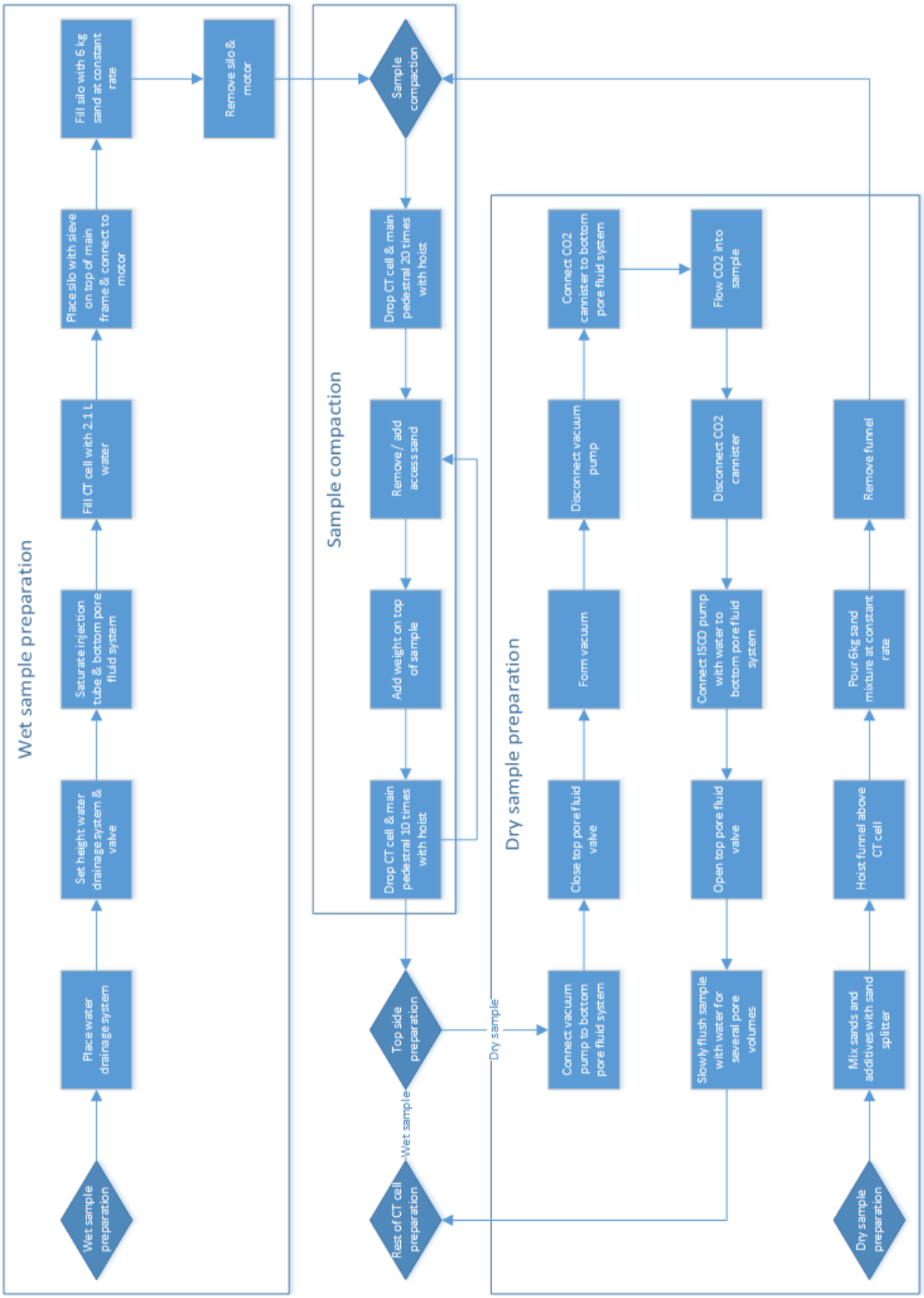

Figure A.2: Flowchart - Sample preparation

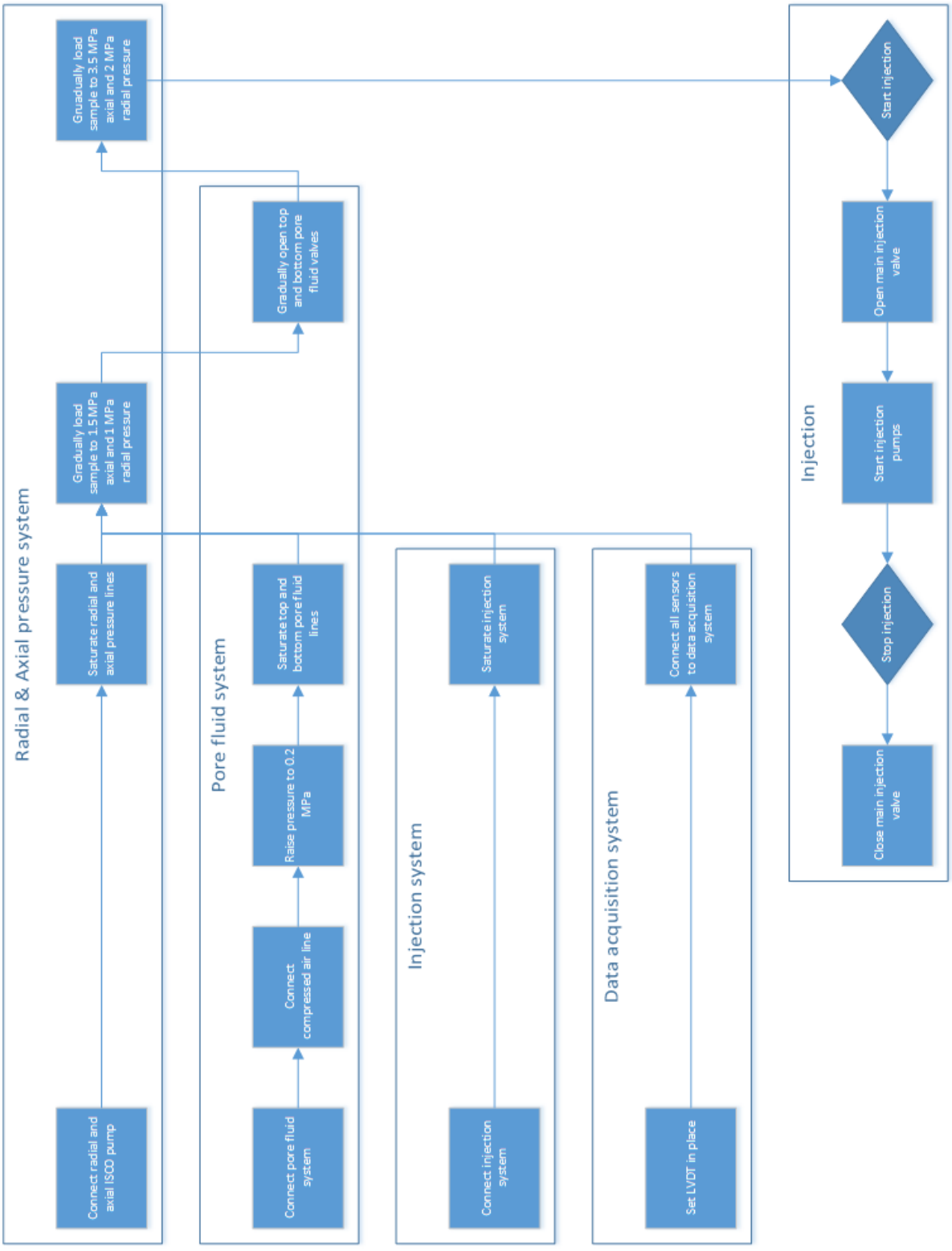

Figure A.3: Flowchart - Experiment procedure

B

Technical drawings CT cell

Note that the figures in this appendix are of the original pressure CT vessel which was designed for mud studies, such as infiltration studies. TU Delft made a series of adjustments to the vessel to allow an injection tube to be placed inside the sample. Next to that, the pore fluid outflow system was created, using the sinter filters and outflow mechanisms in the brass plugs that are described in chapter 2. However, except for the injection pipe entry, volumetrics and measurements of the equipment have not been changed.

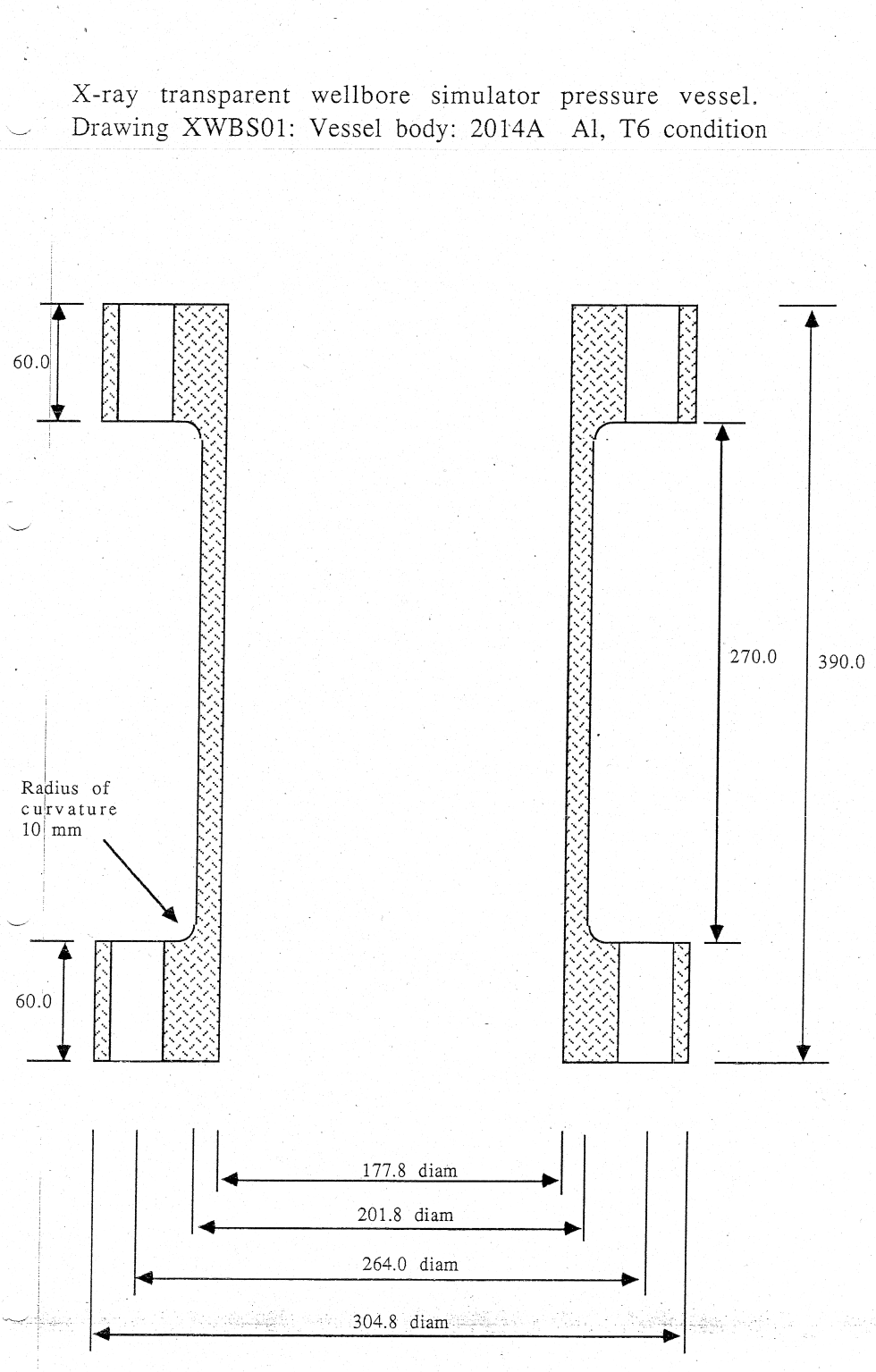

Figure B.1: Technical drawing CT cell - Main aluminium frame

X-ray transparent wellbore simulator pressure vessel.
Drawing XWBS02: Vessel body

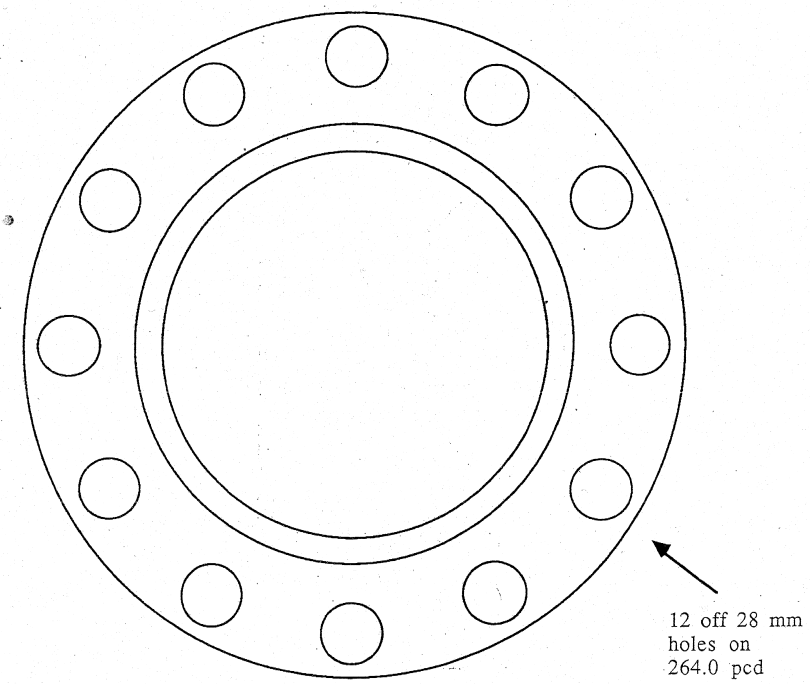

Figure B.2: Technical drawing CT cell - Main aluminium frame (cross section)

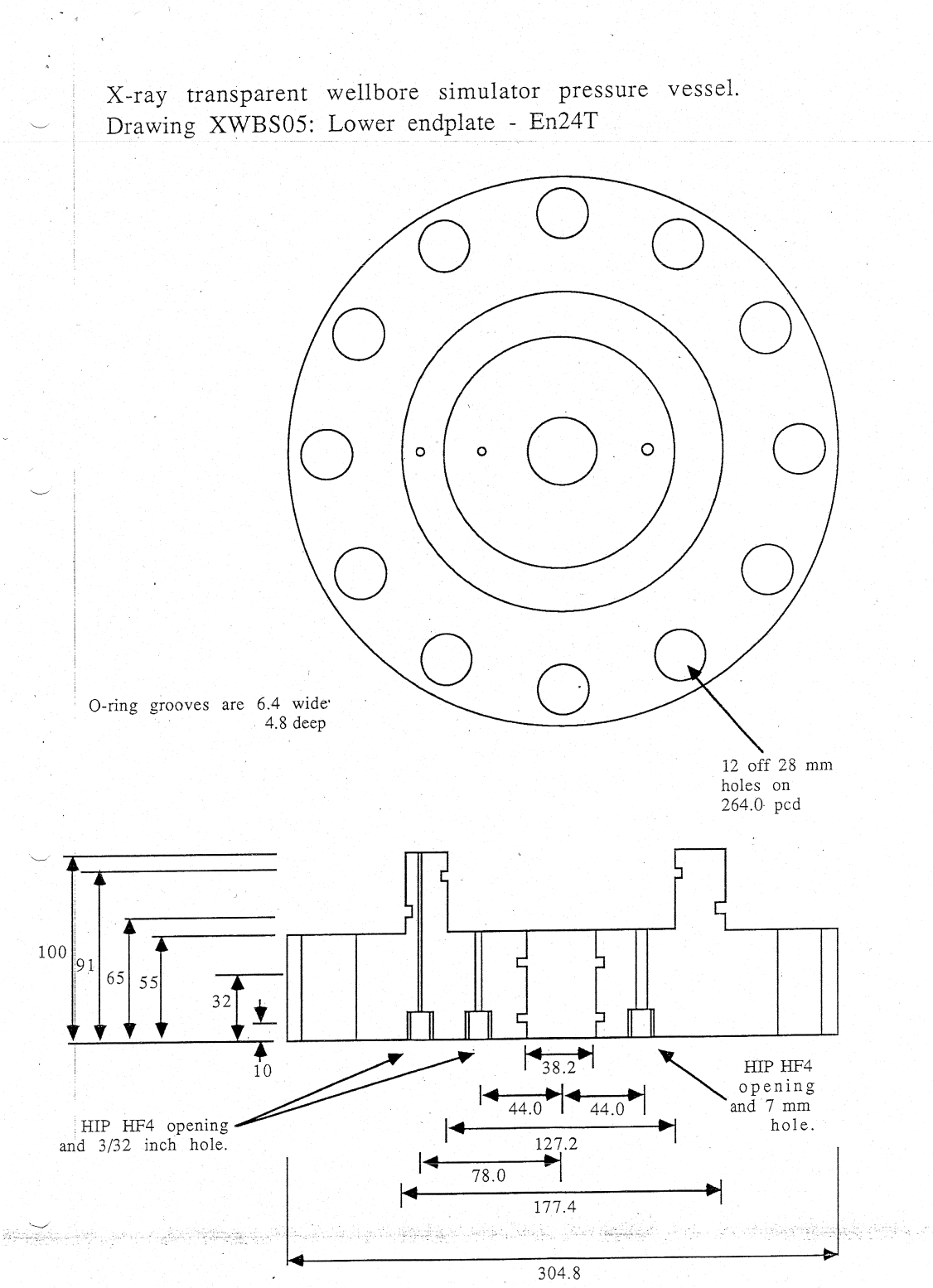

Figure B.3: Technical drawing CT cell - Base aluminium lid

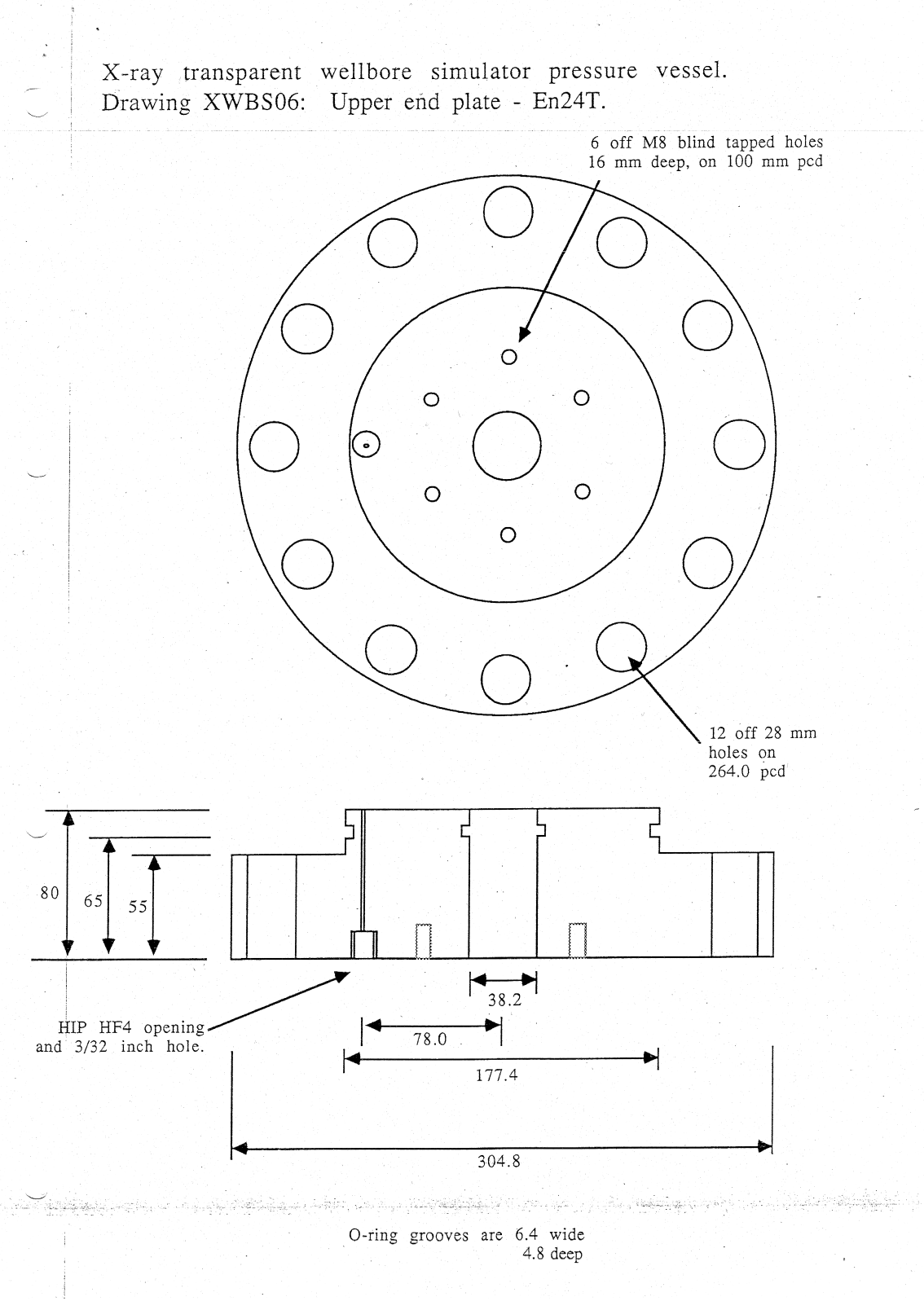

Figure B.4: Technical drawing CT cell - Top aluminium lid

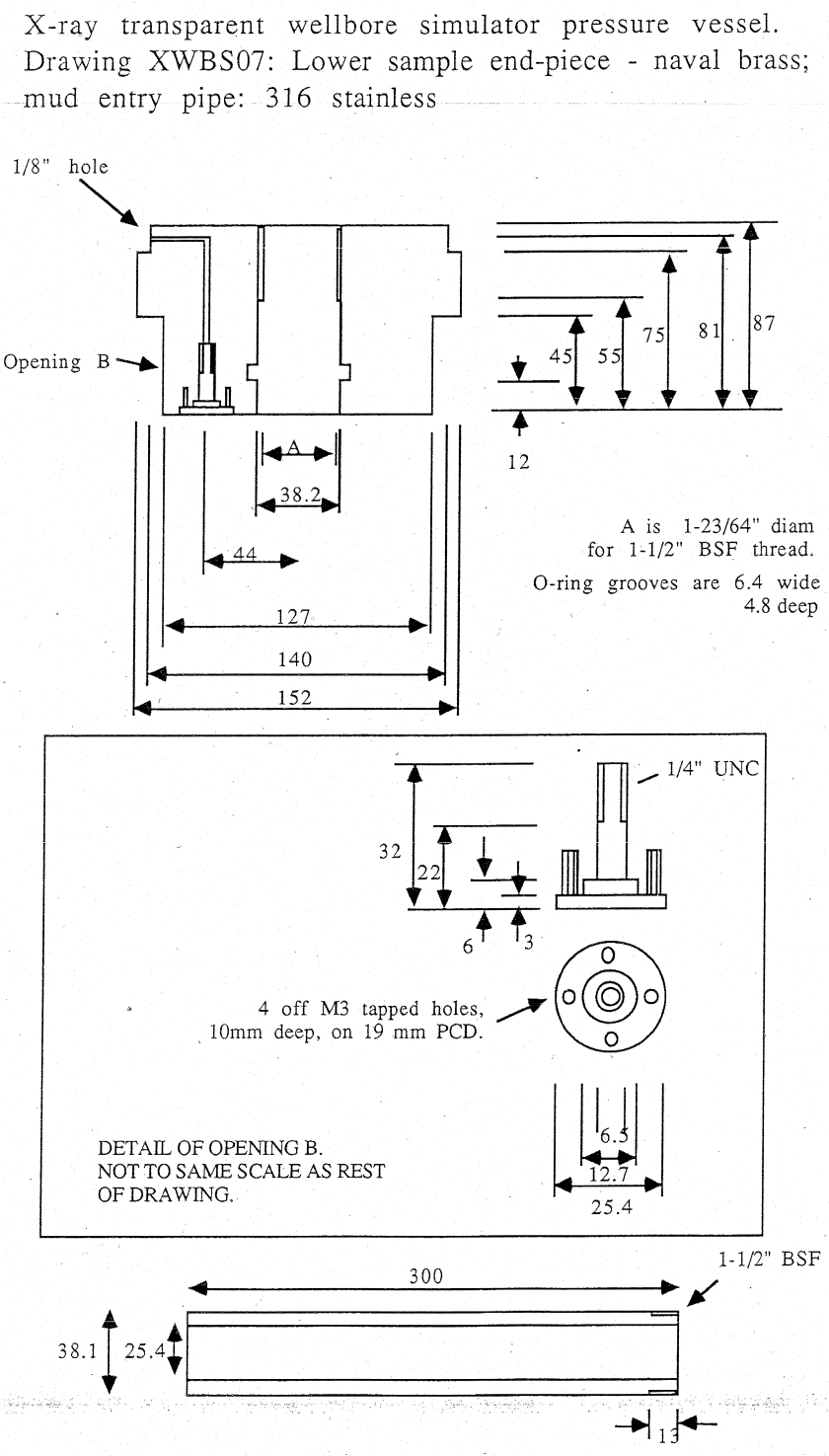

Figure B.5: Technical drawing CT cell - Base brass plug

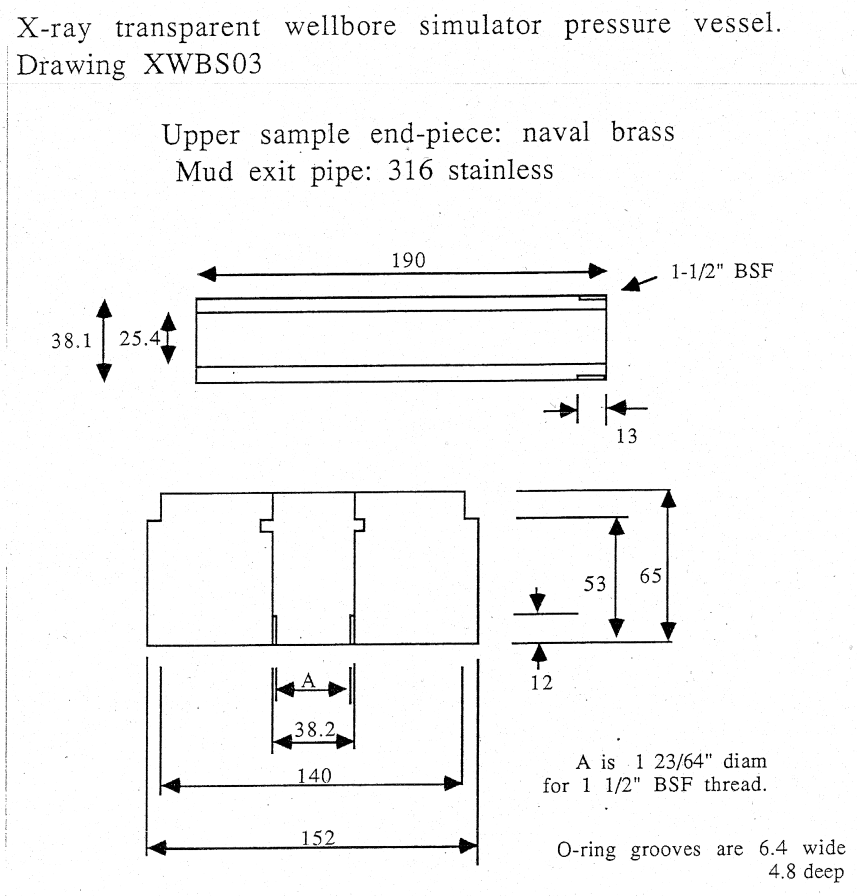

Figure B.6: Technical drawing CT cell - Top brass plug